

AD A109678

LEVEL II

(12)

DNA 5404F

THREE-DIMENSIONAL NUMERICAL ANALYSES OF EARTH PENETRATION DYNAMICS

Y. M. Ito

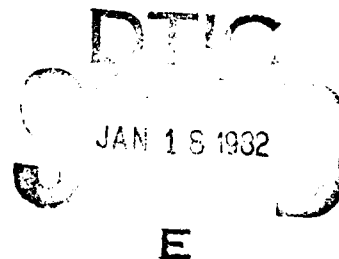
R. B. Nelson

F. W. Ross-Perry

California Research & Technology, Inc.

6269 Variel Avenue

Woodland Hills, California 91367



31 January 1979

Final Report for Period 1 September 1976—11 January 1979

CONTRACT No. DNA 001-76-C-0383

APPROVED FOR PUBLIC RELEASE;
DISTRIBUTION UNLIMITED.

THIS WORK SPONSORED BY THE DEFENSE NUCLEAR AGENCY
UNDER RDT&E RMSS CODE B344078464 Y99QAXSB04839 H2590D.

DTIC FILE COPY

Prepared for

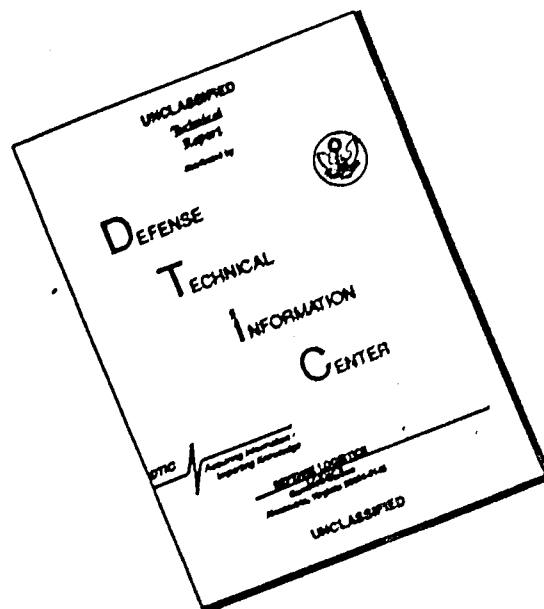
Director

DEFENSE NUCLEAR AGENCY

Washington, D. C. 20305

01 15 82 035

DISCLAIMER NOTICE



THIS DOCUMENT IS BEST QUALITY AVAILABLE. THE COPY FURNISHED TO DTIC CONTAINED A SIGNIFICANT NUMBER OF PAGES WHICH DO NOT REPRODUCE LEGIBLY.

Destroy this report when it is no longer
needed. Do not return to sender.

PLEASE NOTIFY THE DEFENSE NUCLEAR AGENCY,
ATTN: STTI, WASHINGTON, D.C. 20305, IF
YOUR ADDRESS IS INCORRECT, IF YOU WISH TO
BE DELETED FROM THE DISTRIBUTION LIST, OR
IF THE ADDRESSEE IS NO LONGER EMPLOYED BY
YOUR ORGANIZATION.



UNCLASSIFIED

SECURITY CLASSIFICATION OF THIS PAGE (When Data Entered)

REPORT DOCUMENTATION PAGE		READ INSTRUCTIONS BEFORE COMPLETING FORM
1. REPORT NUMBER DNA 5404F	2. GOVT ACCESSION NO. AD-A109	3. RECIPIENT'S CATALOG NUMBER 678
4. TITLE (and Subtitle) THREE-DIMENSIONAL NUMERICAL ANALYSES OF EARTH PENETRATION DYNAMICS		5. TYPE OF REPORT & PERIOD COVERED Final Report for Period 1 Sep 76-11 Jan 79
7. AUTHOR(s) Y. M. Ito R. B. Nelson F. W. Ross-Perry		8. CONTRACT OR GRANT NUMBER(s) DNA 001-76-C-0383
9. PERFORMING ORGANIZATION NAME AND ADDRESS California Research & Technology, Inc. 6269 Variel Avenue Woodland Hills, California 91367		10. PROGRAM ELEMENT PROJECT, TASK AREA & WORK UNIT NUMBERS Subtask Y99QAXSB048-39
11. CONTROLLING OFFICE NAME AND ADDRESS Director Defense Nuclear Agency Washington, D.C. 20305		12. REPORT DATE 31 January 1979
14. MONITORING AGENCY NAME & ADDRESS (if different from Controlling Office)		13. NUMBER OF PAGES 92
		15. SECURITY CLASS. (of this report) UNCLASSIFIED
		15a. DECLASSIFICATION/DOWNGRADING SCHEDULE
16. DISTRIBUTION STATEMENT (of this Report) Approved for public release; distribution unlimited.		
17. DISTRIBUTION STATEMENT (of the abstract entered in Block 20, if different from report)		
18. SUPPLEMENTARY NOTES This work sponsored by the Defense Nuclear Agency under RDT&E RMSS Code B344078464 Y99QAXSB04839 H2590D.		
19. KEY WORDS (Continue on reverse side if necessary and identify by block number) Non-Normal Impact Lagrangian/Eulerian Earth Penetrator Penetration Fourier Expansion Sandstone Target Terradynamics Finite-Element Structural Response Reverse Ballistic Test Finite-Difference Scale Model		
20. ABSTRACT (Continue on reverse side if necessary and identify by block number) A new three-dimensional numerical code, TRIFLE, is described which provides, for the first time, a rigorous yet efficient analytical tool to investigate the penetration dynamics of semi-rigid projectiles under asymmetric (non-normal) impact conditions. This is a key development since most real impacts and penetrations involve at least some degree of both yaw and obliquity, and since small degrees of asymmetry can have significant effects on the design environment of earth penetrating systems.		

DD FORM 1473

EDITION OF 1 NOV 65 IS OBSOLETE

UNCLASSIFIED

SECURITY CLASSIFICATION OF THIS PAGE (When Data Entered)

371 100

UNCLASSIFIED

SECURITY CLASSIFICATION OF THIS PAGE (When Data Entered)

20. ✓ Abstract (continued)

In the TRIFLE code formulation, the full three-dimensional equations of motion are solved using (1) a moving polar cylindrical coordinate reference frame aligned with the projectile, (2) a Fourier representation of circumferential variation to couple together several r-z finite-difference planes in the target media, (3) an arbitrary Lagrangian/Eulerian transformation to allow these planes to remain planes, and (4) a momentum exchange procedure to determine forces on the penetrator. The circumferential Fourier representation in TRIFLE provides highest resolution near the penetrator, and hence, TRIFLE is more efficient and practical than a three-dimensional cartesian finite-difference formulation.

As the first major demonstration of this new numerical technique, the TRIFLE code has been used to successfully determine the time-resolved force distribution on the DNA 0.284-scale earth (sandstone) penetrator in the 3° yawed-impact reverse ballistic sled test conducted at Sandia Laboratories. The corresponding structural response results from a finite-element analysis, driven by the applied projectile forces prescribed from the TRIFLE penetration dynamics solution, compare well with the experimental observations.

A series of parametric calculations of penetration dynamics under various impact conditions was also performed using the TRIFLE code. The effects of nose shape, body length, impact velocity, obliquity and yaw on penetrator loading is examined.

Accession For	
NTIS GRA&I	<input checked="" type="checkbox"/>
DTIC TAB	<input type="checkbox"/>
Unannounced	<input type="checkbox"/>
Justification	
By	
Distribution/	
Availability Codes	
Dist	Avail and/or Special
A	

UNCLASSIFIED

SECURITY CLASSIFICATION OF THIS PAGE (When Data Entered)

SUMMARY

A practical three-dimensional numerical code has been developed which provides, for the first time, a rigorous analytical tool to investigate the penetration dynamics of projectiles under asymmetric (non-normal) impact conditions. This is a key development, since most real impacts and penetrations involve at least some degree of both yaw and obliquity, and since small degrees of asymmetry can have significant effects on the design environment of penetrating systems.

The 3-D numerical technique, TRIFLE, was achieved through major modifications of an existing 2-D finite-difference code. The 2-D code, WAVE-L, uses an explicit, Lagrangian formulation based on the HEMP method and has been adapted and validated for treatment of normal-incidence (axisymmetric) impact and penetration problems.

In the TRIFLE code formulation (see Figure S-1), the *full* three-dimensional equations of motion are solved using a) *moving* cylindrical coordinate reference frame aligned with the penetrator, b) Fourier representation of circumferential variation to *couple* several r-z finite-difference planes in the target medium together, c) arbitrary Lagrangian-Eulerian (ALE) transformations to allow these planes to remain planes, and d) momentum exchange to determine forces on the penetrator. The ALE transformations are also used to provide *in-plane* automatic rezoning and the momentum exchange eliminates the need for "slide-line" logic between the penetrator and the target. The circumferential Fourier representation in the TRIFLE provides highest resolution near the penetrator, and hence TRIFLE is more efficient and practical than a *full* 3-D (cartesian) finite-difference code.

- Define moving cylindrical coordinate (r, θ, z) reference frame aligned with rigid-body penetrator.
- Divide 3-D space of target medium into N circumferentially spaced ($\theta = \text{const.}$) "Fourier" $(r-z)$ planes.
- Define 2-D $(r-z)$ finite difference grid with 3-D particle velocity (v_r, v_θ, v_z) in each "Fourier" plane.
- Couple planes together with N -term Fourier series which define circumferential variation of parameters.
- Introduce arbitrary Lagrangian-Eulerian (ALE) transformations so that the planes remain planes.
- Satisfy full 3-D equations of motion in each "Fourier" plane.
- Determine forces on penetrator using momentum exchange with target medium.

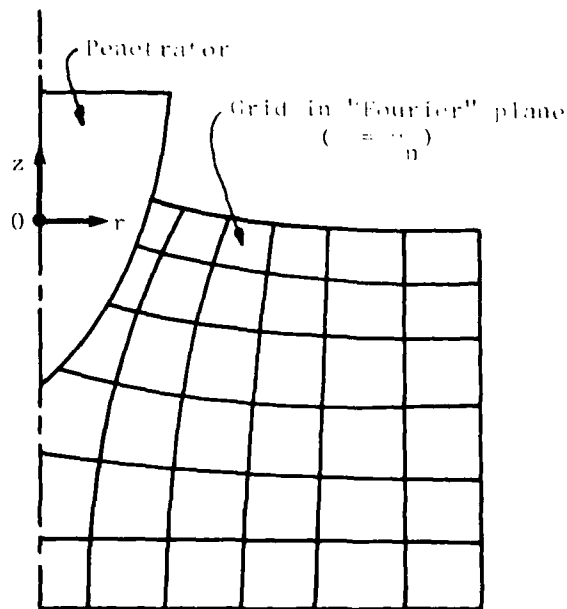
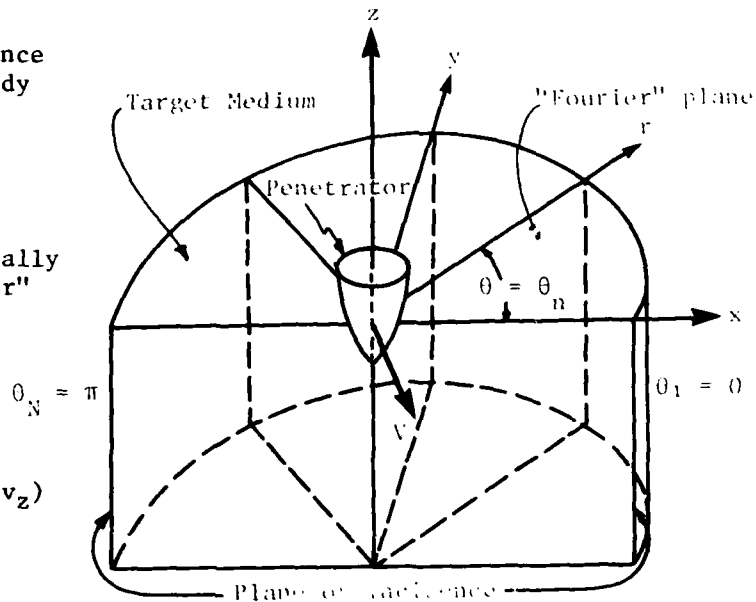


Figure S-1. Basic Concepts of TRIFLE Code.

The formulation, coding and check-out of the 3-D TRIFLE code was performed in a step-by-step manner through a series of 3-D/2-D comparison test cases with the 2-D WAVE-L code. These test cases involved dynamic loadings on plane strain solid-cylinders and pipes, as well as axisymmetric rigid-body normal penetrations. The comparisons of 3-D/2-D code results showed very good agreement. Also, it was noted that a five-plane Fourier representation provides good resolution for problems with circumferential variations greater than expected in asymmetric penetration cases.

As the first major demonstration of this new 3-D numerical technique, the TRIFLE code has been used to successfully determine the time-resolved force distribution on the DNA 0.284-scale earth (sandstone) penetrator in the 3° yawed-impact reverse ballistic sled test conducted at Sandia Laboratories. The corresponding structural response results from a 2½-D *plane stress* NONSAP code analysis (driven by the applied projectile forces prescribed from the TRIFLE penetration dynamics solution) compare well with the experimental observations.

This successful comparison of experimental results and numerical predictions verifies that a practical 3-D technique is now available for determination of the spatially and temporally resolved design loads on semi-rigid earth penetrators in non-normal impact and penetration. (It is also expected that the TRIFLE technique can be adapted to solve other 3-D dynamic problems, including certain types of buried structural response and tunnel collapse problems.)

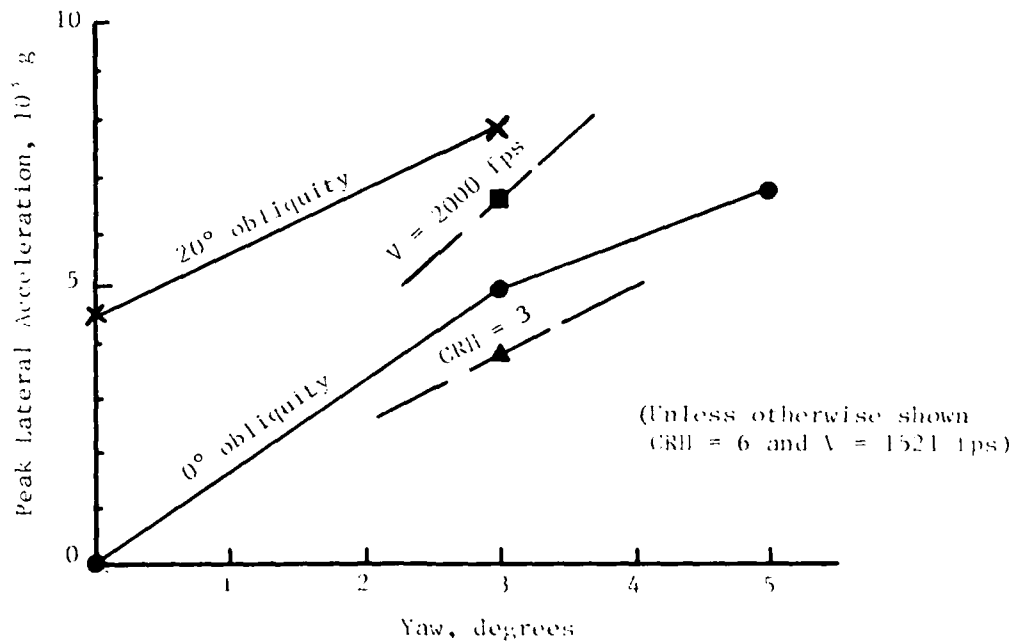
A series of 3-D parametric calculations of the penetration dynamics occurring under various impact conditions was also completed using the TRIFLE code. The effects of nose shape, body length-to-diameter ratio, impact velocity, obliquity and yaw on

penetrator loading were examined for impact and nose embedment into sandstone. The results of this analysis are summarized in Table S-1.

Numerical first-principle code solutions can provide information which is not readily or efficiently accessible by other techniques (analytical *or* experimental). In this respect, these code solutions have been, and will continue to be, particularly valuable in the penetration dynamics field. The TRIFLE code can now be used to quantify the effects on the design environment so that trajectory stabilization requirements, strengthened penetrator design requirements, and/or increased penetrator cargo hardness tolerances can be established.

Table S-1. Parametric Analyses of Asymmetric Penetration

1. For nose shapes considered, obliquities to 20° and yaw angles to 5° do not significantly affect *axial* acceleration as compared to normal impact.
2. Lateral (and angular) accelerations are very sensitive to yaw and/or obliquity:



3. CRH = 3 nose shape gives ~5% *greater* axial acceleration than CRH = 6 nose shape, but ~25% *smaller* lateral acceleration.
4. For CRH = 6 nose shape, 2000 fps impact velocity gives ~30% *greater* lateral and axial accelerations than 1521 fps.
5. L/D = 5.3 penetrator has about the *same* lateral acceleration, but ~50% *greater* angular acceleration than L/D = 10.6 penetrator with same W/A.

PREFACE

This report describes a numerical code investigation of penetration dynamics performed for the Defense Nuclear Agency (DNA) during the period from September 1976 to January 1979 under Contract DNA 001-76-C-0383. The DNA technical monitor was Lt. Col. D. R. Spangler. Technical coordination was provided by P. F. Hadala and B. Rohani of the U. S. Army Engineer Waterways Experiment Station.

The project was under the general supervision of M. H. Wagner. The authors gratefully acknowledge the contributions of M. Rosenblatt who provided the initial formulation for the numerical technique and of D. T. Liu who performed the initial code development. Thanks are also due to T. E. Wolverton who provided technical assistance in the final numerical formulation and to H. D. Zimmerman who performed some of the parametric calculations.

PRECEDING PAGE BLANK-NOT FILMED

Table 1. Conversion factors for U.S. customary to metric (SI) units of measurement.

To Convert From	To	Multiply By
angstrom	meters (m)	1.000 000 X E -10
atmosphere (normal)	kilo pascal (kPa)	1 013 25 X E +2
bar	kilo pascal (kPa)	1 000 000 X E +2
barn	meter ² (m ²)	1.000 000 X E -28
British thermal unit (thermochemical)	joule (J)	1.054 350 X E +3
calorie (thermochemical)	joule (J)	4 184 000
cal (thermochemical) /cm ²	mega joule/m ² (MJ/m ²)	4.184 000 X E -2
curie	*giga becquerel (GBq)	3 700 000 X E +1
degree (angle)	radian (rad)	1.745 329 X E -2
degree Fahrenheit	degree kelvin (K)	$(^{\circ}\text{F} - 32) \times 5/9$
electron volt	joule (J)	1.602 19 X E -19
erg	joule (J)	1.000 000 X E -7
erg/second	watt (W)	1.000 000 X E -7
foot	meter (m)	3 048 000 X E -1
foot-pound-force	joule (J)	1.355 818
gallon (U. S. liquid)	meter ³ (m ³)	3 785 412 X E -3
inch	meter (m)	2 540 000 X E -2
jerk	joule (J)	1 000 000 X E +9
joule/kilogram (J/kg) (radiation dose absorbed)	Gray (Gy)	1.000 000
kilotons	terajoules	4 183
kip (1000 lbf)	newton (N)	4 448 222 X E +3
kip/inch ² (ksi)	kilo pascal (kPa)	6 894 757 X E +3
ktap	newton-second/m ² (N-s/m ²)	1 000 000 X E +2
micron	meter (m)	1 000 000 X E -6
mil	meter (m)	2 540 000 X E -5
mile (international)	meter (m)	1 609 344 X E +3
ounce	kilogram (kg)	2 834 952 X E -2
pound-force (lbf avoirdupois)	newton (N)	4 448 222
pound-force/inch	newton-meter (N-m)	1 129 848 X E -1
pound-force/inch	newton/meter (N/m)	1 751 268 X E +2
pound-force/foot ²	kilo pascal (kPa)	4 788 026 X E -2
pound-force/inch ² (psi)	kilo pascal (kPa)	6 894 757
pound-mass (lbm avoirdupois)	kilogram (kg)	4 535 924 X E -1
pound-mass-foot ² (moment of inertia)	kilogram-meter ² (kg-m ²)	4 214 011 X E -2
pound-mass/foot ³	kilogram/meter ³ (kg/m ³)	1 601 846 X E +1
rad (radiation dose absorbed)	*Gray (Gy)	1 000 000 X E -2
roentgen	coulomb/kilogram (C/kg)	2 579 760 X E -4
shake	second (s)	1 000 000 X E -8
slug	kilogram (kg)	1 459 390 X E +1
torr (mm Hg, 0° C)	kilo pascal (kPa)	1 333 22 X E -1

*The becquerel (Bq) is the SI unit of radioactivity; 1 Bq = 1 event/s.

**The Gray (Gy) is the SI unit of absorbed radiation.

A more complete listing of conversions may be found in "Metric Practice Guide E 380-74," American Society for Testing and Materials.

TABLE OF CONTENTS

<u>Section</u>	<u>Page</u>
SUMMARY	1
PREFACE	7
LIST OF ILLUSTRATIONS	10
LIST OF TABLES.	12
1 INTRODUCTION.	13
2 TRIFLE PENETRATION DYNAMICS CODE.	17
2.1 MATHEMATICAL DEFINITIONS	18
2.2 COMPUTATIONAL FEATURES	24
2.3 CODE VERIFICATION.	26
3 PENETRATION DYNAMICS OF YAWED IMPACT.	28
4 STRUCTURAL RESPONSE AND COMPARISON WITH DATA.	50
4.1 STRUCTURAL RESPONSE MODEL.	50
4.2 RESPONSE ANALYSIS AND COMPARISONS.	53
5 PARAMETRIC ANALYSIS OF PENETRATION DYNAMICS	73
6 CONCLUSIONS AND RECOMMENDATIONS FOR FUTURE INVESTIGATIONS.	82
REFERENCES.	85

LIST OF ILLUSTRATIONS

<u>Figure</u>		<u>Page</u>
S-1	Basic Concepts of TRIFLE Code	2
2.1	Basic Concepts of TRIFLE Code	23
2.2	3-D Code Analysis - Computation Scheme.	25
3.1	Geometry of Oblique, Yawed Impact Problem	29
3.2	Penetrator and Target Data.	31
3.3	RBT Penetrator for 3° Yawed Impact at 1521 fps into Dakota Sandstone Target (in 180° - 0° Planes).	33
3.4	Initial Computational Grid of Sandstone Target in 180° - 0° Planes	34
3.5	Principal Stress, Particle Relative Velocity and Grid Configuration in 180° - 0° Planes at 100 μsec.	36
3.6	Principal Stress, Particle Relative Velocity and Grid Configuration in 180° - 0° Planes at 180 μsec.	37
3.7	Principal Stress, Particle Relative Velocity and Grid Configuration in 180° - 0° Planes at 380 μsec.	38
3.8	Principal Stress, Particle Relative Velocity and Grid Configuration in 180° - 0° Planes at 525 μsec.	39
3.9	Principal Stress, Particle Velocity and Grid Configuration in All Planes at 800 μsec	40
3.10	TRIFLE Code Solution (Stress and Grid Configura- tion) of 3° Yawed-Impact and Body Length Penetra- tion of DNA 0.284-Scale RBT	41
3.11	Penetrator Axial Deceleration and Force Time History	42
3.12	Penetrator Lateral Deceleration and Force Time History	43
3.13	Penetrator Angular Deceleration and Torque Time History	44

LIST OF ILLUSTRATIONS (continued)

<u>Figure</u>		<u>Page</u>
3.14	Stress and Force Distributions along Penetrator Contour at 800 μ sec	46
3.15	Net Axial Force Distribution along Penetrator Contour	48
3.16	Net Lateral Force Distribution along Penetrator Contour	49
4.1	Modified Plane Stress (2½-D) Element Model of Penetrator Structure (including Applied Force Locations).	52
4.2	Net Axial Force Time Histories for Penetrator Stations Forward of Center of Mass.	54
4.3	Net Axial Force Time Histories for Penetrator Stations Aft of Center of Mass.	55
4.4	Net Lateral Force Time Histories for Penetrator Stations Forward of Center of Mass.	57
4.5	Net Lateral Force Time Histories for Penetrator Stations Aft of Center of Mass.	58
4.6	Experimental and Analytical Results for Lateral Acceleration Near the Center of Mass.	59
4.7	Experimental and Analytical Results for Axial Acceleration Near the Center of Mass.	60
4.8	Experimental and Analytical Results for Lateral Acceleration at Aft End	62
4.9	Experimental and Analytical Results for Axial Acceleration at Aft End	63
4.10	Experimental and Analytical Axial Strains on Outer Face of Top Surface of EPW Midsection	65
4.11	Experimental and Analytical Axial Strains on Inner Face of Top Surface of EPW Midsection	66

LIST OF ILLUSTRATIONS (continued)

<u>Figure</u>		<u>Page</u>
4.12	Experimental and Analytical Axial Strains on Inner Face of Bottom Surface of EPW Midsection. . .	67
4.13	Experimental and Analytical Axial Strains on Outer Face of Bottom Surface of EPW Midsection. . .	68
4.14	Experimental and Analytical Results for Axial Strain on Outer Top Surface of Aft End.	70
4.15	Experimental and Analytical Results for Axial Strain on Outer Bottom Surface of Aft End	71
5.1	Comparison of Penetrator Axial Deceleration	75
5.2	Comparison of Penetrator Lateral Deceleration . . .	76
5.3	Comparison of Penetrator Angular Acceleration . . .	77

LIST OF TABLES

<u>Table</u>		<u>Page</u>
S-1	Parametric Analyses of Asymmetric Penetration . . .	5
5.1	Parametric Study of Asymmetric Penetration.	74
5.2	Parametric Analyses of Asymmetric Penetration . . .	80

SECTION 1

INTRODUCTION

A determination of the performance capabilities of earth penetrating weapons (EPW) requires a knowledge of the influence of the critical parameters on impact survivability and post-impact performance. Overall aspect ratio (length over diameter, L/D), nose configuration (caliber radius head, CRH) and parameters defining internal structure are obvious parameters to be considered, as well as parameters which specify flight velocity, impact attitude (yaw and obliquity) and target hardness.

To quantify the allowable ranges of parameters which define penetrator design, flight envelope and target characteristics, a combined program of testing and analytical investigation is necessary. The testing program provides benchmarks for evaluating and proof testing analytical procedures and establishes an experimental data base to support EPW design evaluations. Since physical tests are very expensive, only a limited number are feasible.

Analytical investigations are relatively less expensive to perform. However, to be useful as a design tool, these methods must be able to accurately represent all the important features of the penetration dynamics and the structural response of the EPW. The most desirable feature of an analytical procedure is that any parameter of interest can easily be adjusted and the analysis repeated in order to assess the influence of the parameter on system performance.

Two different types of EPW analyses have been established. The first is one in which the system (both the EPW and target) is represented by a very simple mathematical system involving only a few parameters.^{[1,2]*} These parameters are selected on the basis of fitting the results of the analyses with available test data.

*Numbers in brackets designate references at end of report.

This approach is semi-empirical in the sense that system model and parameter definitions require an extensive experience base. Such models are not suitable for investigating system performance in areas where data is unavailable or inadequate, nor for determining detailed physical mechanisms which govern the impact processes and ultimately the survivability of the EPW.

The second analytical method which has been developed is one based on first principles of physics, i.e., on the basic non-linear dynamical theories which characterize the physics of the penetration.^[3-7] The complexity of these theories is rather formidable and the development of an analysis tool using first principles is a difficult task requiring extensive experience with analytical methods and computer analysis capabilities.

This latter approach to the analytical investigation of the EPW penetration dynamics problem is the method presented in this report. In detail, this analysis is decoupled into two separate analyses, the first of which is an analysis of the penetration of a rigid projectile into the target material and the second the analysis of a deformable penetrator. This decoupled approach, which is valid only if the missile structure is nearly rigid throughout the penetration, has been investigated and validated in earlier works.^[3-5] The projectile has mass and inertial properties as well as prescribed initial velocity and flight attitude (yaw and obliquity). This problem is a true three-dimensional impact problem since the projectile attitude and flight direction is not perpendicular to the target.

To investigate this complex penetration problem, a new three-dimensional explicit finite difference code was developed. This code, named TRIFLE (for three-dimensional Fourier Lagrangian-Eulerian analysis) is capable of analyzing nonlinear nonaxisymmetric impact problems, such as the yawed impact of the EPW into

the target. The key results obtained by this analysis are the forces and rigid body accelerations to which the EPW is subjected during impact.

The second analysis, which requires the forces generated by the TRIFLE code, is a detailed analysis of the structural response of the EPW. This analysis is generated using a nonlinear dynamic, elastic-plastic finite element program CRT/NONSAP, which is capable of modeling all pertinent details of the structure of the projectile during the impact.

This two-part analytical study determines a) the impact environment to which the penetrator is subjected by means of the TRIFLE code, and b) the response of the penetrator to its impact environment via the CRT/NONSAP code. Both the TRIFLE and the CRT/NONSAP codes are first principle codes requiring knowledge of only material properties of target and EPW, and initial impact flight velocity and attitude.

This decoupled analysis procedure is used to simulate the 0.284-scale 1521 ft/sec 3° yawed reverse ballistic test (RBT) conducted by AVCO and Sandia Laboratories.^[8,9] The results of this penetration simulation will be shown to agree closely with the experimental results, thus demonstrating the capability of the method for predicting EPW impact response.

The TRIFLE computer code is then used to perform several analyses of EPW impacts at different velocities, flight attitudes (obliquity and yaw) and for different geometric configurations of the forward end of the projectile. These analyses show that, for a given target material, impact velocity and yaw are key parameters, with slight (<20°) obliquities of less consequence. Also, it appears that details of the design of the forward end of the EPW can be used to reduce the harshness of the impact environment.

The basic mathematical formulations used in the development of the TRIFLE code and the special features required to perform EPW penetration calculations are presented in Section 2. Also, a brief description is given of preliminary code verifications prior to the comparison with the results of the 0.284-scale RBT experiments.

Section 3 presents in detail the TRIFLE analysis of the 0.284-scale 3° yawed impact RBT, including detailed definitions of the target material, computational grids and calculation procedures. The determination of the impact forces applied to the penetrator is described in detail since these forces are the basic information required in order to determine the structural response and assess the survivability of the EPW.

The details of the CRT/NONSAP computer simulation of the 0.284-scale EPW response are presented in Section 4, including the finite element model used to represent the missile and the procedure used to construct the impact forces compatible with this analysis. The results are compared with the experimental data.

Section 5 presents the results of a parametric study using the TRIFLE code to investigate effects of yaw, obliquity, and initial velocity, as well as geometry of the penetrator.

Finally, Section 6 gives both a review of the results of this investigation and recommendations for directions of future analyses of EPW penetration problems.

SECTION 2

TRIFLE PENETRATION DYNAMICS CODE

The TRIFLE computer code is a three-dimensional explicit finite difference computer program specifically developed for investigating nonlinear nonaxisymmetric penetration problems. The computer program is a major modification of the two-dimensional explicit Lagrangian code WAVE-L, which is based on the HEMP scheme.^[10] Thus, the code has the same material modeling capabilities and abilities to track large scale motion found in the WAVE-L code, but has the capability of tracking nonlinear dynamic response for full three-dimensional systems. In TRIFLE the basic field variables, rather than being defined as a function of two variables (x, y for planar problems or r, z for axisymmetric problems) are described in polar cylindrical coordinates (r, θ, z) . The primary feature of this code is that all geometry and response quantities are represented by means of truncated Fourier series in the circumferential angle θ . Of course, since the problem is nonlinear, the various components proportional to $\cos k\theta$ (or $\sin k\theta$), $k = 0, 1 \dots N$ are coupled together, e.g., components proportional to $\cos m\theta$ couple with those proportional to $\cos n\theta$, when $m \neq n$.

This mathematical scheme, which is capable of treating general three-dimensional problems, may be expected to provide very efficient modeling for problems which possess some degree of axisymmetry in layout, i.e., problems whose initial geometry can be characterized by means of truncated Fourier series similar to the ones used to describe the field variables. Thus, the non-normal, asymmetric, rigid penetrator impact problem is ideally suited for analysis by the TRIFLE code. As will be detailed in the TRIFLE formulation, the full three-dimensional equations of motion are solved using a) a moving cylindrical coordinate

reference frame aligned with the penetrator axis, b) the Fourier representation described on specified Fourier grid planes, c) arbitrary Lagrangian-Eulerian (ALE) transformation to allow these grid planes to remain planes and d) momentum exchange logic to determine forces on the rigid penetrator. The mathematical formulation is described in the following.

2.1 MATHEMATICAL DEFINITIONS

In TRIFLE the equations of motion which characterize the medium are expressed in polar cylindrical coordinates (r, θ, z) which, for purposes of the EPW penetration analysis, are aligned with (but not attached to) the penetrator axis. The equations are

$$\frac{\partial T_{rr}}{\partial r} + \frac{1}{r} \frac{\partial T_{\theta r}}{\partial \theta} + \frac{\partial T_{zr}}{\partial z} + \frac{1}{r} (T_{rr} - T_{\theta\theta}) + \rho b_r = \rho \dot{v}_r$$

$$\frac{\partial T_{r\theta}}{\partial r} + \frac{1}{r} \frac{\partial T_{\theta\theta}}{\partial \theta} + \frac{\partial T_{z\theta}}{\partial z} + \frac{1}{r} (T_{r\theta} + T_{\theta r}) + \rho b_\theta = \rho \dot{v}_\theta$$

$$\frac{\partial T_{rz}}{\partial r} + \frac{1}{r} \frac{\partial T_{\theta z}}{\partial \theta} + \frac{\partial T_{zz}}{\partial z} + \frac{1}{r} T_{rz} + \rho b_z = \rho \dot{v}_z$$

In these equations, v_i ($i = r, \theta, z$) are velocity components, ρ denotes density, and b_i , T_{ij} are components of body force per unit mass and Cauchy stress, respectively. The dot denotes material time differentiation.

Since the basic computational grid used in TRIFLE is assumed to move arbitrarily in time, the material time derivative of any function f , is given by the expression

$$\dot{f} = \frac{\partial f}{\partial t} + (Vf)_i (v_i - v_i^g)$$

where $(\nabla f)_i$ is the i th component of the spatial gradient of f . Symbol v_i is the particle velocity and v_i^g is the specified grid velocity, both with respect to the moving reference frame used to describe the problem. The grid system in general may execute any specified motion from purely Eulerian ($v_i^g = 0$) to Lagrangian ($v_i^g = v_i$).

The rate of deformation D_{ij} is given by the relations

$$\begin{aligned} D_{rr} &= \frac{\partial v_r}{\partial r} & D_{\theta\theta} &= \frac{1}{r} \frac{\partial v_\theta}{\partial \theta} + \frac{v_r}{r} & D_{zz} &= \frac{\partial v_z}{\partial z} \\ D_{r\theta} &= \frac{1}{2} \left(\frac{1}{r} \frac{\partial v_r}{\partial \theta} + \frac{\partial v_\theta}{\partial r} - \frac{v_r}{r} \right) & D_{rz} &= \frac{1}{2} \left(\frac{\partial v_r}{\partial z} + \frac{\partial v_z}{\partial r} \right) \\ D_{\theta z} &= \frac{1}{2} \left(\frac{\partial v_\theta}{\partial z} + \frac{1}{r} \frac{\partial v_z}{\partial \theta} \right) \end{aligned}$$

The equation of continuity is

$$\frac{1}{\rho} \dot{\rho} + \frac{1}{r} \frac{\partial}{\partial r} (rv_r) + \frac{1}{r} \frac{\partial v_\theta}{\partial \theta} + \frac{\partial v_z}{\partial z} = 0$$

The constitutive relations used to describe the material require the usual stress measures

$$\begin{aligned} T_{rr} &= -P + S_{rr} & T_{r\theta} &= S_{r\theta} \\ T_{\theta\theta} &= -P + S_{\theta\theta} & T_{rz} &= S_{rz} \\ T_{zz} &= -P + S_{zz} & T_{z\theta} &= S_{z\theta} \end{aligned}$$

where S_{ij} are the deviatoric stress components and P denotes pressure. The material state is determined by

$$P = P(\rho, f_1, f_2, \dots)$$

and

$$F(J_2^I, Y_1, Y_2, \dots) = 0$$

where f_1, f_2, \dots are material parameters defining the pressure as a function of density. The symbol J_2^I denotes the second invariant of deviatoric stress and Y_1, Y_2, \dots are parameters used to describe F . The deviatoric stress rates estimated by use of elastic relations are:

$$\begin{aligned} \dot{S}_{rr} &= 2\mu \left(D_{rr} + \frac{1}{3} \frac{\dot{\rho}}{\rho} \right) & \dot{S}_{r\theta} &= 2\mu D_{r\theta} \\ \dot{S}_{\theta\theta} &= 2\mu \left(D_{\theta\theta} + \frac{1}{3} \frac{\dot{\rho}}{\rho} \right) & \dot{S}_{rz} &= 2\mu D_{rz} \\ \dot{S}_{zz} &= 2\mu \left(D_{zz} + \frac{1}{3} \frac{\dot{\rho}}{\rho} \right) & \dot{S}_{z\theta} &= 2\mu D_{z\theta} \end{aligned}$$

These equations are adjusted into order to satisfy the condition $F = 0$ [10]. This mathematical model is capable of representing a hysteretic, elastic-plastic material including dilatation. In essence, the model represents the material behavior in terms of variable shear and bulk moduli in both loading and unloading. With this model it is possible to represent fractured and crushed materials by degrading material properties through modification of the parameters f_i and Y_i .

As described earlier all field variables are presented by truncated N-term Fourier series. Thus, for example, the velocities are written

$$v_r = v_r^o + \sum_{n=1}^{N-1} v_r^n \cos n\theta$$

$$v_\theta = \sum_{n=1}^{N-1} v_\theta^n \sin n\theta$$

$$v_z = v_z^o + \sum_{n=1}^{N-1} v_z^n \cos n\theta$$

and stresses are expressed in the form

$$T_{rr} = T_{rr}^o + \sum_{n=1}^{N-1} T_{rr}^n \cos n\theta \quad T_{r\theta} = \sum_{n=1}^{N-1} T_{r\theta}^n \sin n\theta$$

$$T_{\theta\theta} = T_{\theta\theta}^o + \sum_{n=1}^{N-1} T_{\theta\theta}^n \cos n\theta \quad T_{\theta z} = \sum_{n=1}^{N-1} T_{\theta z}^n \sin n\theta$$

$$T_{zz} = T_{zz}^o + \sum_{n=1}^{N-1} T_{zz}^n \cos n\theta \quad T_{rz} = T_{rz}^o + \sum_{n=1}^{N-1} T_{rz}^n \cos n\theta$$

where

$$v_i^k = v_i^k(r, z)$$

$$i = r, \theta, z$$

$$T_{ij}^k = T_{ij}^k(r, z)$$

Note that this solution form is symmetric about the $\theta = 0^\circ - 180^\circ$ plane. This representation thus replaces the set of field variables defined over 3 space dimensions with N sets of field variables, each of which are defined over 2 space dimensions. Consequently, the physics of the problem is described on N independent Fourier planes

$$\theta_k = \frac{k-1}{N-1}\pi \quad k = 1, \dots, N$$

as shown on Figure 2.1. On each Fourier plane $(r, z, \theta = \theta_k)$ the problem is represented by means of a finite difference grid. At each grid point, the full three-dimensional equations are expressed in finite difference form.

Thus, for a grid with M grid points in both the r and z directions, the total number of points which must be considered is $N \times M^2$. It is important to recognize that all the Fourier components are coupled together since the equations are non-linear. Nevertheless, this approach is much less costly than a full finite difference model which has, for a similar volume of material $M \times M \times M$ grid points. Thus, the relative efficiency of the TRIFLE approach compared to a full finite difference grid is N/M . Since the number of terms in the truncated Fourier series is small compared with the number of grid points M in a typical direction in the computational grid, the TRIFLE approach will result in a major reduction in computational effort. This savings is especially significant when it is recognized that the modeling accuracy which can be achieved by a moderate number of Fourier planes is more than adequate for impact problems in which small yaw and obliquity is investigated. In fact, for an equivalent total number of grid points, the TRIFLE approach will always produce a better resolution of the physics near the impact site than an associated 3-D Cartesian grid.

- Define moving cylindrical coordinate (r, θ, z) reference frame aligned with rigid-body penetrator.
- Divide 3-D space of target medium into N circumferentially spaced ($\theta = \text{const.}$) "Fourier" $(r-z)$ planes.
- Define 2-D $(r-z)$ finite difference grid with 3-D particle velocity (v_r, v_θ, v_z) in each "Fourier" plane.
- Couple planes together with N -term Fourier series which define circumferential variation of parameters
- Introduce arbitrary Lagrangian-Eulerian (ALE) transformations so that the planes remain planes.
- Satisfy full 3-D equations of motion in each "Fourier" plane.
- Determine forces on penetrator using momentum exchange with target medium.

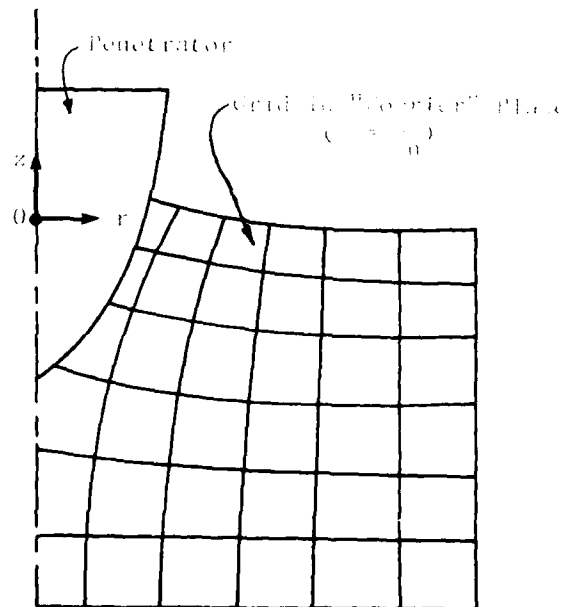
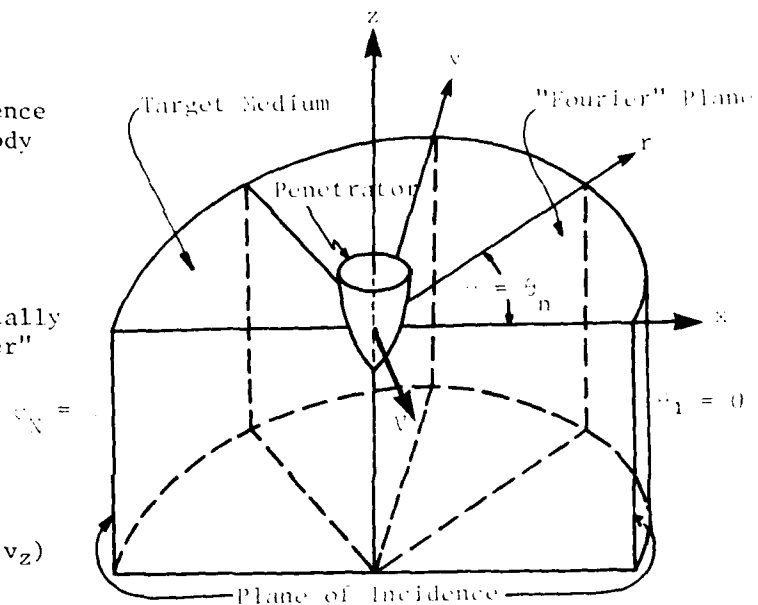


Figure 2.1. Basic Concepts of TRIFLE Code.

2.2 COMPUTATIONAL FEATURES

The basic computational scheme employed in the TRIFLE code, shown in Figure 2.2, follows the explicit time integration scheme used by WAVE-L and the HEMP family of codes.^[10] The primary modifications in the TRIFLE code are as follows (see Figure 2.1):

- 1) The full three-dimensional equations of motion must be generated at each grid point on each Fourier plane. These equations, in general, involve all the Fourier components of the field variables. Gradients for field variables in circumferential (θ) direction are explicitly formed.
- 2) The cylindrical coordinate system is aligned with rigid penetrator axis for the impact calculation, with the origin located in the plane of the initial impact site.
- 3) On each Fourier plane the computational grid is not permitted to deform out of the r-z plane by means of the arbitrary Lagrangian-Eulerian (ALE) transformation. The deformed planar grids are also rezoned for computational efficiency.
- 4) Due to the maintainance of the computation planes and the alignment of the coordinate system with the penetrator axis, material flows through the Fourier grid system.
- 5) For the rigid penetrator, the momentum exchange between target and penetrator is used to determine forces on the penetrator and update the rigid body response of the penetrator.

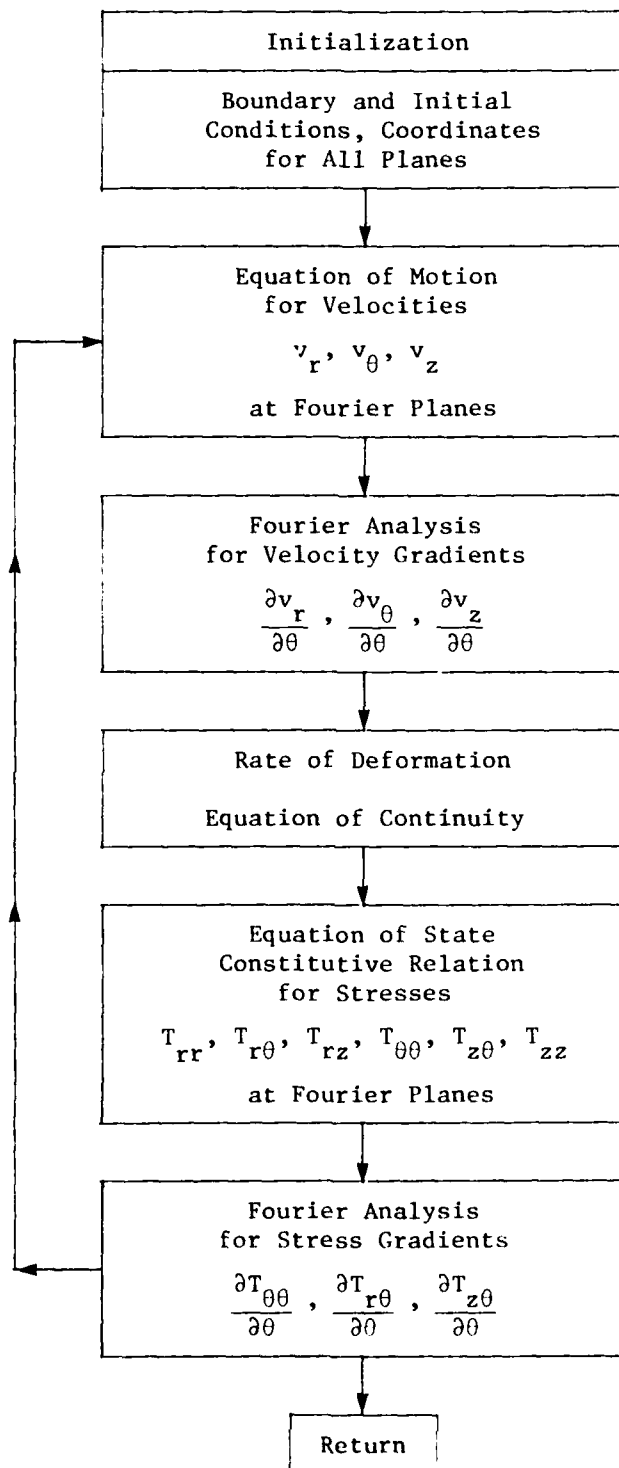


Figure 2.2. 3-D Code Analysis - Computation Scheme.

The rigid body representation of the penetrator was employed to provide the best combination of modeling accuracy and economy.^[4] While a fully deformable penetrator can be analyzed in the penetrator/target response calculation using the TRIFLE code, a simulation of the details of the penetrator structural response would require a very fine grid. Apart from the increased size of the problem in terms of numbers of variables, this grid would require a much smaller time step for numerical stability and would be much more costly to use.

To assist the user of TRIFLE, a complete graphical software system has been developed. The system is capable of displaying all relevant data and grid systems (deformed or undeformed) on each Fourier plane for arbitrary time slices. As will be evident from the results shown in Section 3, the plot system is an essential part of the TRIFLE code since it provides the capability of visualizing as clearly as possible the complex impact processes which come into play during penetration.

2.3 CODE VERIFICATION

In order to verify the TRIFLE concept and check out the computer program, a number of 2-D test cases were analyzed using the (3-D) TRIFLE code and compared with other available analyses. These included

- a) Plane strain dynamical loadings on pipes, both ideal Fourier distributions and nonideal distributions
- b) Dynamical loadings on moving solid cylinders in plane strain
- c) Axisymmetric rigid body penetrations (normal impact)

The TRIFLE code proved capable of giving essentially identical results to those obtained by other analyses. Of course, the

full three-dimensional capabilities of the code can only be checked out by analyzing a full three-dimensional problem and comparing the results with either the results of another 3-D computer code or experimental data.

The latter approach was used to prove the fidelity of TRIFLE. The 0.284-scale 3° yawed impact RBT was the test which was used as a benchmark. For this test the penetrator was extensively instrumented and a great deal of experimental data was available. [8,9] Since the test results can only be obtained numerically by first using the TRIFLE code to simulate the penetration dynamics, and then applying the forces generated by TRIFLE to a CRT/NONSAP finite element model, the proof of the code involves

- a) an accurate TRIFLE solution
- b) an accurate method of interfacing the TRIFLE solution with the CRT/NONSAP code
- c) an accurate CRT/NONSAP code

An important aspect of this study is the development of accurate mathematical models of the materials in both the penetrator and the target.

As will be shown in Section 4, the comparison between test results and the numerical analysis is very favorable, thus validating the TRIFLE analysis of asymmetric impact problems.

SECTION 3

PENETRATION DYNAMICS OF YAWED IMPACT

The impact of a penetrator into a target is a true three-dimensional problem if the impact is other than normal to the target. This situation occurs if the flight trajectory is non-normal (obliquity) and/or the missile axis differs from the line of flight (yaw). For non-normal impact, see Figure 3.1, the face of the penetrator most directly exposed to the target, termed the upstream face, encounters a more severe impact environment than the downstream face. Thus, the impact forces on each face will differ, so that lateral force resultant as well as axial force resultants will be generated on the forward end of the penetrator. These lateral forces will produce severe lateral and rotational accelerations along with the expected axial accelerations. Together, these impact forces will generate intense stress levels which may result in structural damage or failure.

Since the stress analysis of the penetrator during impact requires a detailed knowledge of the time dependent surface tractions between target and penetrator, the TRIFLE code is used to analyze the penetrator/target impact in order to determine

- a) details of the tractions on the interface of the penetrator and target, and
- b) gross axial, lateral and angular accelerations of the missile.

In the TRIFLE calculation, the penetrator is represented as a rigid body free to undergo rigid body linear and angular accelerations developed during the penetration. For this analysis the origin of the coordinate system is constrained to remain in the plane defined by the initial target surface and the z axis is aligned with the penetrator throughout the impact. As a result,

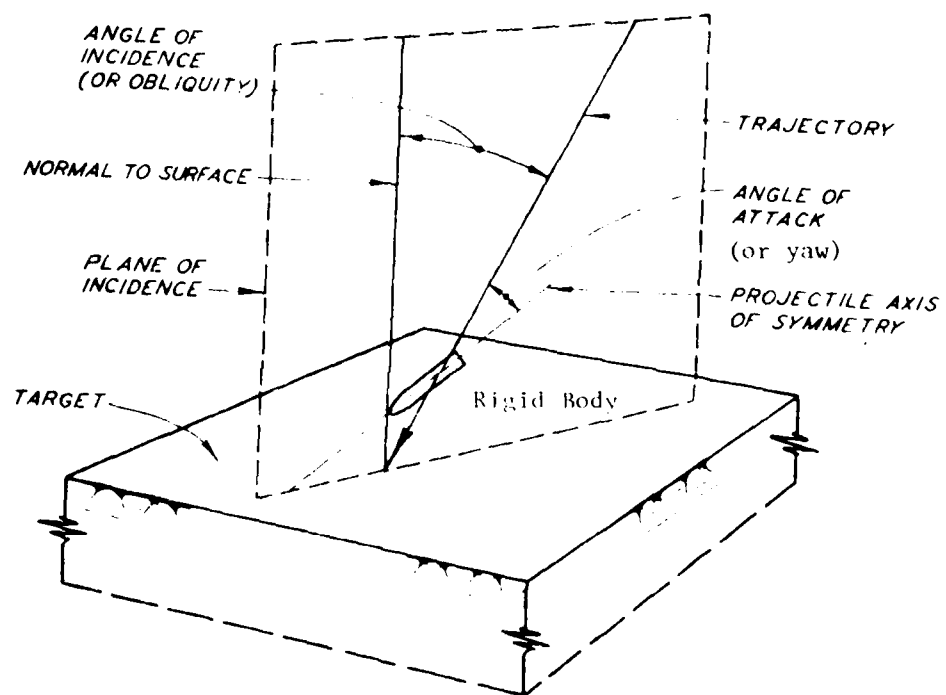


Figure 3.1. Geometry of Oblique, Yawed Impact Problem.

the grid system which describes the target undergoes rigid body motion in addition to the in-plane distortion developed by the impact. It is important to recognize that the grid system is not axisymmetric, even at the beginning of the impact, but rather skewed, reflecting the obliquity and yaw of the missile flight. As a result, each Fourier plane will have a different grid system, although the mesh on each Fourier plane is a distorted version of the one on another plane. This is because the grid locations (as well as all the other variables required to describe the problem) are represented by truncated Fourier series in the angle θ .

The details of the penetrator and target are shown in Figure 3.2. The 0.284-scale penetrator has a nominal length 18.15 in. and is machined from 300-M steel. The interior of the missile is hollow, except for a cylinder of Kennertium ballast in the forward end and accelerometer packages near the center of mass and in the aft end. Strain gauges are also attached at several points on the interior and exterior surfaces of the structure.

The target material is Dakota sandstone^[11] with properties indicated in the figure. The mathematical model developed by CRT^[12] which describes this material is a hysteretic, elastic-plastic associated flow model with variable bulk and shear moduli in loading and unloading. The material is assumed to strain harden to the fracture point and then strain soften after fracture in order to account for degraded strength properties representative of crushed sandstone. The friction rule at the target/projectile interface assigns zero strength for positive tension ($\sigma_n > 0$) and takes the form

$$\tau = 0.19\sigma_n \exp(-\sigma_n/1.6)$$

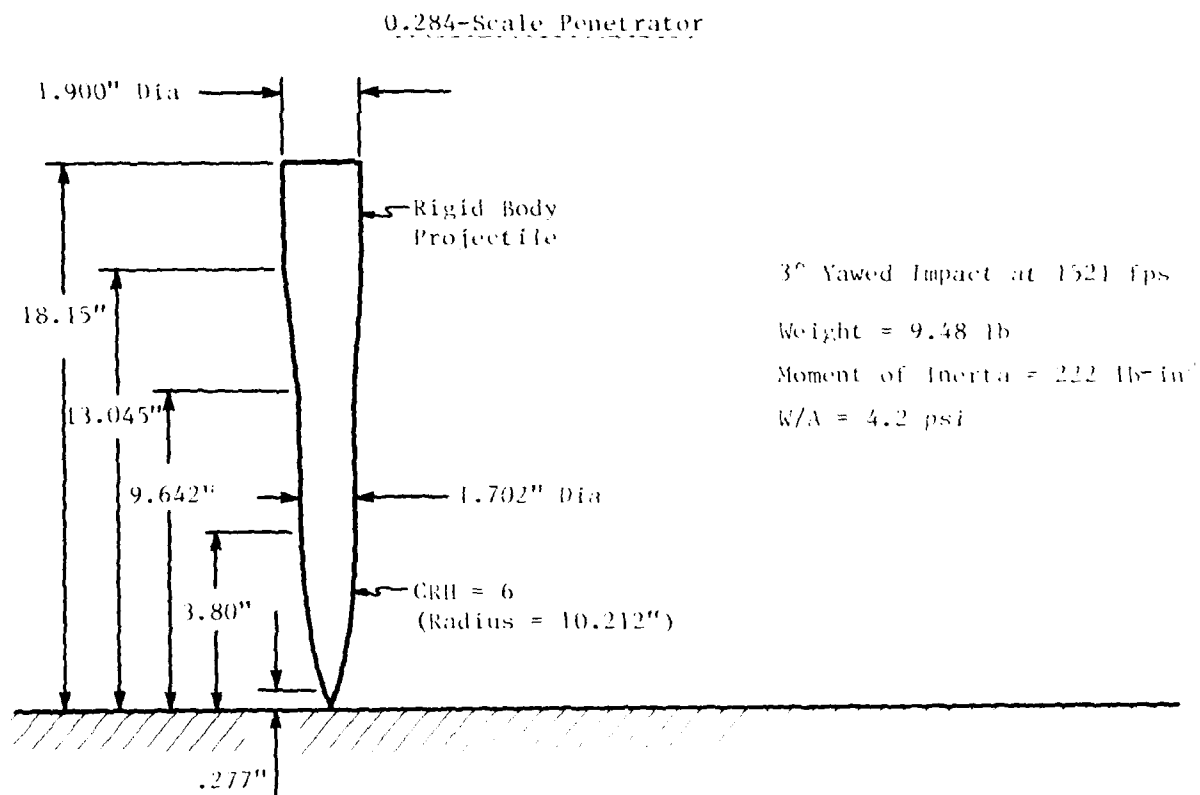


Figure 3.2. Penetrator and Target Data.

when $\sigma_n < 0$, where τ is the maximum shear stress and σ_n is the compressive stress (both measures in kb). This material model has been validated in previous penetration studies.^[4]

The penetrator is assumed to have an initial impact flight velocity of 1521 ft/sec and to have 0° obliquity and 3° yaw, i.e., to have a flight direction normal to the target, but a slight yaw.

Figures 3.3 and 3.4 are views of the penetrator and the target grid (0° - 180° planes only) at the beginning of the impact problem. Note that the yaw requires a target grid which is appropriately skewed on each plane. For this analysis five Fourier planes were used, with a total of 9900 grid points required. The boundaries on the outside edge of each plane and the bottom were assumed to be fixed. Finally, the grid points on the line defined by the penetrator axis were coincident until such time as the penetration process produced separation of the target.

The layout of the grid is dictated by the usual requirements imposed on finite difference calculations, namely that the aspect ratio of the grid cells not be too large and that the size of the cells vary slowly. In addition, the overall dimensions of the computational grid was established to match the dimensions of the target; however, in this calculation, the boundaries were assumed fixed. For this configuration no waves reflected by the grid boundaries encounter the penetrator prior to $\sim 800 \mu\text{sec}$. As will be seen from the solution, these reflected waves influence physical characteristics of the target, but do not appreciably alter the penetrator response of interest during the time $800 \mu\text{sec} < t < 1000 \mu\text{sec}$.

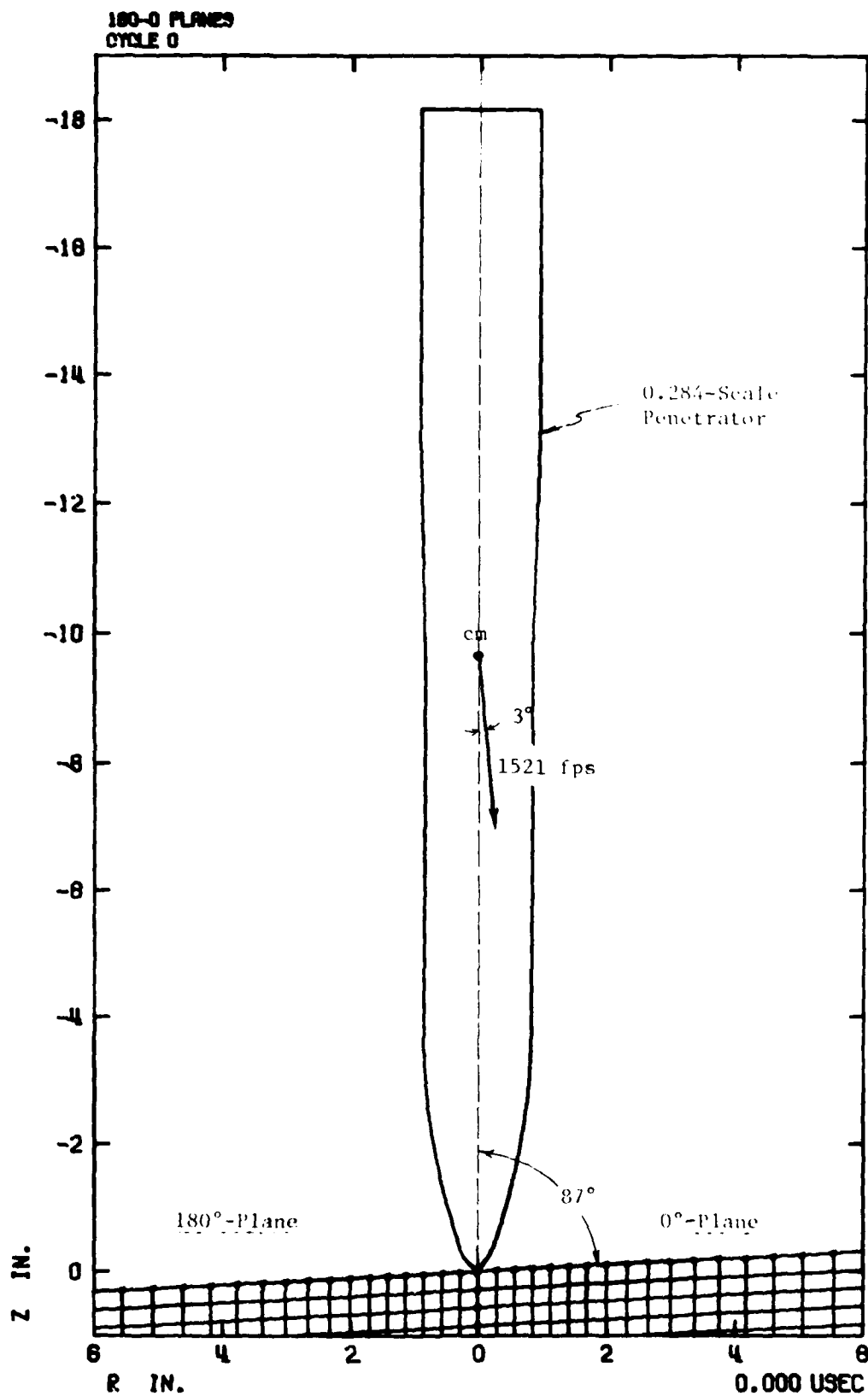
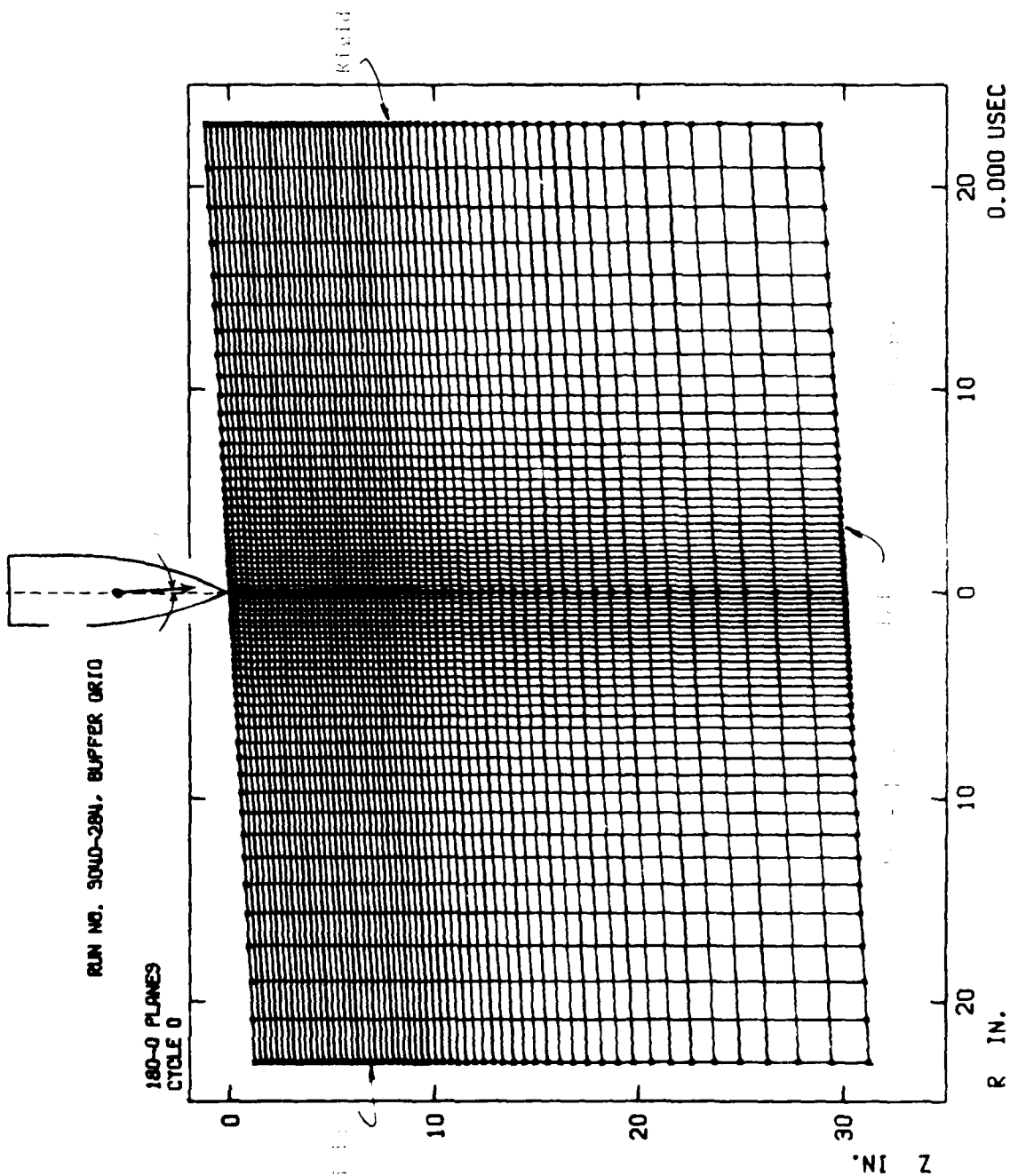


Figure 3.3. RBT Penetrator for 3° Yawed Impact at 1521 fps into Dakota Sandstone Target (in 180° - 0° Planes).

RUN NO. 5040-284, BUFFER OR 10

180-0 PLANES
CYCLE 0



180-0 PLANES
CYCLE 0

For purposes of numerical stability, the calculation required a time step of approximately 1 μ sec, although the step size varied throughout the analysis. The analysis was carried forward in time until the penetrator was fully embedded in the target, i.e., for approximately 1000 μ sec after impact, which required 962 time steps.

Grid plots of the TRIFLE solution are shown for increasing time $t = 100, 180, 380, 525, 800$ and 1000μ sec in Figures 3.5 through 3.10, respectively. The grid plots, which show both the 0° and 180° planes indicate the buildup of non-axisymmetric response, with development of contact all along the upstream face of the penetrator for $t > 500 \mu$ sec and contact only along the forward portion of the upstream face for all times. Although it is not so clearly demonstrated in the grid plots of the early phases of the penetration, the resultant forces generated by the impact have a very substantial lateral component. This is better shown by examining plots of axial, lateral and angular acceleration, shown in Figures 3.11, 3.12 and 3.13, respectively. (Obviously, the arrival of the reflected wave off the fixed boundary produces a significant change in the target material with significant changes in rigid body motion after $\sim 800 \mu$ sec.)

These results show a sharp early rise in axial deceleration to approximately 150 μ sec and then a more gradual increase during the remaining time. Both the lateral and angular accelerations are characterized by a large peak with a maximum near 150 μ sec and then a decrease to a rather constant level for $250 < t < 600 \mu$ sec. As will be seen, this large peak is very important in defining the primary aspects of structural response. These large lateral and angular rotations are due to large lateral force resultants applied to the forward end during the early stages of the impact.

BUFFER CASE

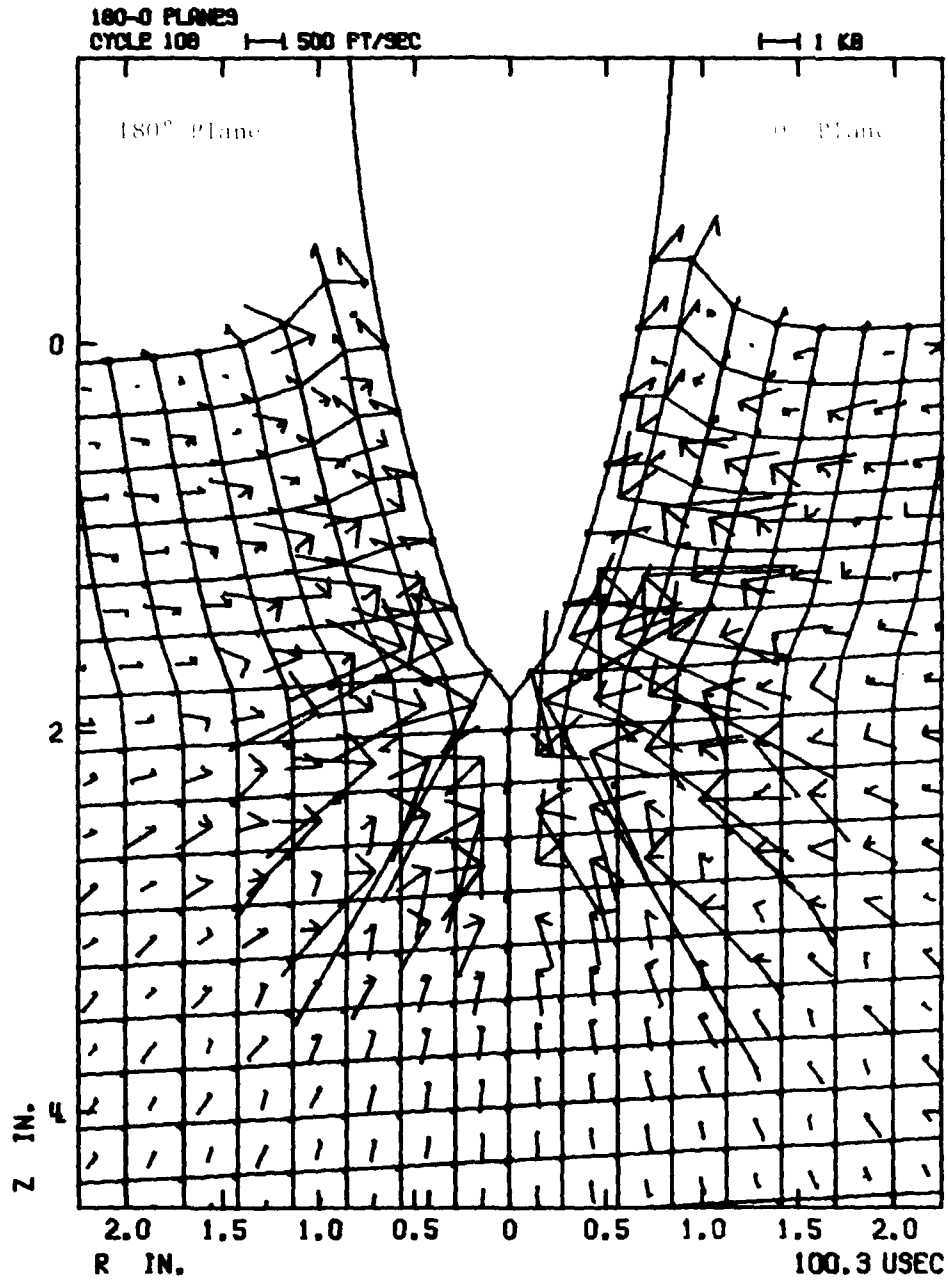


Figure 3.5. Principal Stress, Particle Relative Velocity and Grid Configuration in 180° - 0° Planes at 100 μ sec.

BUFFER CASE

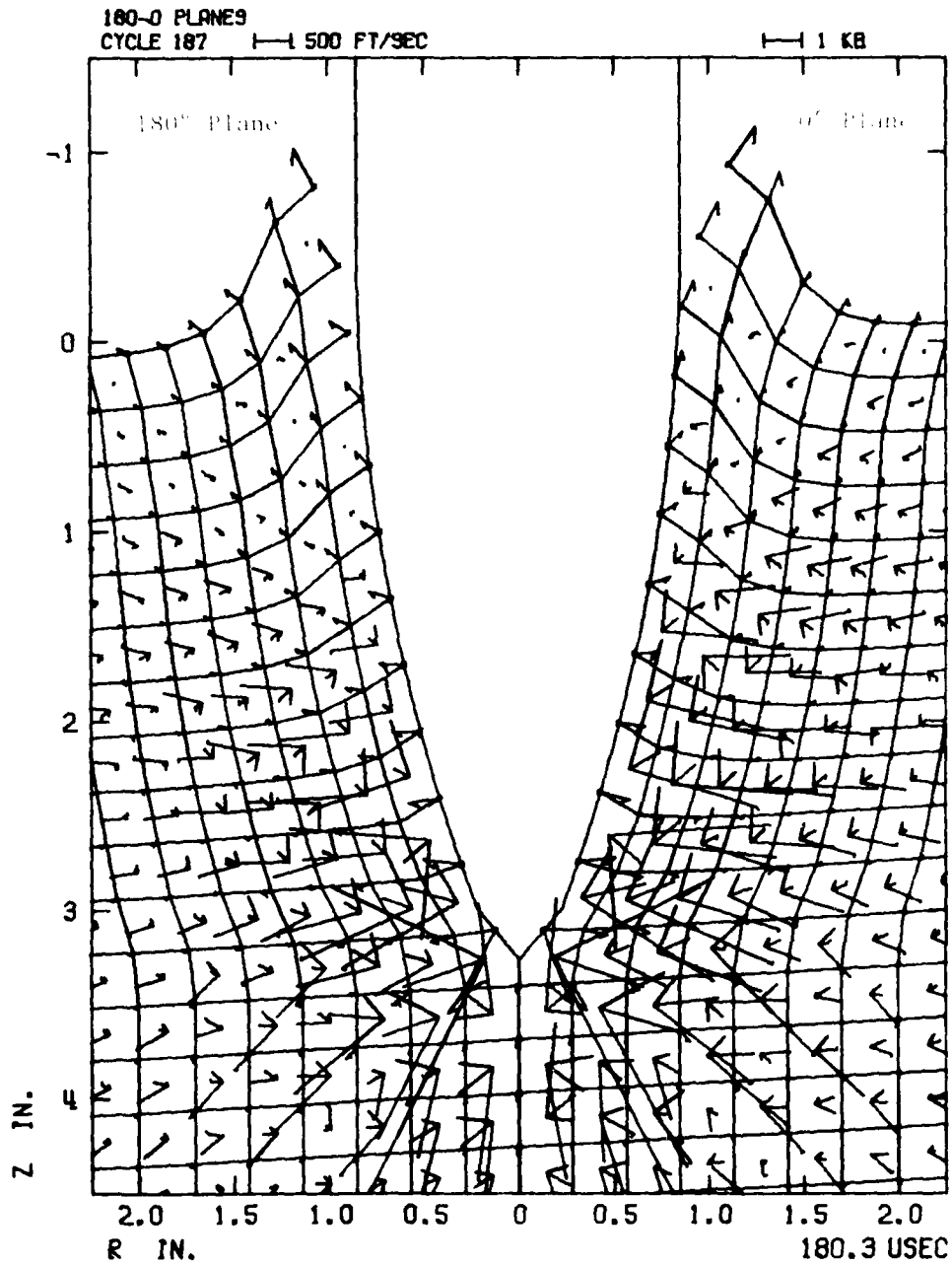


Figure 3.6. Principal Stress, Particle Relative Velocity and Grid Configuration in 180° ~ 0° Planes at 180 usec.

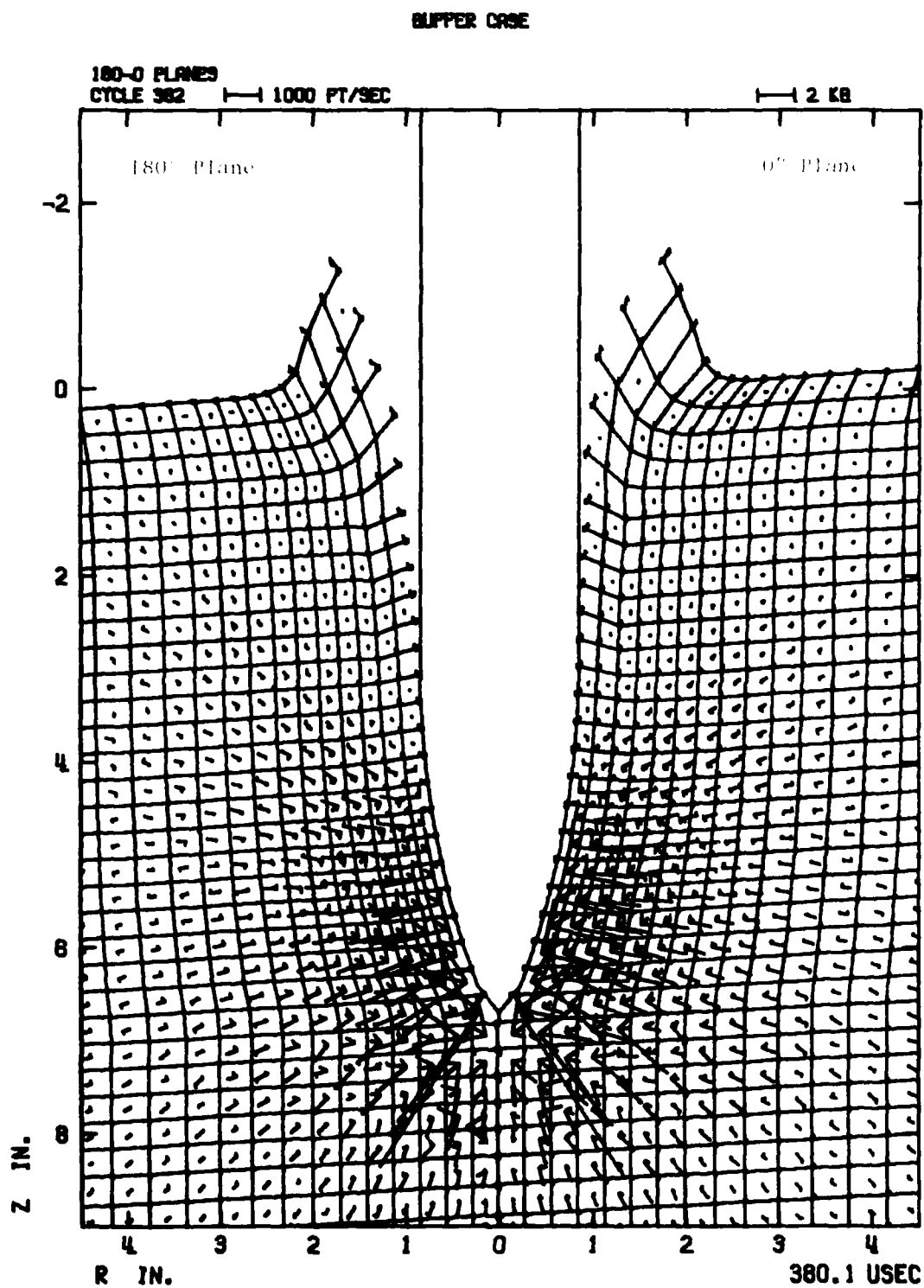


Figure 3.7. Principal Stress, Particle Relative Velocity and Grid Configuration in $180^\circ - 0^\circ$ Planes at 380 psec.

BUFFER CASE

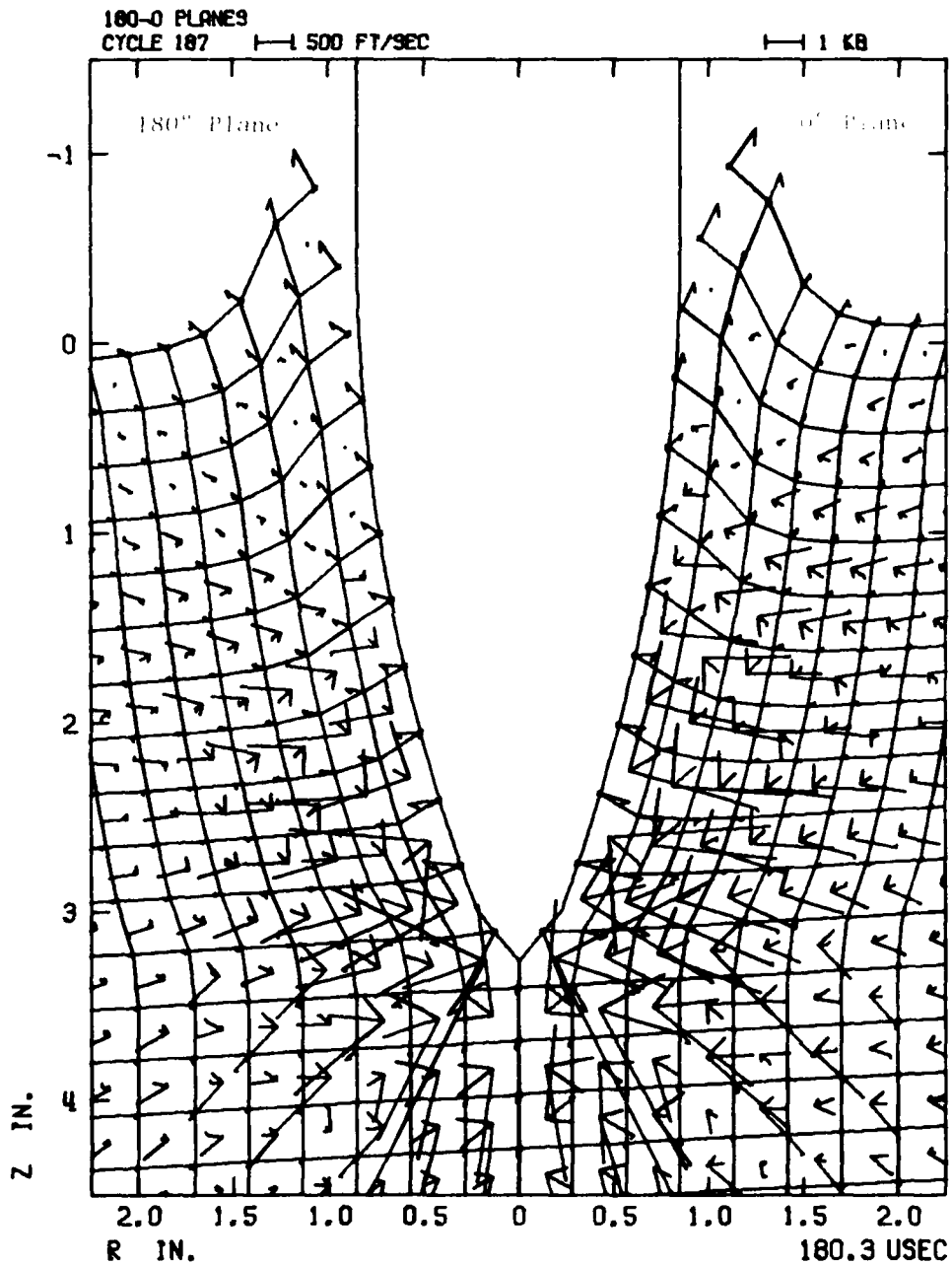


Figure 3.6. Principal Stress, Particle Relative Velocity and Grid Configuration in 180° - 0° Planes at 180 μsec.

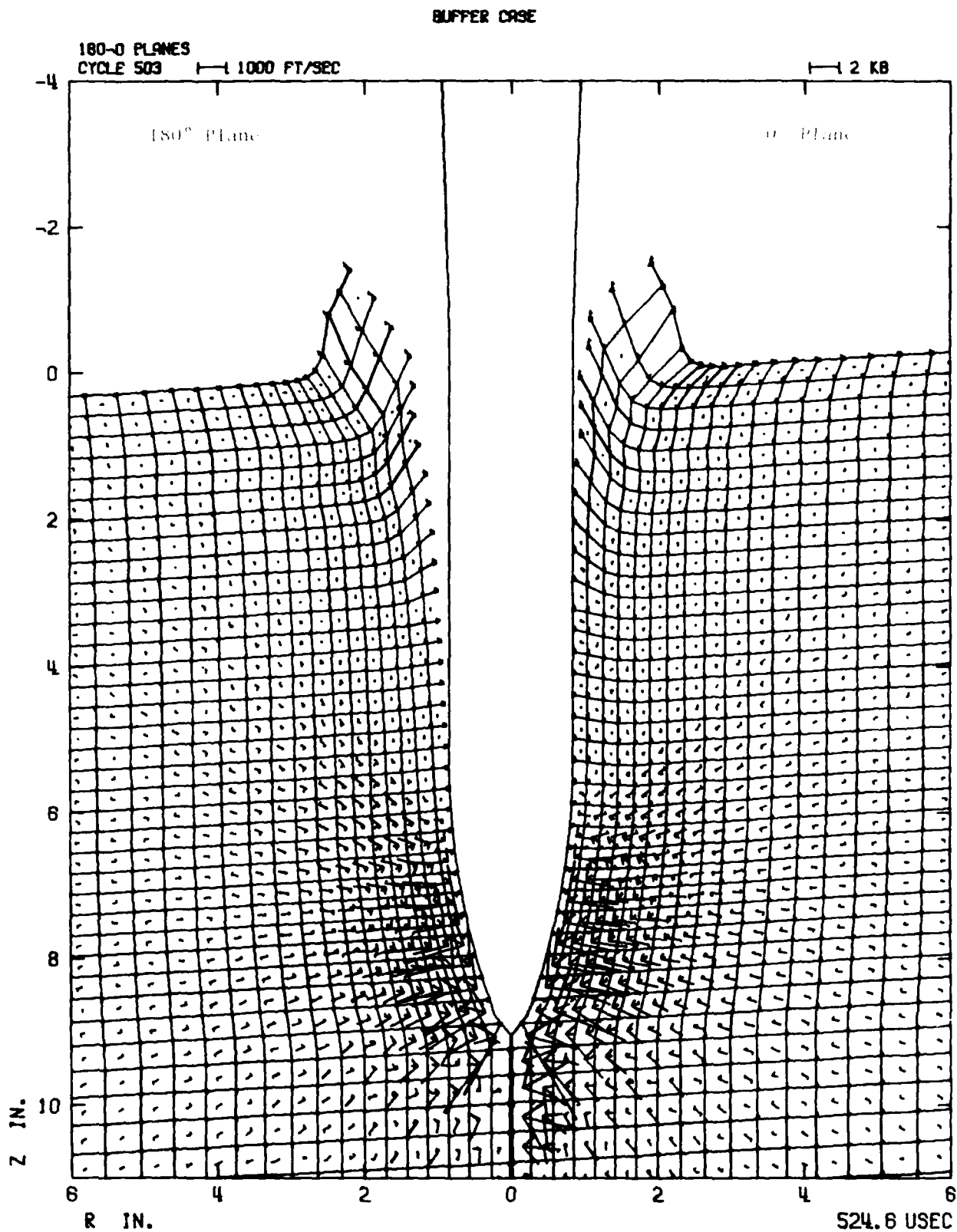
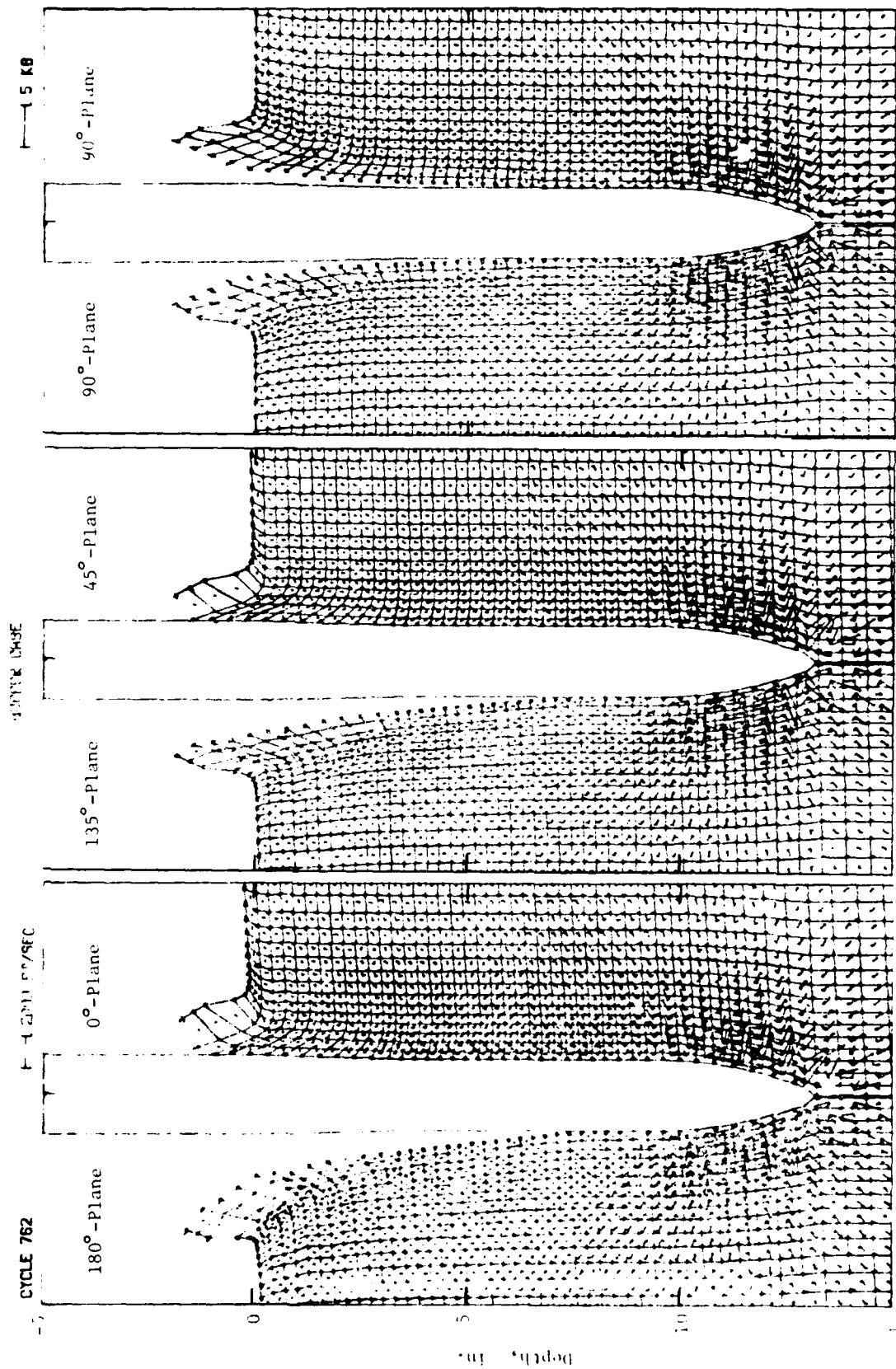


Figure 3.8. Principal Stress, Particle Relative Velocity and Grid Configuration in 180° - 0° Planes at 525 μsec.



800.2 USEC

Radius, in.

Figure 3.27. Principal Stress, Particle Velocity and Grid Configuration in All Planes at 800.2 usec.

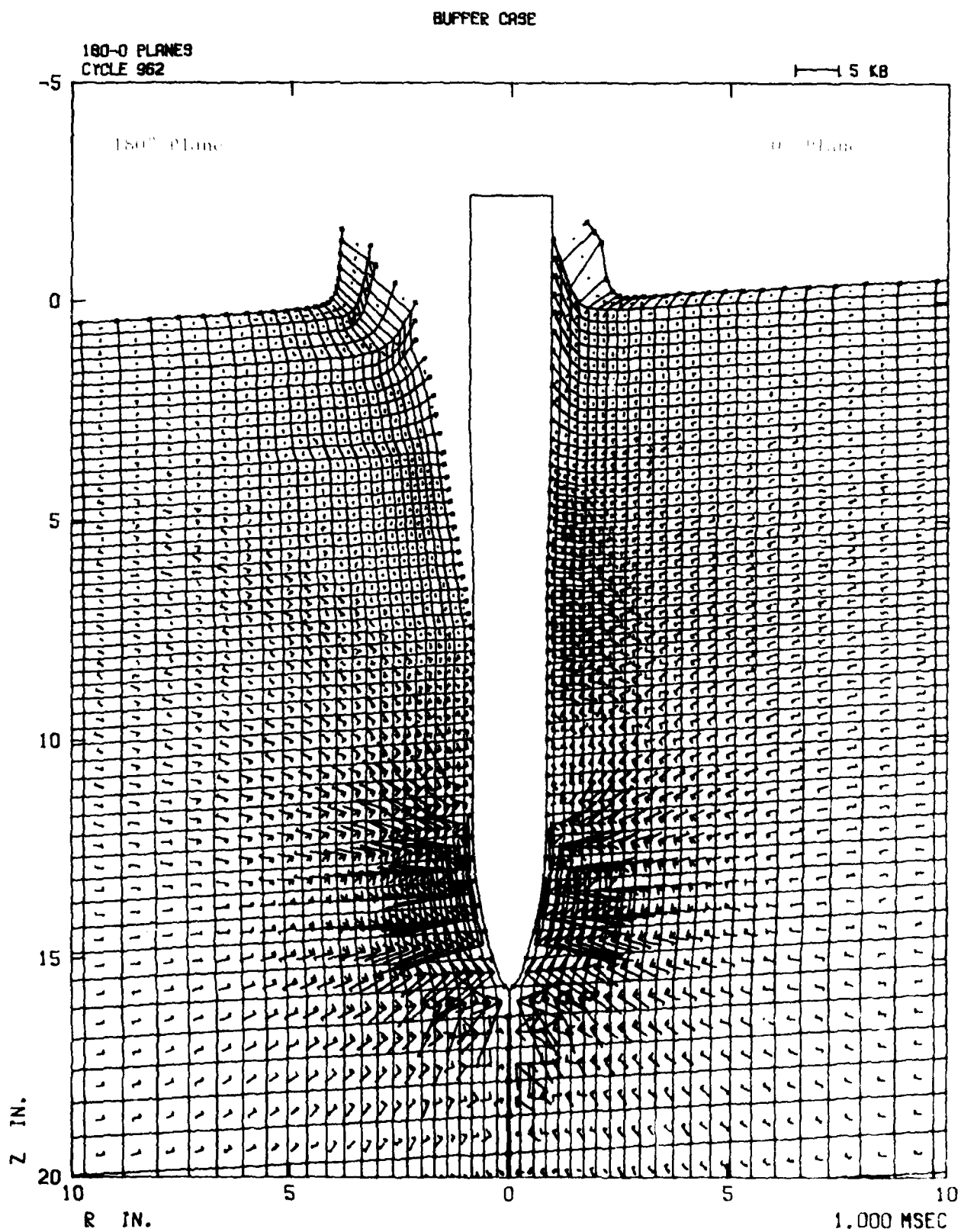


Figure 3.10. TRIFLE Code Solution (Stream and Grid Contour Lines) of 3° Yawed-Impact and Body Length Penetration of 0.234 (Scale RBL).

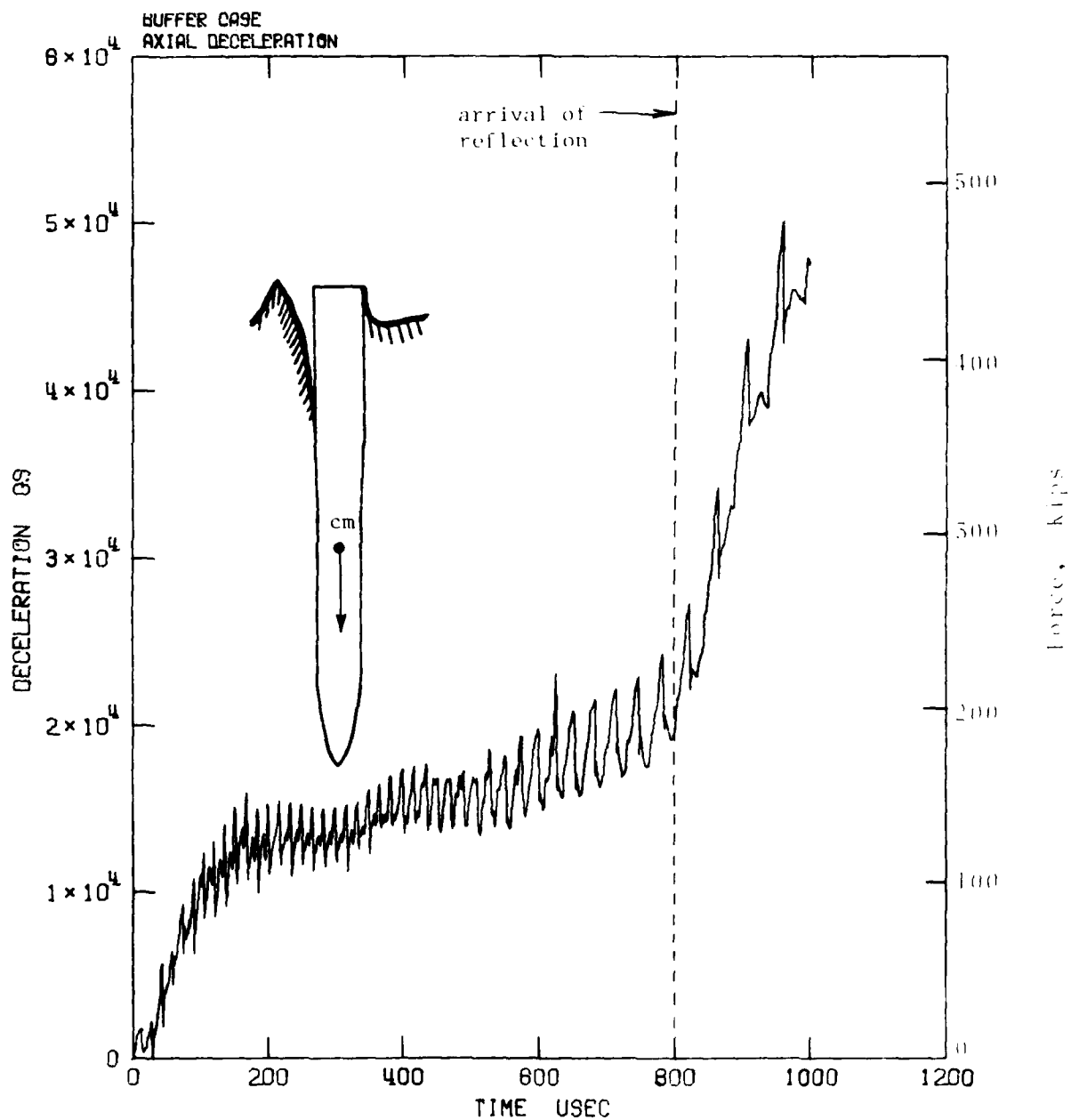


Figure 3.11. Penetrator Axial Deceleration and Force Time History.

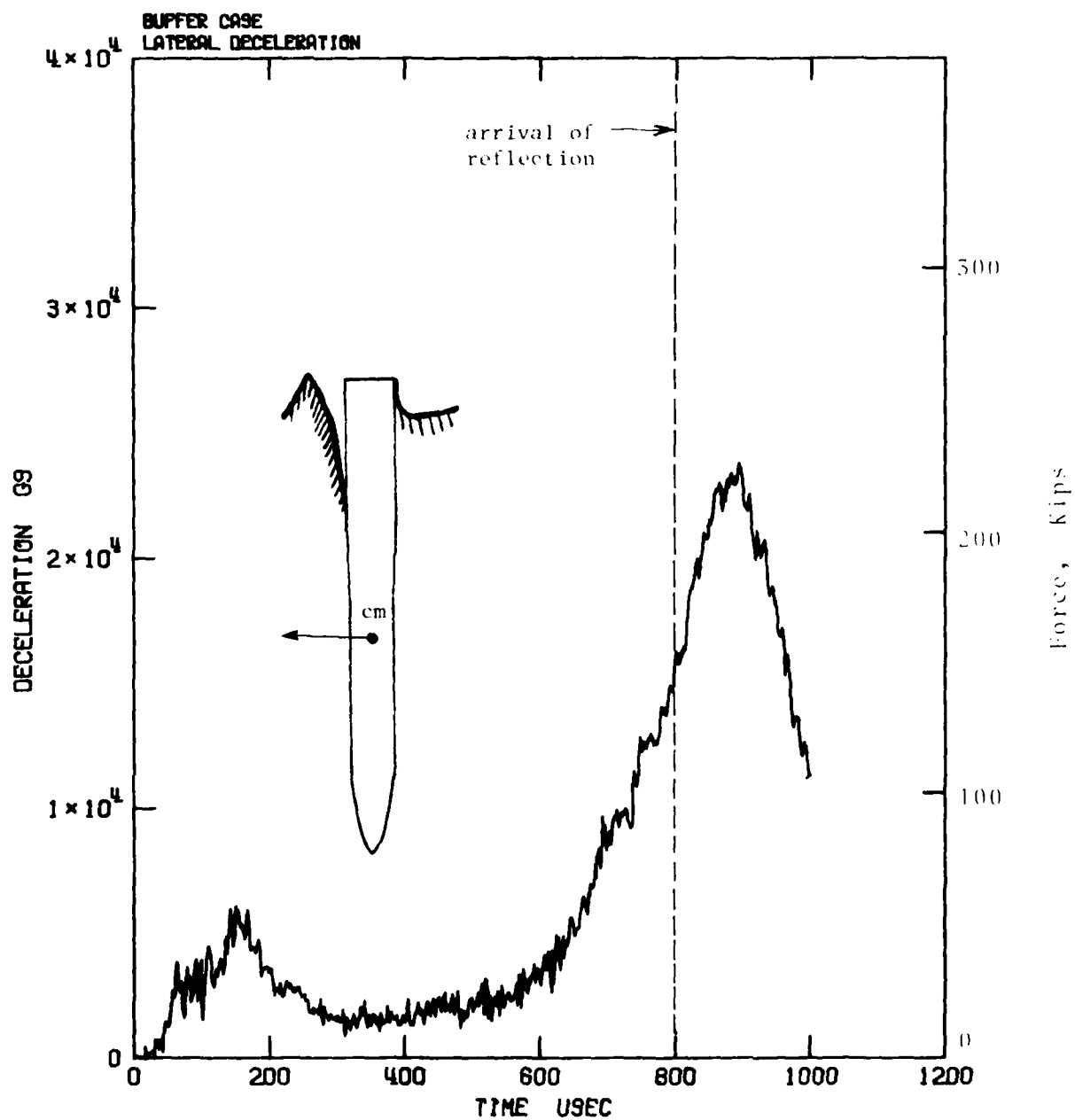


Figure 3-12. Penetrator Lateral Deceleration and Force Time History.

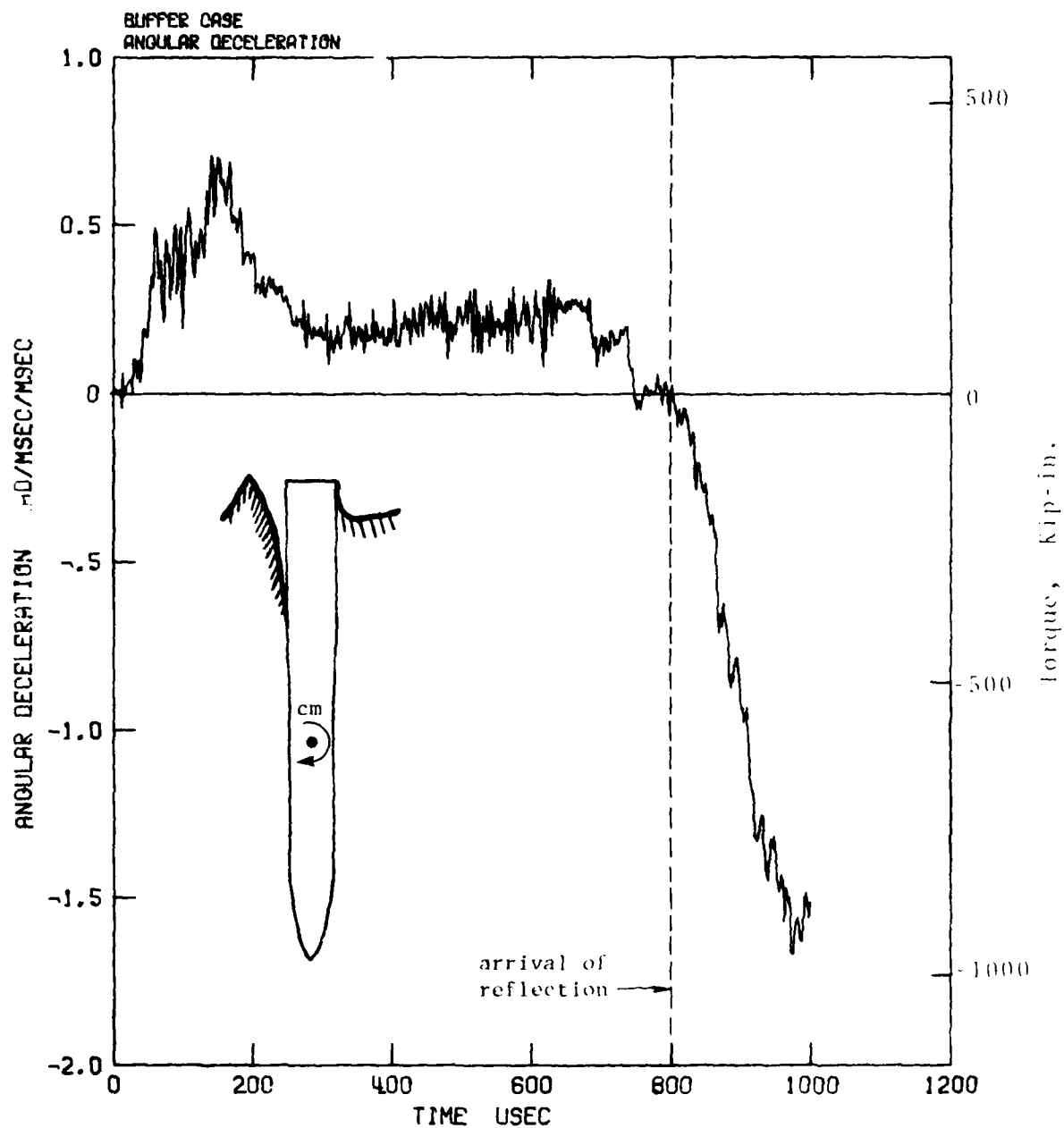


Figure 3.13. Penetrator Angular Deceleration and Torque Time History.

As may be seen from these rigid body accelerations for times greater than $\sim 600 \mu\text{sec}$, the lateral acceleration begins to increase sharply and the angular acceleration begins to decrease. This is due to the involvement of the central portion of the upstream side of the penetrator with the target, resulting in a large lateral force/length whose centroid lies on the aft side of the center of mass. Thus the aft body involvement tends to stabilize the flight attitude by reducing rotational accelerations.

The primary information required for a detailed structural analysis is a time history of the tractions encountered by the penetrator during the impact. This information is generated by determining the stresses in the elements directly adjacent to the penetrator and making use of their truncated Fourier representations. Figure 3.14 indicates tangential and normal stresses on the five Fourier planes at $800 \mu\text{sec}$, together with equivalent distributed line loads. Note that normal stresses and equivalent distributed line loads are very high compared with the tangential stresses and associated axial force distributions. However, the axial force distributions all act in the same direction, while each lateral line load acts in a particular Fourier plane perpendicular to the axis of the missile. As a result, the relatively small axial forces on each plane add to produce a larger axial force resultant, the largest portion of which is distributed along the nose of the penetrator. By comparison the large lateral line loads on each Fourier plane act in different directions and develop a relatively small lateral force resultant. Note from the figure that the intense lateral loads in the forward end of the missile are distributed in a nearly symmetric manner about the 90° Fourier plane, but that in the middle/aft section the loads are only on the 0° and 45° planes. This is due to the involvement of the upstream (0° , $\pm 45^\circ$) face of the penetrator and the target, and the lack of contact between target and penetrator on its downstream face.

BUFFER CASE 84

CYCLE 782 800 USEC

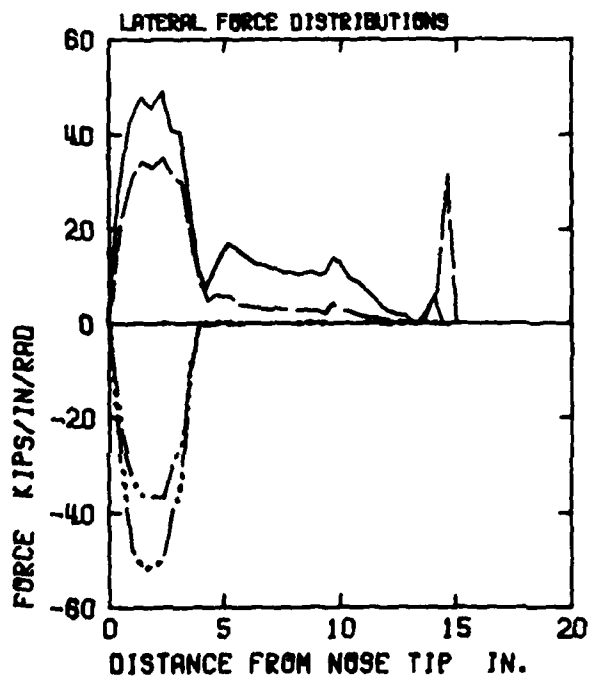
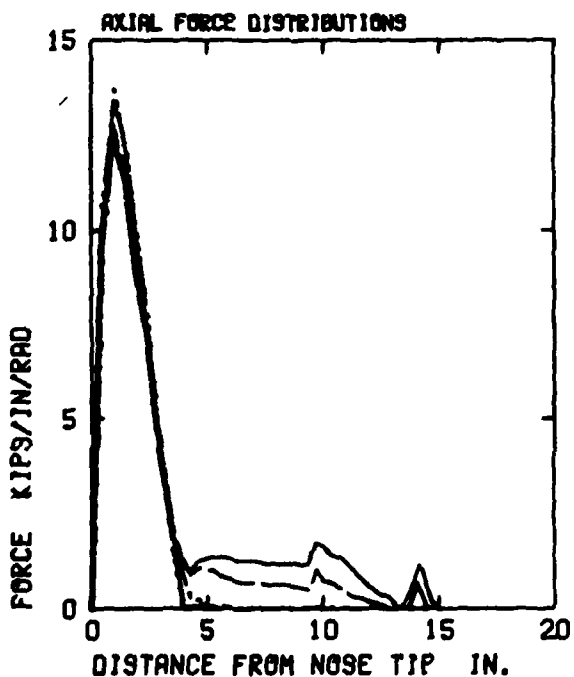
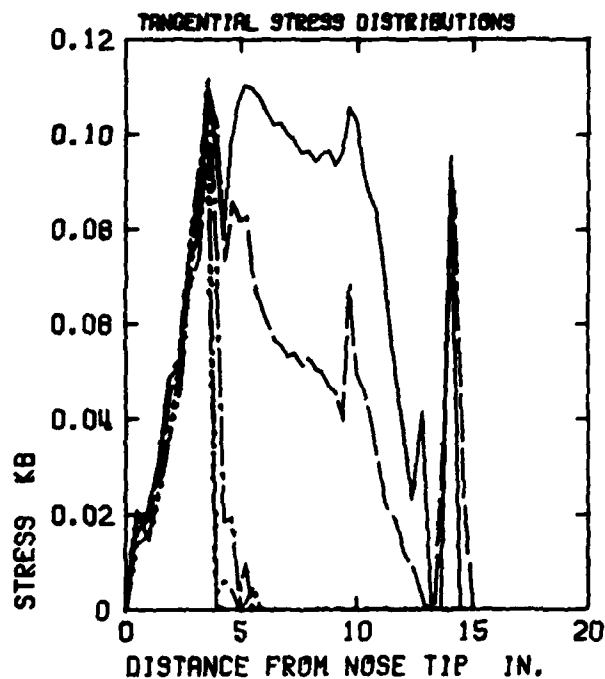
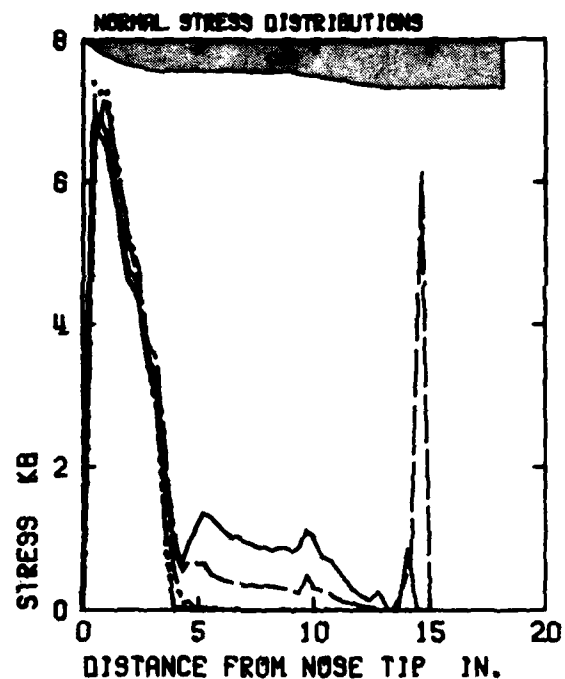


Figure 3.14. Stress and Force Distributions along Penetrator Contour at 800 μ sec.

(Acute)		(Obtuse)
— 0°-Plane	- - - 90°-Plane	— · — 180°-Plane
- - - 45°-Plane	- · - 145°-Plane	

The gross axial and lateral force distributions between the target and the penetrator are shown in Figures 3.15 and 3.16. As might be expected, the axial force is distributed primarily in the nose region. The lateral load profile is more variable, with a very large loading concentrated in the nose at $t = 200 \mu\text{sec}$, a gradual reduction in intensity and a general redistribution at $525 \mu\text{sec}$. A major increase in intensity develops at $800 \mu\text{sec}$ due to the involvement of the midsection and aft end of the penetrator and the target.

These force profiles are input into a detailed finite element model of the structure described in Section 4. As will be evident, the most critical portion of the input loads in terms of structural survivability are the axial loads and the early ($t < 200 \mu\text{sec}$) lateral loads applied to the forward end of the penetrator during nose burial. A parametric analysis of penetration dynamics during nose burial is presented in Section 5.

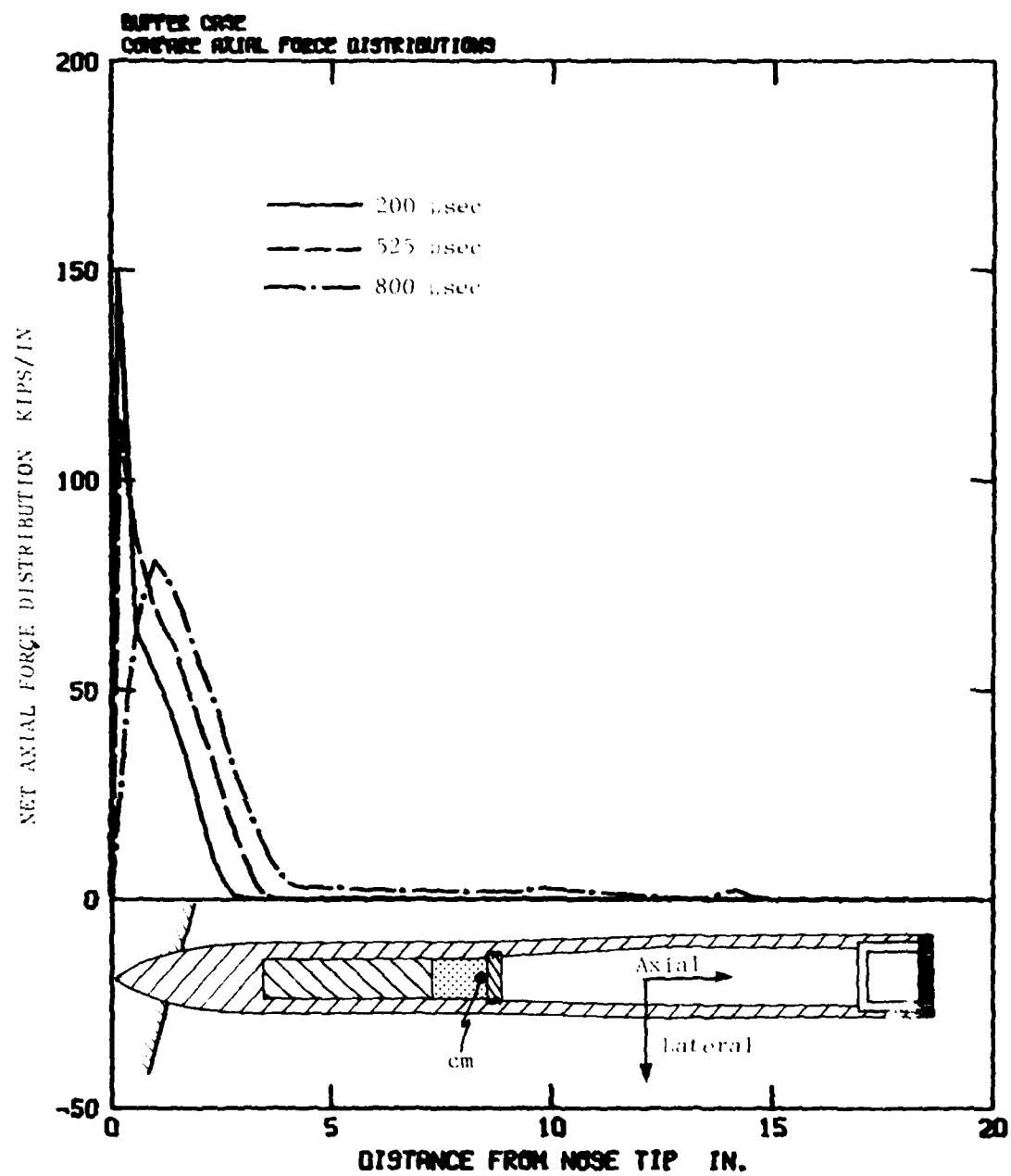


Figure 3-15. Net Axial Force Distribution Along Penetrator Contour.

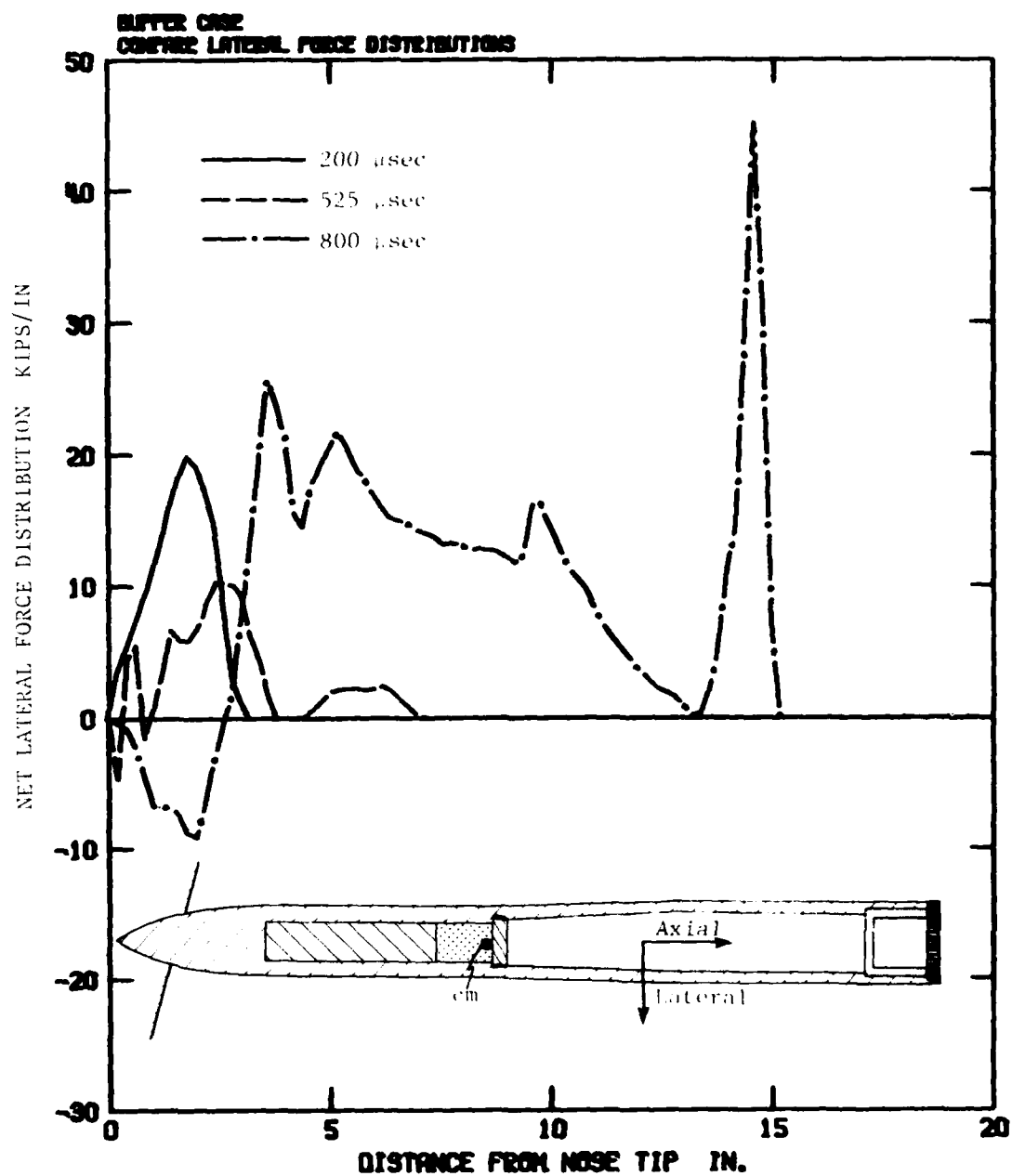


Figure 3.16. Net Lateral Force Distribution Along Penetrator Contour.

SECTION 4

STRUCTURAL RESPONSE AND COMPARISON WITH DATA

4.1 STRUCTURAL RESPONSE MODEL

As a result of the TRIFLE calculation, the forces applied to the penetrator by the target during impact are known, completing all the information required for an EPW response calculation. As the penetration environment produces very intense, impulsive loadings on the missile structure, dynamic elastic-plastic wave action may be expected to occur within the EPW. These intense waves will likely produce at least local plastic behavior and perhaps plastic behavior on a gross scale. To numerically simulate this complex behavior, a nonlinear finite element code, CRT/NONSAP, is used. This implicit time integration code is a modified version of the original NONSAP code developed at the University of California, Berkeley.^[13] The CRT/NONSAP code is capable of tracking nonlinear elastic-plastic dynamical structural response. The code has an extensive library of finite elements including two- and three-dimensional isoparametric continuum elements and a variety of one-dimensional elements. Several difference types of material models are available to represent nonlinear elastic and elastic-plastic material behavior.

As with most dynamical finite element codes, the primary advantages in the use of CRT/NONSAP are a) an ability to model complex structural configurations with complex stress states with relatively few higher order elements and b) an ability to use a large time step compared to explicit time integration codes. The primary disadvantages are a) the code is complete Lagrangian so that maximum distortion is more limited than for Eulerian or Lagrangian/Eulerian codes and b) material nonlinearity is more restricted than for explicit codes due to the implicit integration format.

For the penetration response problem the advantages inherent in the use of a nonlinear finite element code are very significant. The details of the penetrator can be accurately modeled and the calculations efficiently performed for arbitrary input forces. Since the finite elements used by the code are capable of representing highly variable strain fields, the code is capable of giving a fine resolution of the stress fields throughout the penetrator given only a relatively few finite elements.

The model used to describe the structure is shown in Figure 4.1, together with a schematic diagram of the actual structure and a very simple beam type model used in an early assessment of structural response. Based on the results obtained with the simple model, it was concluded that a much more complete and detailed model would have to be developed to capture the high frequency response observed in the RBT tests. The finite element model shown at the bottom of Figure 4.1 emerged as the model with the best combination of modeling accuracy and efficiency. Each element in the model is a plane stress finite element, but the out-of-plane thickness is taken as a variable to represent the exact amount of material that exists in that area of the structure. Also, in sections where more than one material exists (e.g., the center of section 2 where both the Kennertium ballast and the steel case are present) each material is modeled by a separate finite element. In this way the various materials are independently considered, each with its own elastic-plastic material characteristics, thus avoiding the difficulty of defining a composite elastic-plastic material representation. This "2½-D" modeling approach gives a simple but accurate structural model.

The force loading output from the TRIFLE code is in a format which specifies force per unit length along the surface of the penetrator. The forces/length are converted into

PENETRATOR STRUCTURAL PROPERTIES

SECTION NO.	$\frac{1}{\text{in}}$	$\frac{2}{\text{in}}$	$\frac{3}{\text{in}}$	$\frac{4}{\text{in}}$	$\frac{5}{\text{in}}$	$\frac{6}{\text{in}}$
AXIAL STIFF., in ²	1.236	2.844	1.585	1.418	1.512	1.280
BEND STIFF., in ²	0.1727	0.4432	0.3740	0.4185	0.5004	0.4401
SECT. MASS, $\frac{\text{lb-sec}^2}{\text{in.}}$	3.06×10^{-3}	9.45×10^{-3}	2.10×10^{-3}	4.12×10^{-3}	3.67×10^{-3}	2.20×10^{-3}

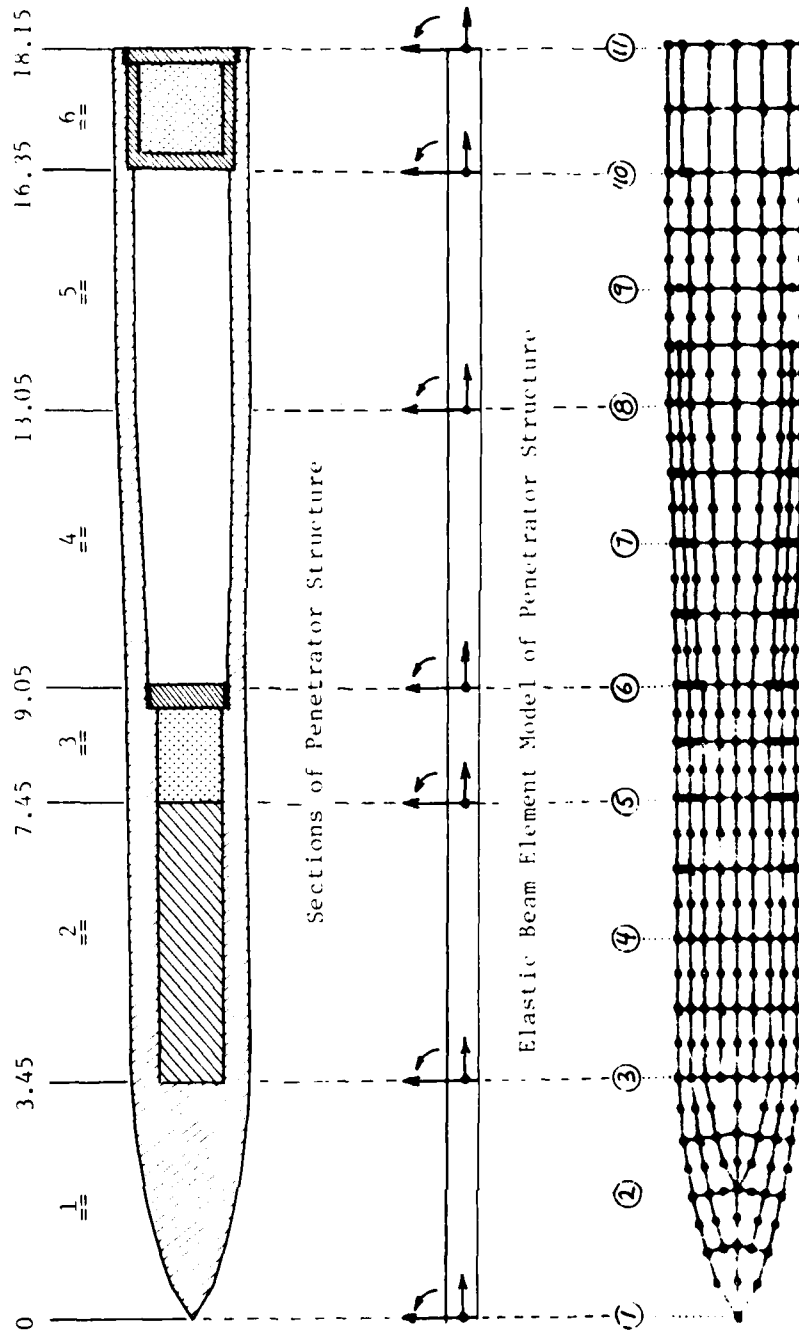


Figure 4.1. Modified Plane Stress (2D) Element Model of Penetrator Structure (including Applied Force Locations).

concentrated nodal forces along the top and bottom edge of the finite element model, with the axial forces equally distributed along the top and bottom edge and the lateral loads applied only to the top edge. The nodal forces are chosen so that each nodal force is statically equivalent to the line loading present in that region of the structure. Since the finite difference grid from the TRIFLE code and the finite element grid used by CRT/NONSAP are different, special care must be used in converting TRIFLE forces information to CRT/NONSAP nodal forces.

The CRT/NONSAP code prints displacement, velocity, acceleration, strain and stress levels at specified stations throughout the structure so that comparisons can be made between any experimental results from accelerometers and/or strain gauges and associated CRT/NONSAP results. The code has a complete plotting software package capable of displaying the various types of information regarding structural response, including plots of deformed geometry.

4.2 RESPONSE ANALYSIS AND COMPARISONS

The TRIFLE force distributions, when converted to CRT/NONSAP forces described in Section 4.1, result in axial nodal forces shown in Figures 4.2 and 4.3, each applied at the indicated station, half on the top node and half on the bottom node. Note that the major portion of the axial forces are applied at stations 1 and 2 for times $0 < t < 600 \mu\text{sec}$. For $t > 600 \mu\text{sec}$, the aft end of the structure becomes involved with the target and nodal forces at stations 6, 7 and 8 rise sharply while forces at 1 and 2 diminish or level off. The intensity of axial forces at 6, 7 and 8 is primarily due to the aft body flare and the "tail-slap" phenomenon in which the upstream side of the EPW engages the target.

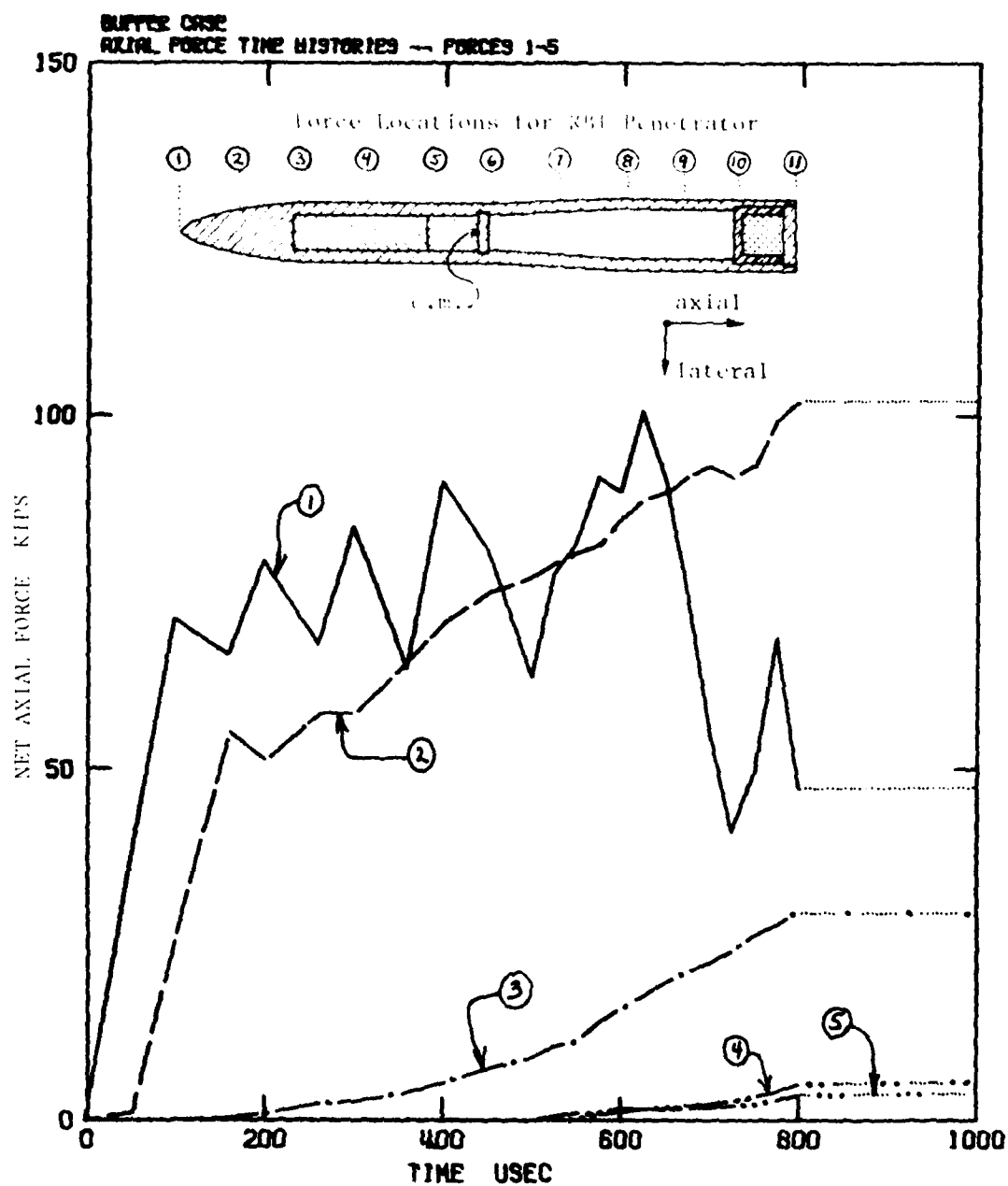


Figure 4.2. Net Axial Force Time Histories for Penetrator Stations Forward of Center of Mass.

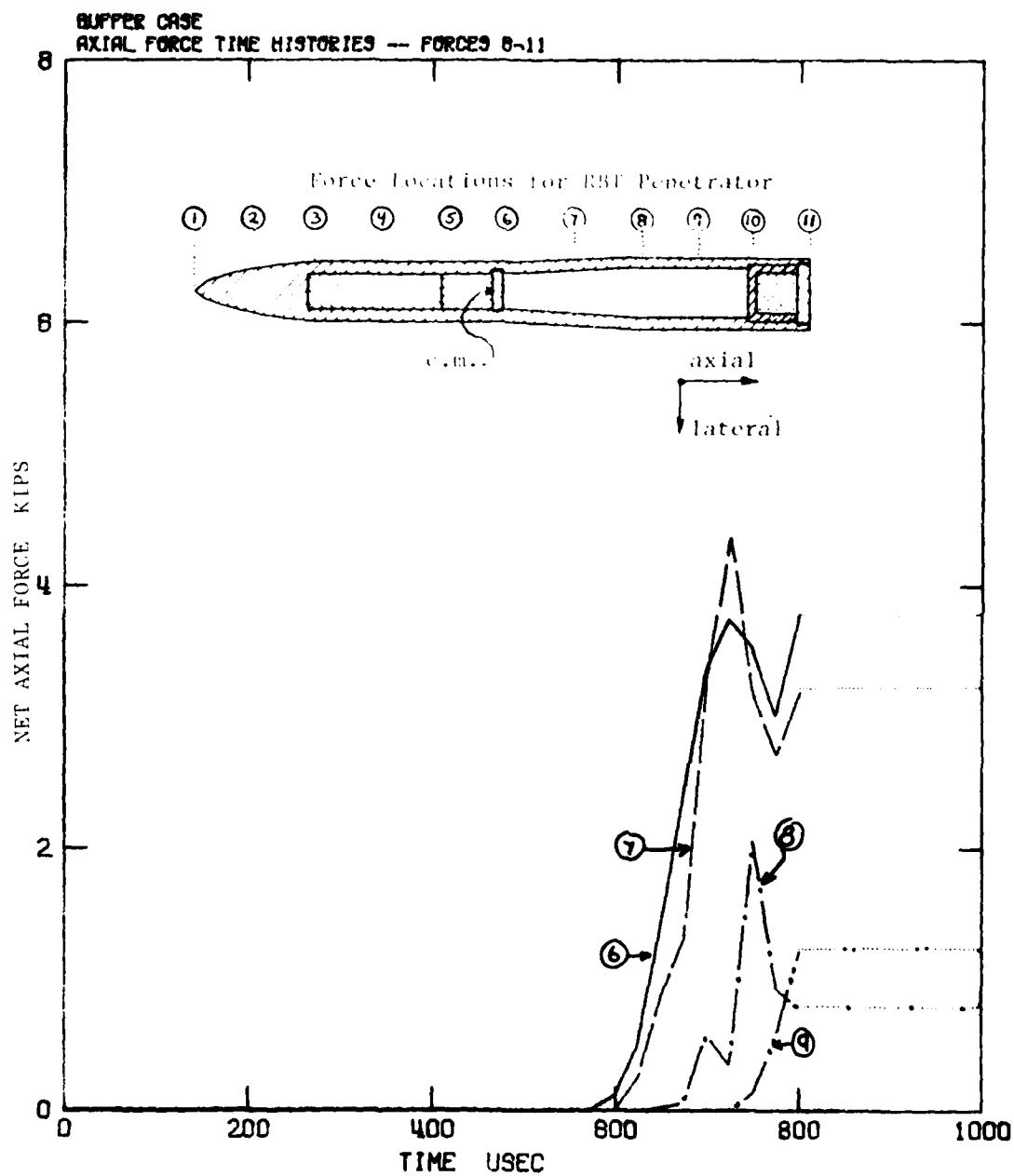


Figure 4.3. Net Axial Force Time Histories for Penetrator Stations Aft of Center of Mass.

The lateral nodal forces are shown in Figures 4.4 and 4.5 for stations in the forward and aft ends of the structure, respectively. Note that the forces are all positive except forces 1 and 2 for times after 800 μ sec. Also, note the intense lateral forces generated in the forward most section (stations 1 and 2) for $0 < t < 200 \mu$ sec. These forces correspond to the resultant of forces on the upstream and downstream faces of the entering missile, before appreciable lateral displacements and rotation are developed sufficient to reduce the influence of the 3° yawed impact. These lateral forces will be shown to have a very important effect on structural response since they are located at the forward tip of the long, slender $L/D = 10.6$ structure. Finally, note the buildup of very intense nodal forces on the aft end of the structure for late times, $t < 600 \mu$ sec, when the aft end of the EPW engages the target on its upstream side (the "tail-slap" phenomenon).

These nodal forces are used by the CRT/NONSAP computer code to calculate the dynamic elastic-plastic response of the EPW. The numerical results obtained from the code may then be compared with experimental results obtained from the 0.284-scale reverse ballistic test (RBT). In the tests the penetrator was fitted with two types of instruments:

- a) axial and lateral accelerometers near the center of mass of the missile and in the aft end of the structure.
- b) strain gauges applied on the inner and outer surfaces of the EPW in the mid and aft sections.

Figures 4.6 and 4.7 indicate both the results of DNA test #2^[8] and the CRT/NONSAP calculation of center of mass accelerations in the lateral and axial directions, respectively. As is evident, the general profile of the axial accelerations in Figure 4.7 agree

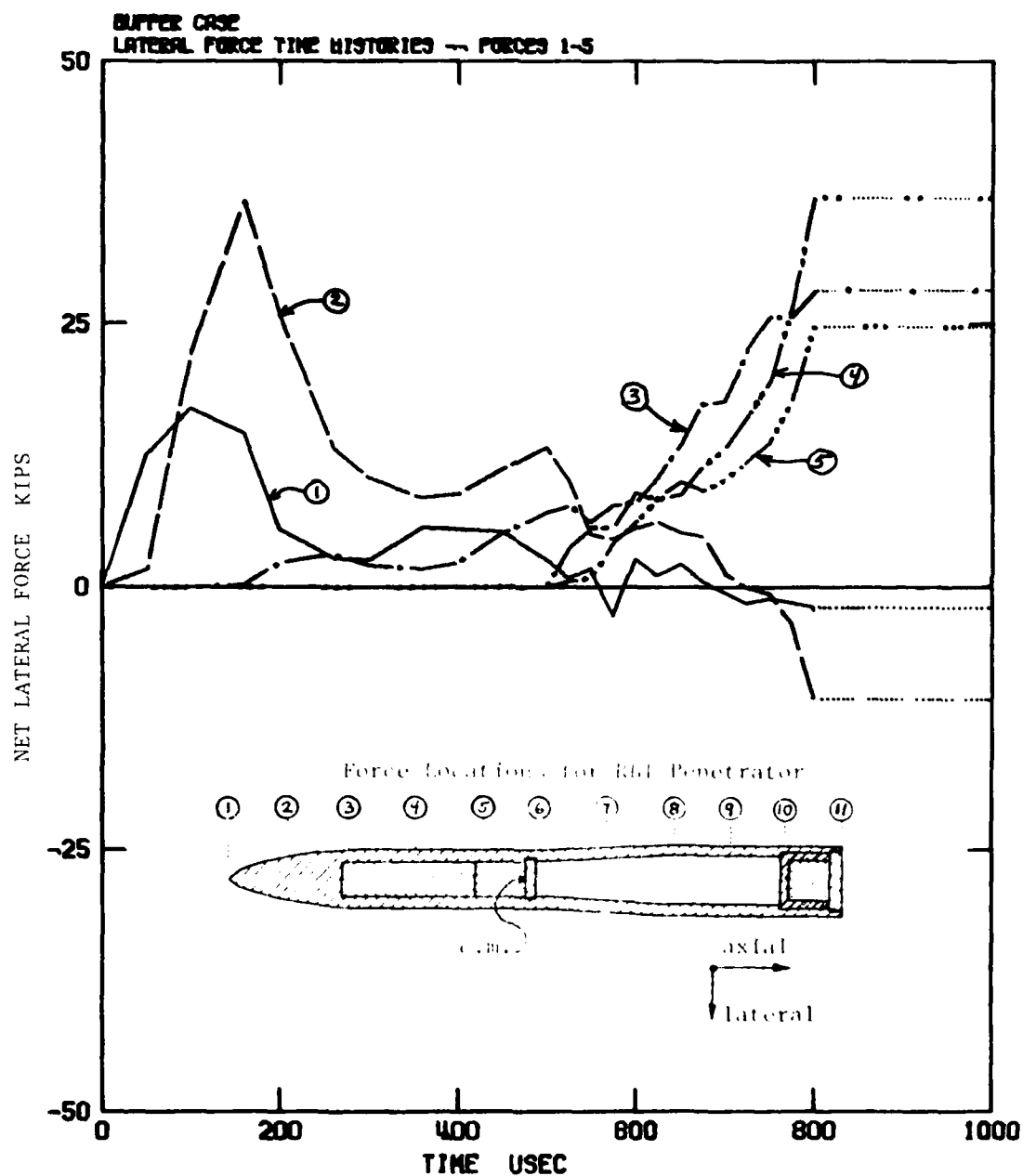


Figure 4.4. Net Lateral Force Time Histories for Penetrator Stations Forward of Center of Mass.

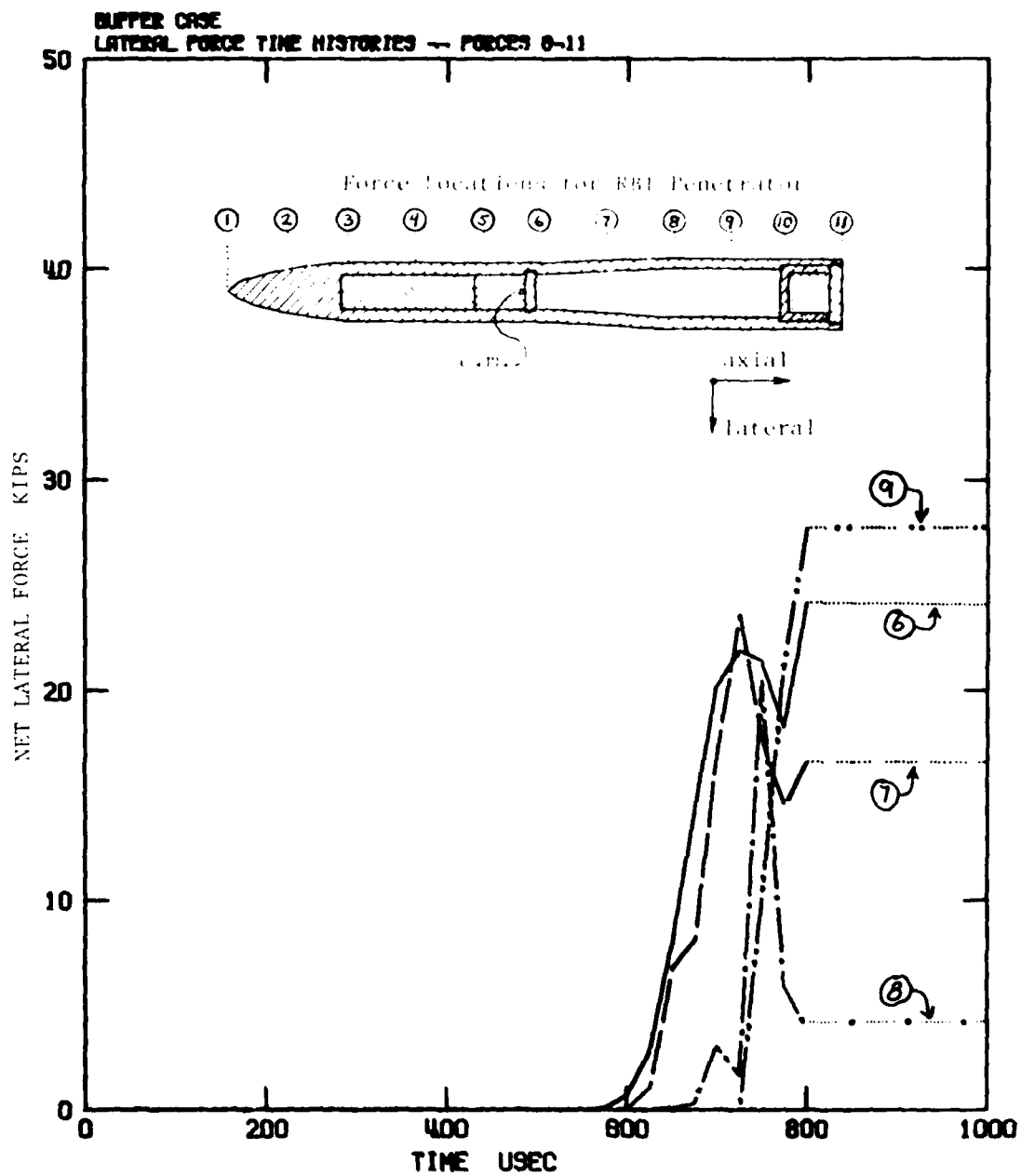


Figure 4.5. Net Lateral Force Time Histories for Penetrator Stations Aft of Center of Mass.

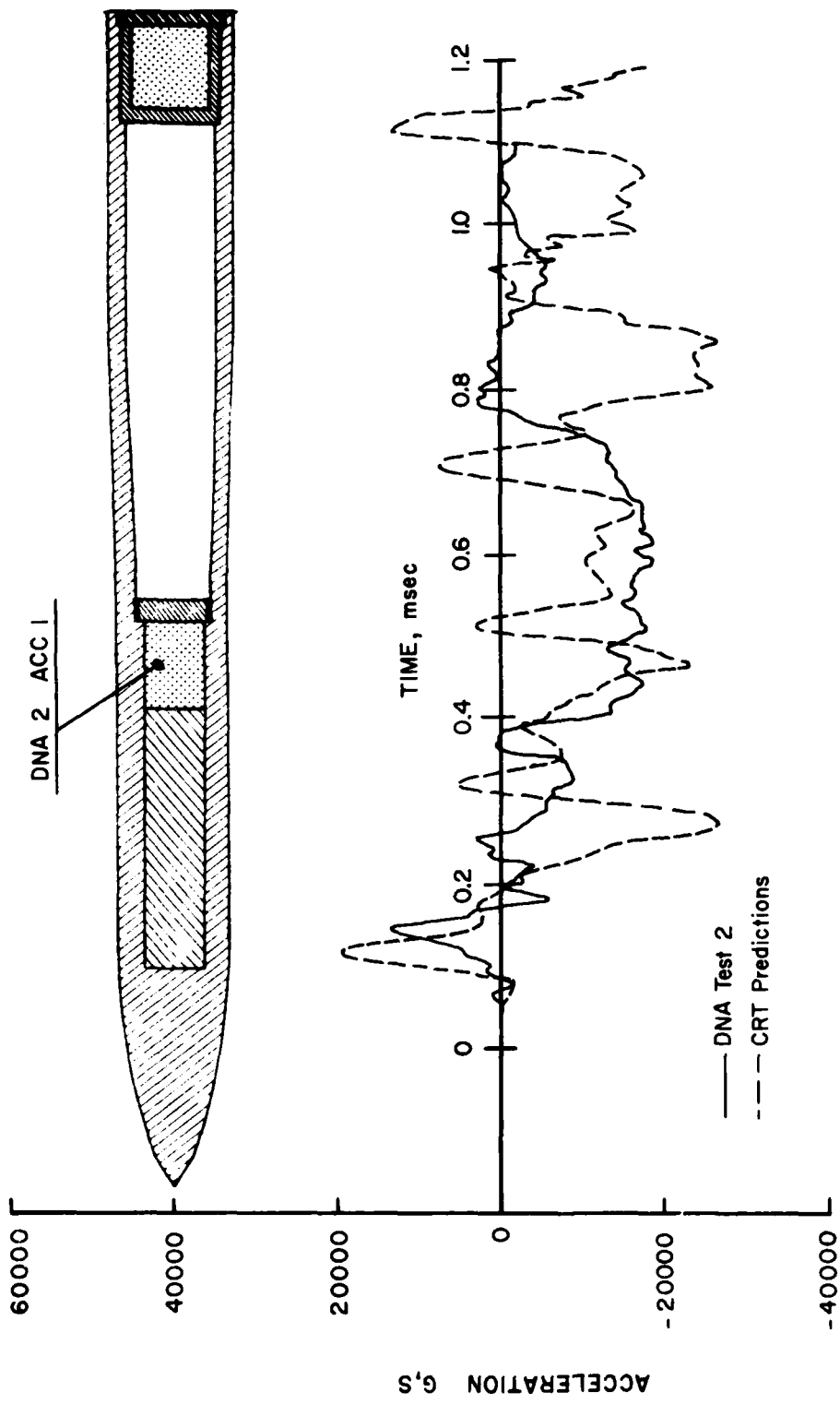


Figure 4.6. Experimental and Analytical Results for Lateral Acceleration Near the Center of Mass.

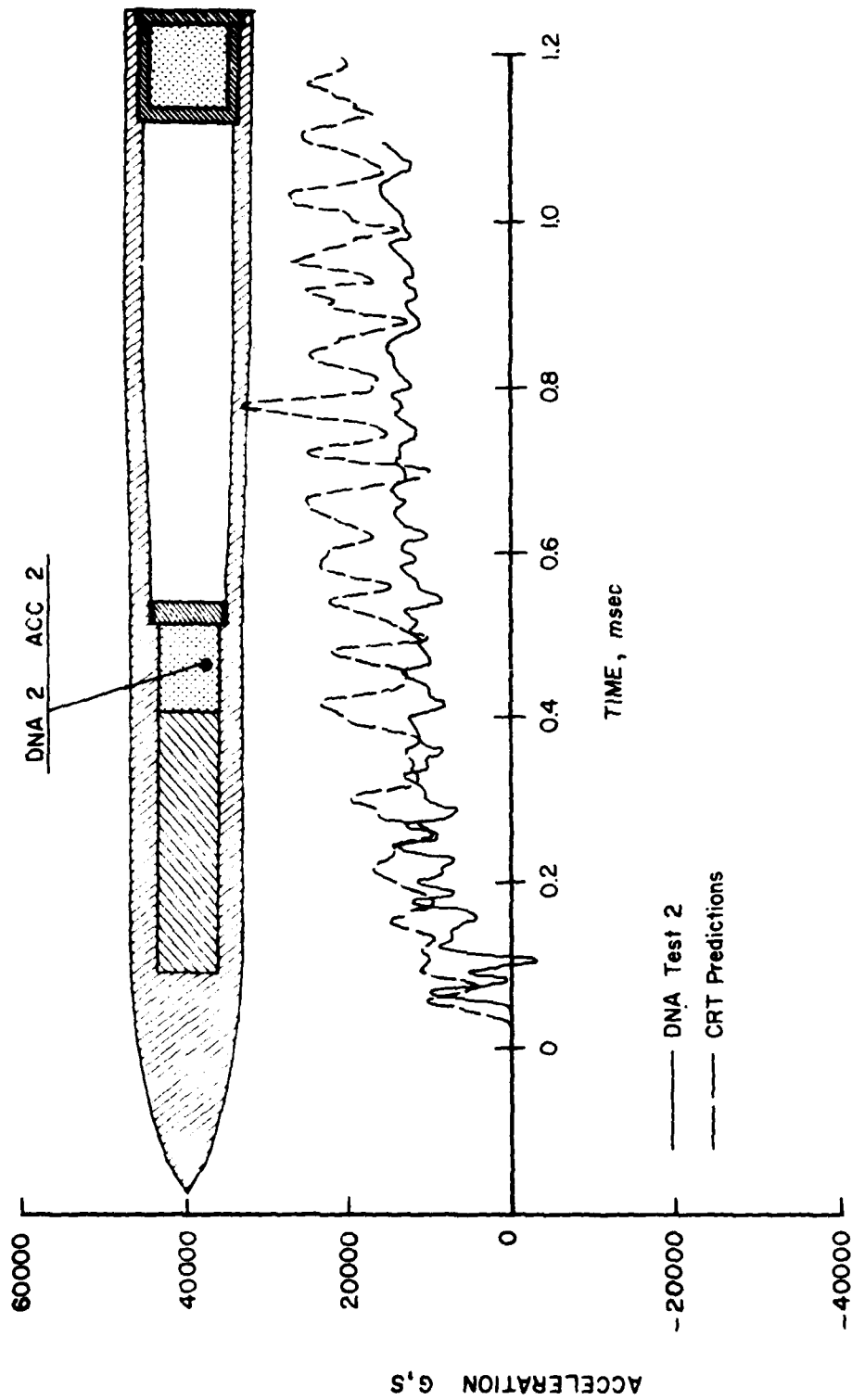


Figure 4.7. Experimental and Analytical Results for Axial Acceleration Near the Center of Mass.

reasonably well with experimental results, except that the numerical results appear to be approximately 30-40% too high on the average and also carry much more high frequency oscillation than the experimental results. The overestimate of the average axial deceleration is probably due to an overestimate of the strength properties of actual sandstone used in the test. The difference in intensity between the high frequency ringing results is thought to be due to the deterioration of the potting material used to suspend the accelerometers. The experimental results show large scale ringing only for $t < 175 \mu\text{sec}$, i.e., for the first major reversal in the acceleration, after which the oscillation appears to be more highly damped. This feature is more evident in the lateral acceleration, Figure 4.6. Here, the experimental and analytical results are in reasonable agreement, again for $t < 175 \mu\text{sec}$, i.e., for the first major excursion and reversal. After this time the accelerometers reveal very little ringing, while the computer program indicates a heavy ringing phenomenon associated with stress wave propagation. The experimental results indicating the lack of ringing are difficult to justify, especially for times $t < 400 \mu\text{sec}$ during which the EPW is almost entirely elastic, according to both experimental and analytical calculations for strains.

The experimental and analytical results for aft end accelerations in the lateral and axial directions are shown in Figures 4.8 and 4.9, respectively. Again, the axial accelerations appear to agree reasonably well except for the lack of a major ringing signal in the experimental data. Also, a major "ding" occurs in the experimental record at $400 \mu\text{sec}$, after which the analytical and experimental results appear to diverge, with the analytical acceleration maintaining a level 20,000 g (equal to the center-of-mass axial acceleration) while the experimental results fall

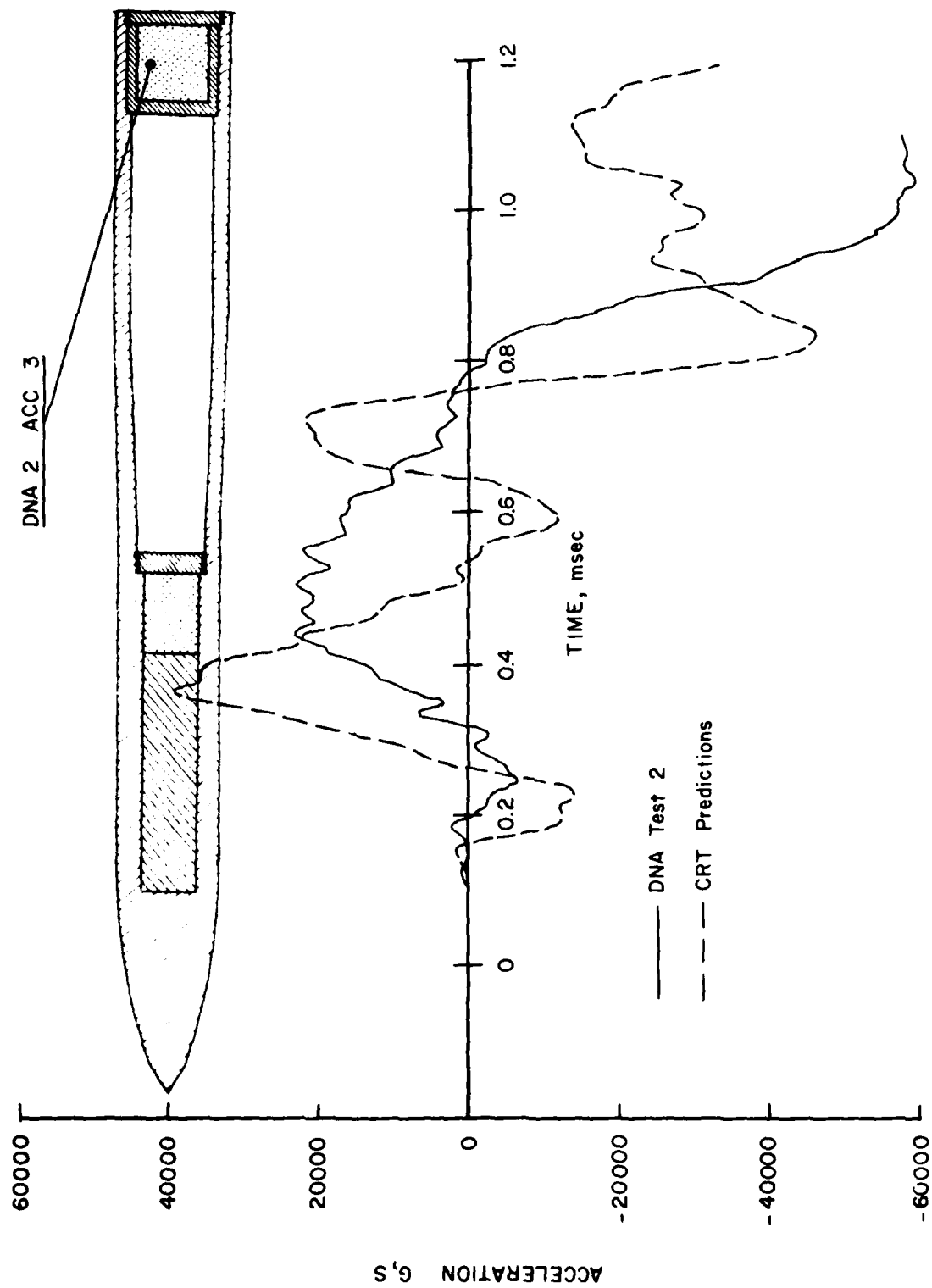


Figure 4.9. Experimental and Analytical Results for Lateral Acceleration at ATT End.

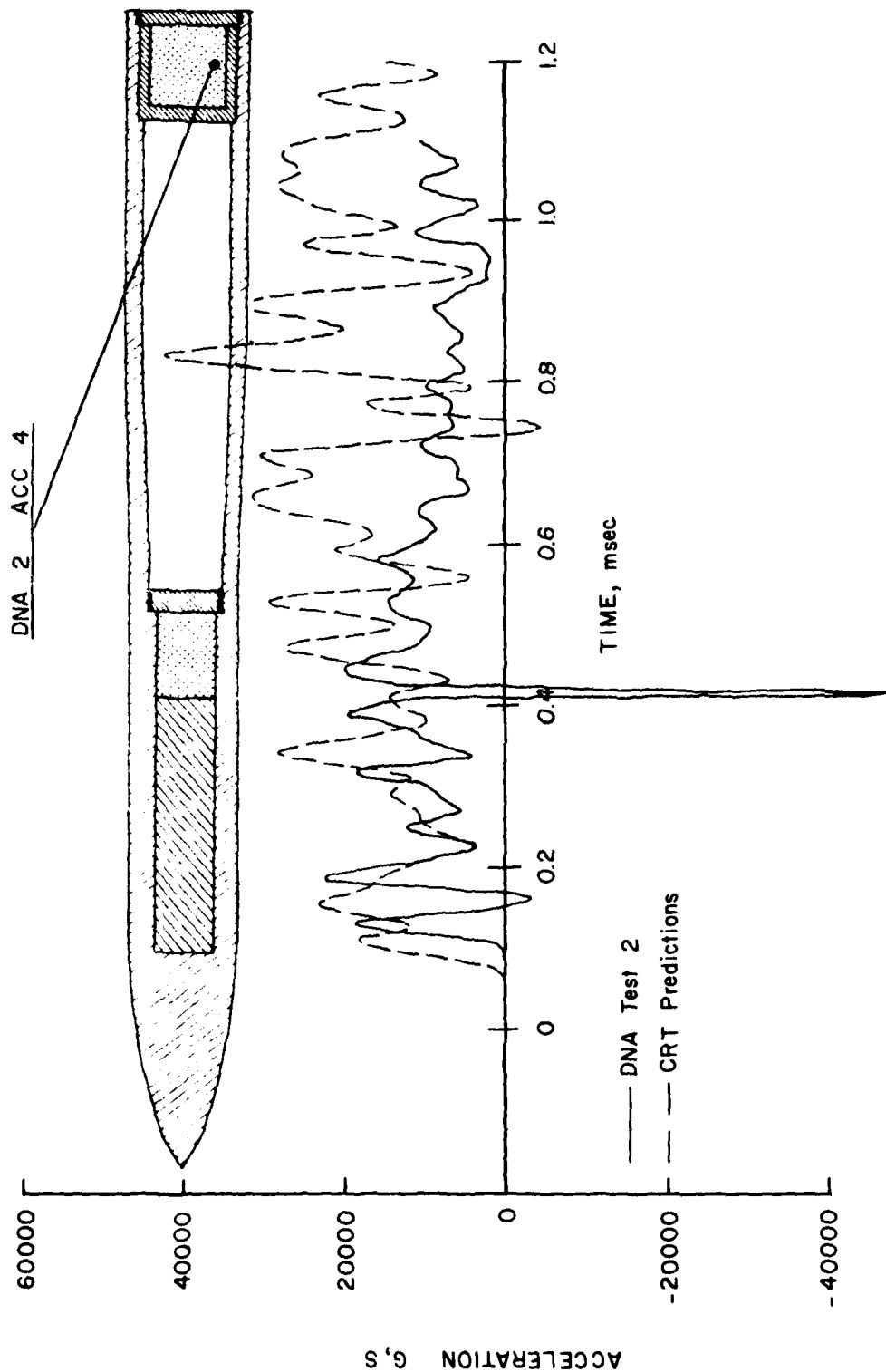


Figure 4.9. Experimental and Analytical Results for Axial Acceleration at ART End.

off to ~7,000 g in contrast to the center-of-mass axial results which are maintained at a level of ~14,000 g throughout the test. The lateral acceleration of the aft end, Figure 4.8, shows only a gross agreement between experimental and analytical results, with the experimental results serving as a sort of average of the analytical accelerations, with the major excursions eliminated.

A second point which tends to support the analytical results is the fact that damage to acceleration sensitive equipment located in the aft end of the missile is known to occur, thus supporting the position that the acceleration environment is more severe than tests indicate.

Comparison of analytical and test results for strain gauge data is in general much better than for the acceleration data, in part due to the fact that strains are based on displacements rather than accelerations, i.e., on second integrals in time of acceleration data and also on the greater tolerance of strain gauges to impact forces. The experimental and analytical results for strains in the midsections are shown in Figures 4.10 through 4.13.

Figure 4.10 indicates axial strain on the outer face of the top surface; Figure 4.11 indicates axial strain on the inner face of the top surface; Figure 4.12 indicates axial strain on the inner face of the bottom surface; and Figure 4.13 indicates axial strain on the outer face of the bottom surface. Both experimental and test results are in substantial agreement, although it is evident that strain gauge 3 (Figure 4.10) and strain gauge 9 (Figure 4.12) are damaged during the test. Both results indicate that the EPW is undergoing very large bending type deformation in its midsection, with tensile strain on the top surface and even larger compressive strain on the bottom surface. The lack of symmetry is due to the axial compression

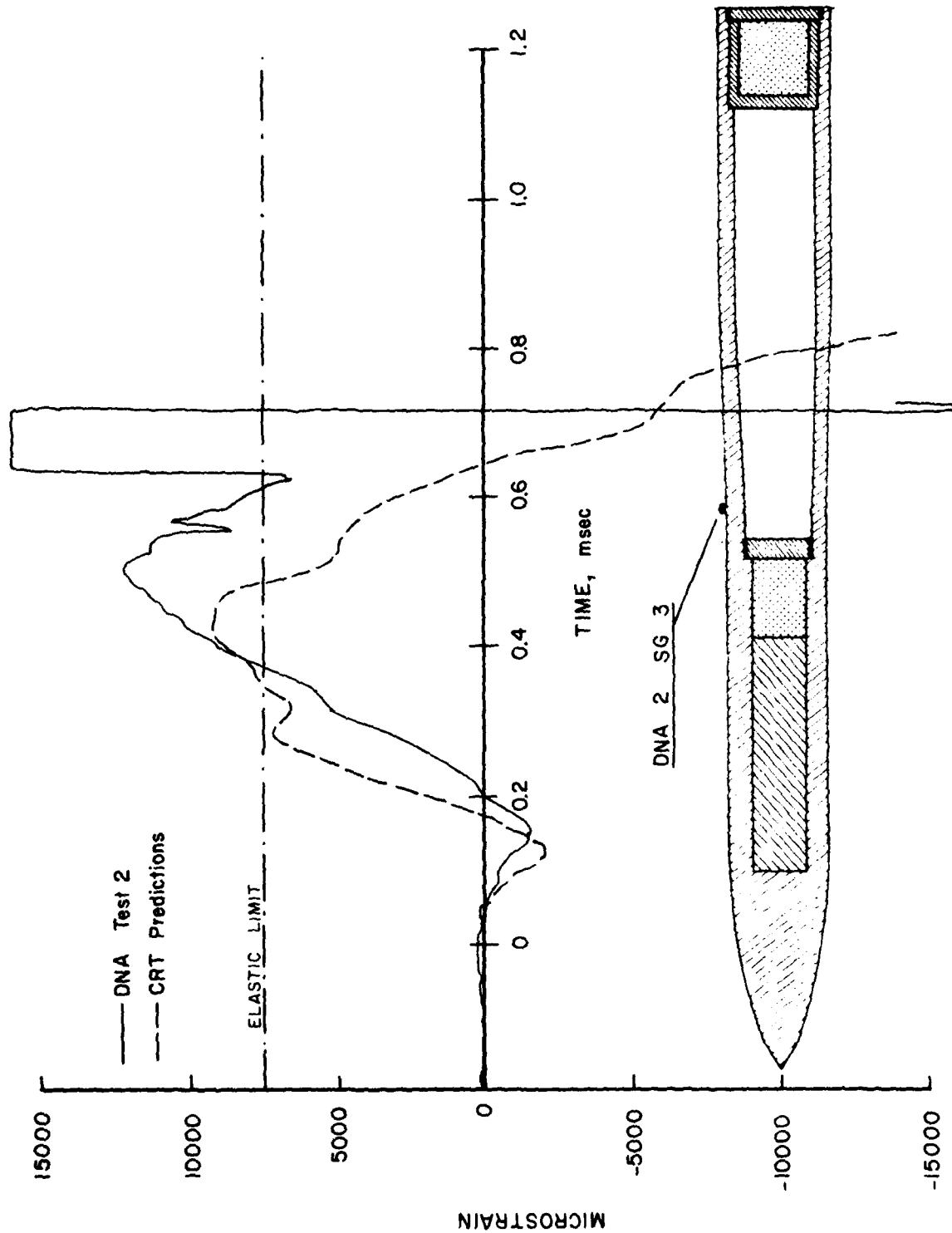


Figure 6.10. Experimental and analytical axial strains on outer face of top surface of PW rib section.

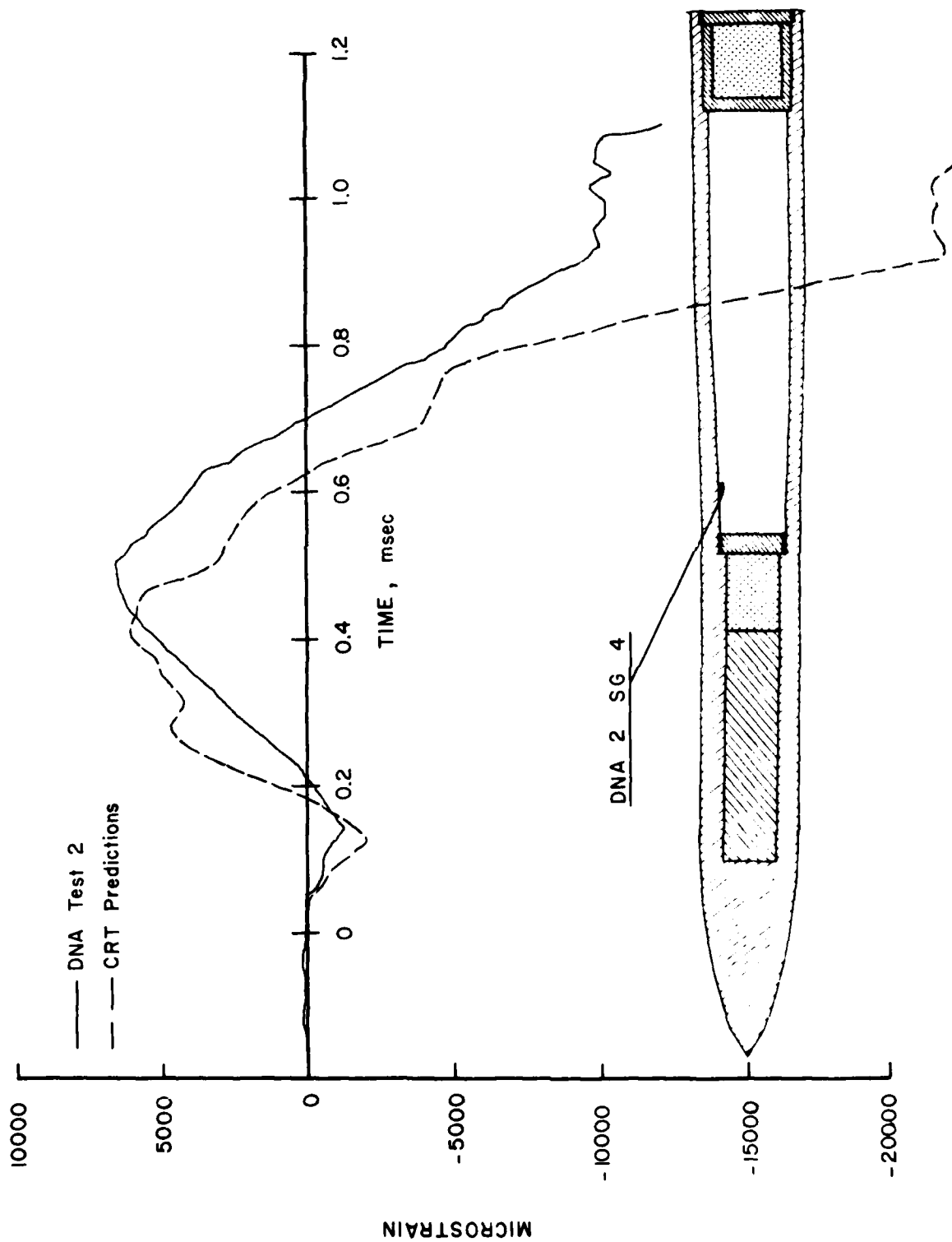


Figure 6.11. Experimental and Analytical Axial Strains on Inner Face of Top Surface of CPZ Thrust Section.

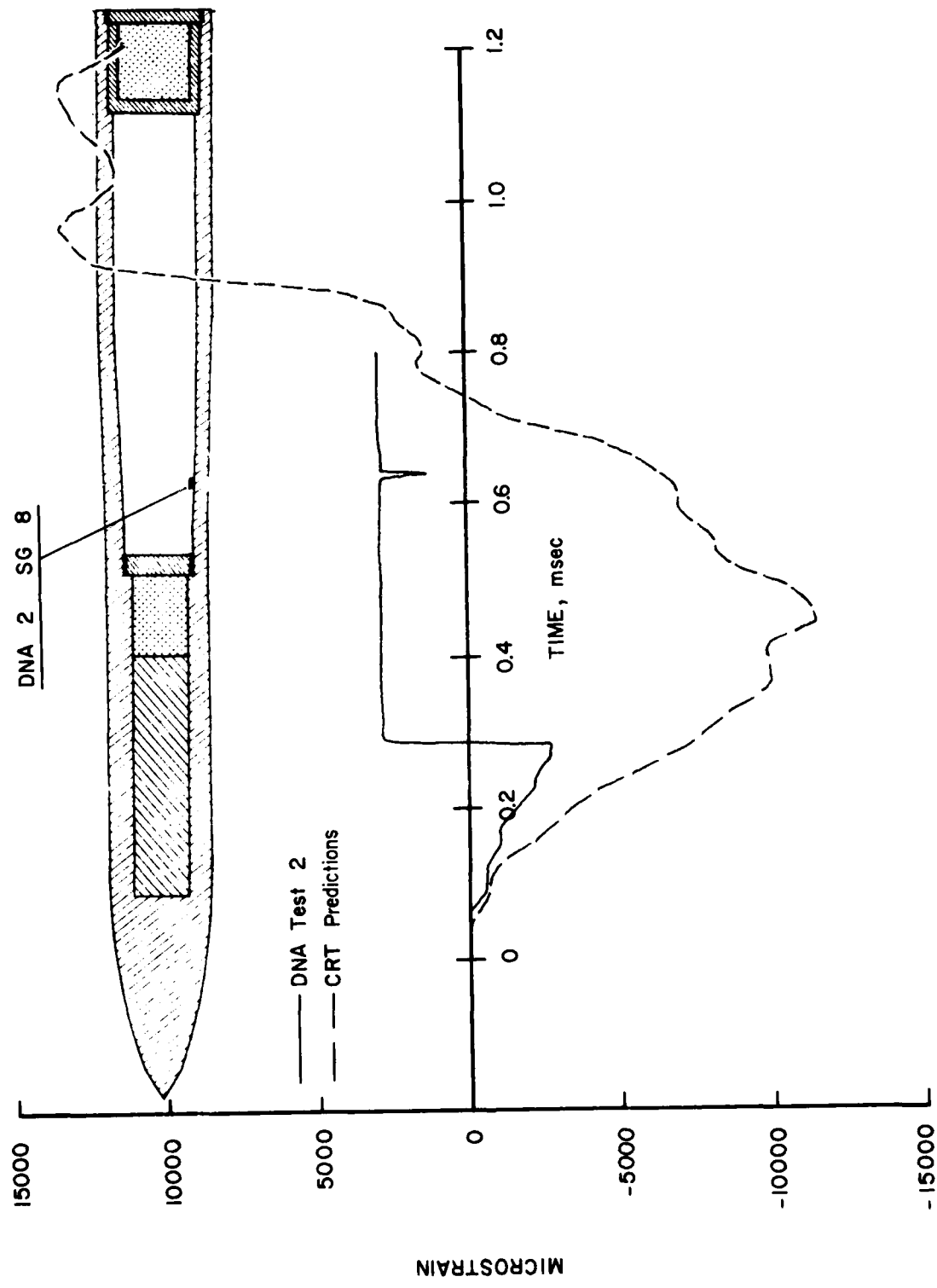


Figure 4.12. Experimental and Analytical Axial Strains on Inner Face of Bottom Surface of EPW Addition.

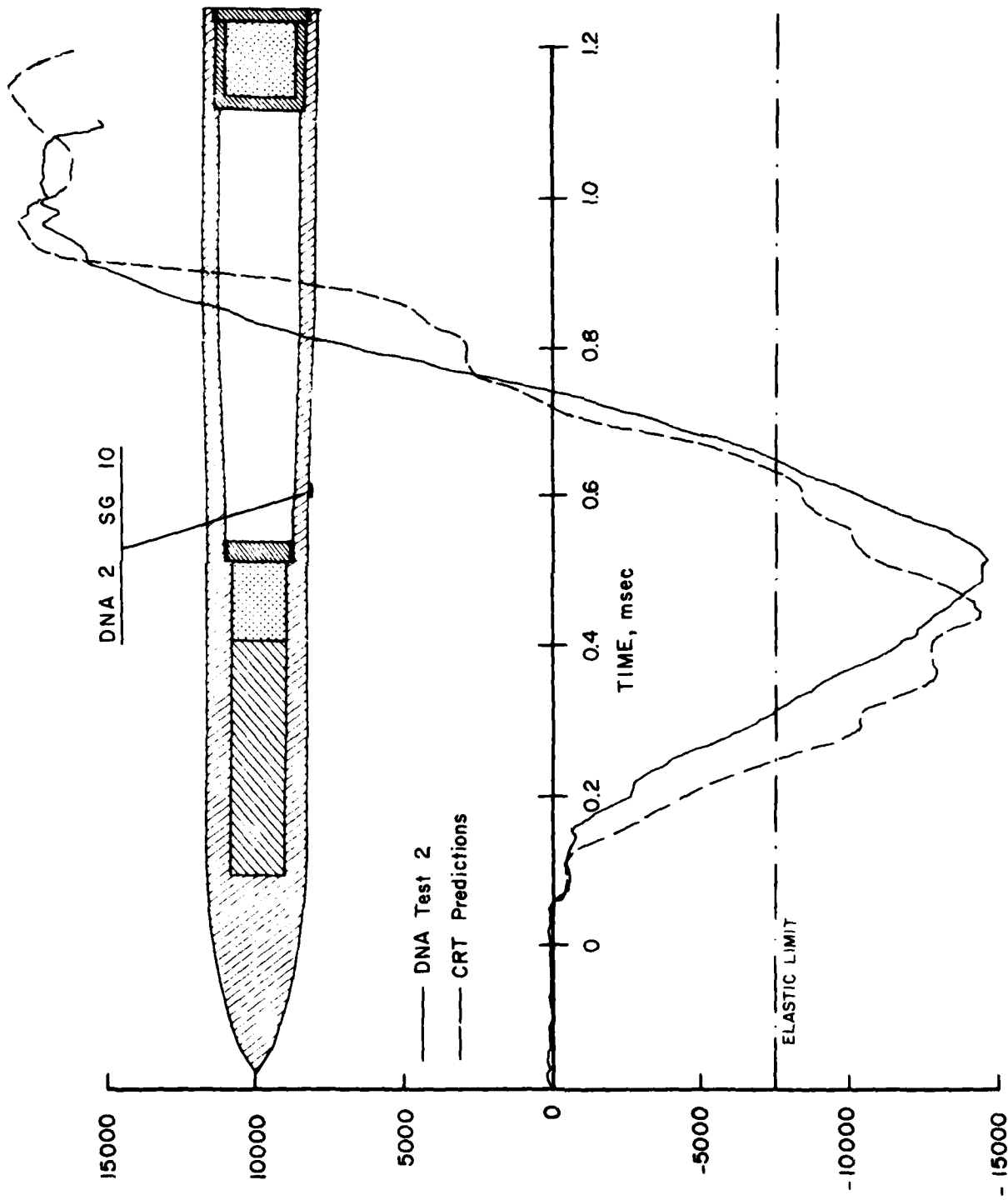


Figure 4.13. Experimental and analytical axial strains on outer face of bottom surface of p.d. midsection.

acting simultaneously with the bending deformation, with the compressive strain subtracting from the positive tensile bending strain on the top surface but adding to the compressive bending strain on the bottom surface. Clearly the bending action is dominant since the absolute values of the maximum top surface strain (analytical result $\sim 12,000 \mu\text{in/in}$ at $t \sim 500 \mu\text{sec}$) and bottom surface strain (analytical result $\sim 14,500 \mu\text{in/in}$ at $t \sim 500 \mu\text{sec}$) differ by only $2500 \mu\text{in/in}$, twice the axial component resulting from the axial deceleration. Thus, while the axial forces might be anticipated as the major contributor to structural deformation, actually the lateral forces in the forward end of the penetrator are the sources of the very high (bending) deformations, with the highest values being just aft of the threaded cap used to seal the midsection accelerometer package.

The experimental and analytical results for strains in the aft end of the structure are shown in Figures 4.14 and 4.15 for the outer surfaces on the top and bottom of the missile. These results are much less dramatic than for the midsection due to the lack of bending deformations. The results agree qualitatively, although there appears to be a delay in the experimental results as compared to the analytical. This is in part due to the model of the penetrator, Figure 4.1, in which the aft end of the structure was modeled with fewer elements than forward and middle portions of the missile. Consequently, the stiffness was slightly high although the mass was modeled correctly. This gives an elastic wave speed in the aft end of the analytical model that is somewhat higher than in the test structure.

Overall, the strain gauge results show remarkably good agreement with the analytical results. Both show the penetrator to be responding in an elastic manner, except for plasticity in the forward-most end and in the midsection. Of course, even

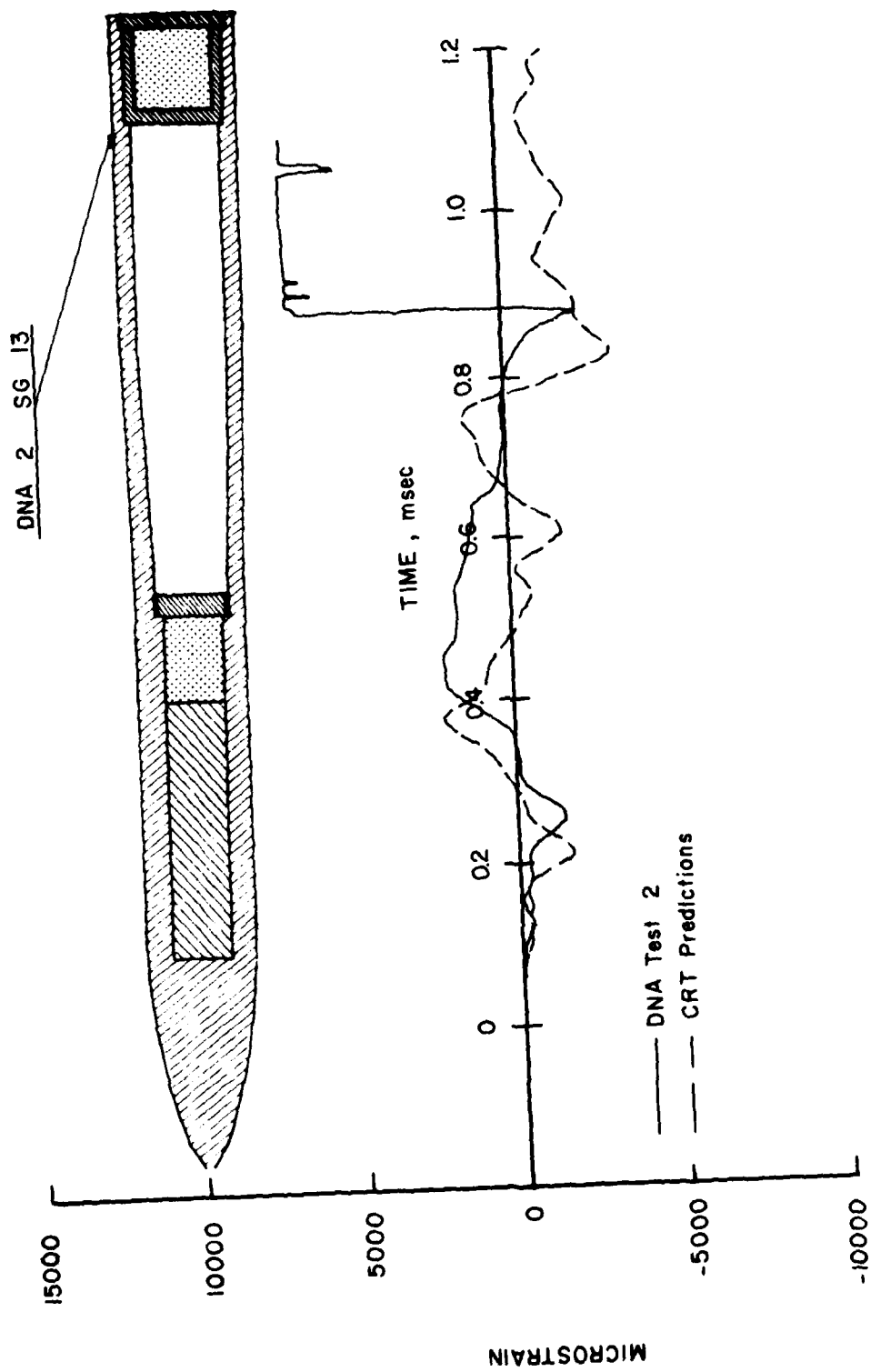


Figure 4.14. Experimental and analytical results for axial strain on outer leg
Surface of Act 100.

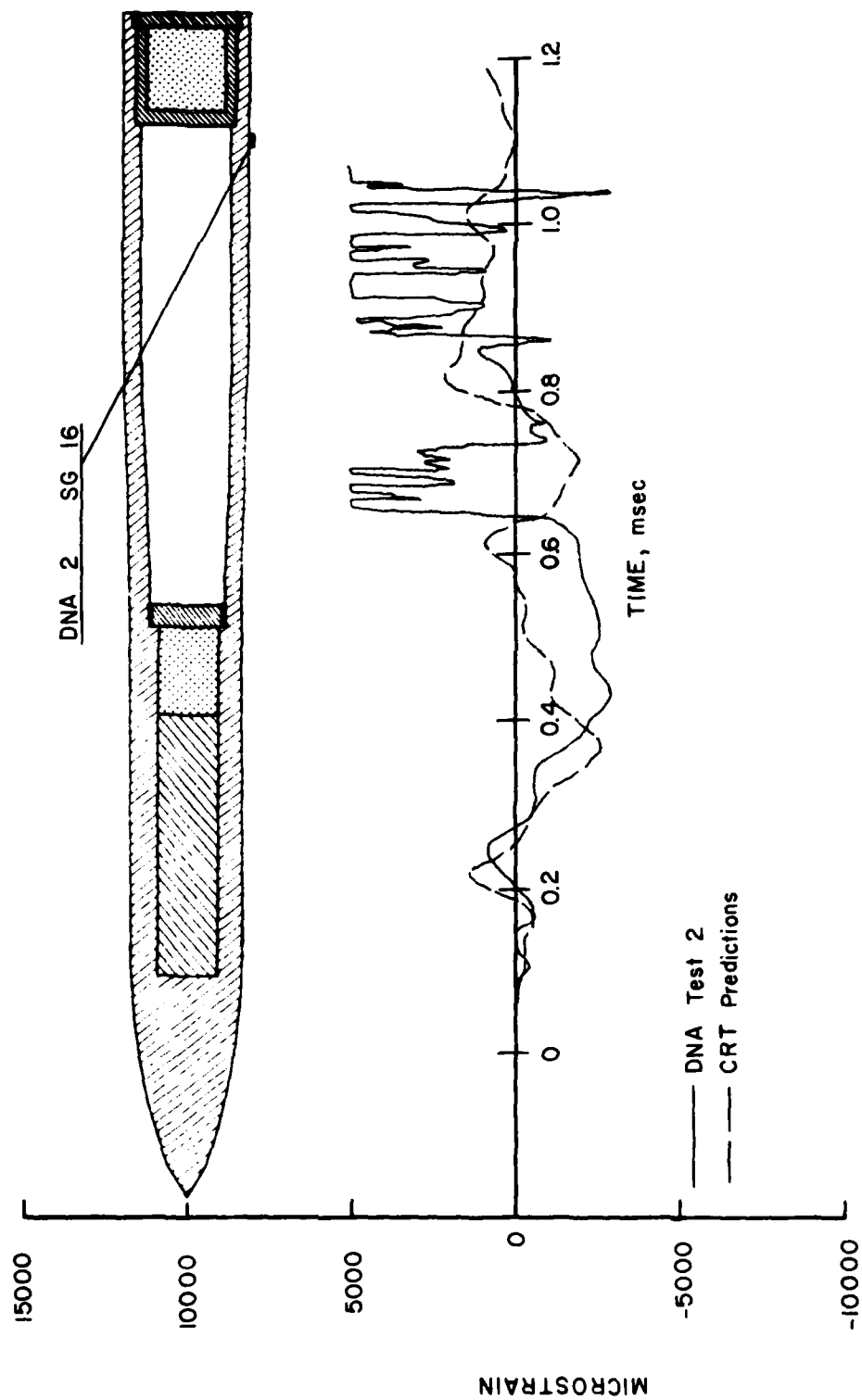


Figure 4.15. Experimental and Analytical Results for Axial Strain on outer Bottom Surface of Aft End.

mild plasticity can result in major structural damage, especially in the threaded area and in the machined area in the center portion of the structure. Here, local stress concentrations can increase the material sensitivity to high stress levels and produce elastic or elastic-plastic fracture. The significance of this problem is highlighted by the residual bending deformations and structural failure observed in the 0.284-scale test series.^[8,9]

Since the CRT/NONSAP calculation relies completely on the forces determined by the TRIFLE code, the accuracy of the numerical results can only be achieved if the input forces from TRIFLE accurately represent the penetration physics.

The agreement between the experimental and analytical results appear, therefore, to verify adequately the TRIFLE code and the combined TRIFLE/NONSAP analysis. These computational procedures are believed to provide a practical and accurate computational method for analyzing non-normal EPW penetration problems.

SECTION 5

PARAMETRIC ANALYSIS OF PENETRATION DYNAMICS

The development of the TRIFLE code as a reliable method for investigating EPW penetration permits the code to be used as a tool for evaluating the changes in system behavior resulting from changes in the various input parameters which define the problem. In particular, the parameters of interest are flight attitude, impact velocity, L/D ratio, nose configuration, target definition and details of the missile structure. To demonstrate the capability of the TRIFLE code in measuring the post-impact performance of an EPW, eight separate analyses were performed as detailed in Table 5.1. In all cases the target material was Dakota sandstone and the penetrator was assumed to be rigid. In all but Case 8, the penetrator was assumed to have the same L/D ratio as the 0.284-scale penetrator and to have the same mass distribution. In the remaining seven cases the design of the nose, the impact velocity, obliquity and angle of attack (yaw) were all varied and the penetration was carried to a full nose burial. For Case 8, the penetrator L/D ratio was reduced 50%, along with appropriate changes in location of mass centroid and radius of gyration.

In the following, all comparisons are based on rigid body axial, lateral and angular accelerations, shown in Figure 5.1, 5.2 and 5.3, respectively. Clearly, as far as axial acceleration is concerned, Figure 5.1, only CRH = 3 has a major influence for a given velocity of impact; obliquity and yaw have little effect. Increasing impact velocity by 31.5% (1521 fps to 2000 fps) increases the maximum axial deceleration by approximately 33%, i.e., in a proportional manner. The effects of parameter variations are much greater with regard to lateral and angular accelerations. As may be seen from Figures 5.2 and 5.3, the case of normal ($\alpha=0^\circ$)

Table 5.1. Parametric Study of Asymmetric Penetration

Case	Target Material	Tangent Ogive Penetrator (W/A=4.2 psi)	Impact Velocity	Obliquity α	Angle of Attack β
1	Sandstone	CRH=6, L/D=10.6	1521 fps	0°	0°
2	"	"	"	"	3°
3	"	"	"	"	5°
4	"	"	"	20°	0°
5	"	"	"	20°	3°
6	"	"	2000 fps	0°	"
7	"	CRH=3, L/D=10.6	1521 fps	"	"
8	"	CRH=6, L/D=5.3*	"	"	"

* Center of mass and radius of gyration reduced by half. W/A held constant.

Case	CRH	L/D	V_i (fps)	α	β	Case	CRH	L/D	V_i (fps)	α	β
1	6.0	10.6	1521	0°	0°	5	6.0	10.6	1521	20°	3°
2	6.0	10.6	1521	0°	3°	6	6.0	10.6	2000	0°	3°
3	6.0	10.6	1521	0°	5°	7	3.0	10.6	1521	0°	3°
4	6.0	10.6	1521	20°	0°	8	6.0	5.3	1521	0°	3°

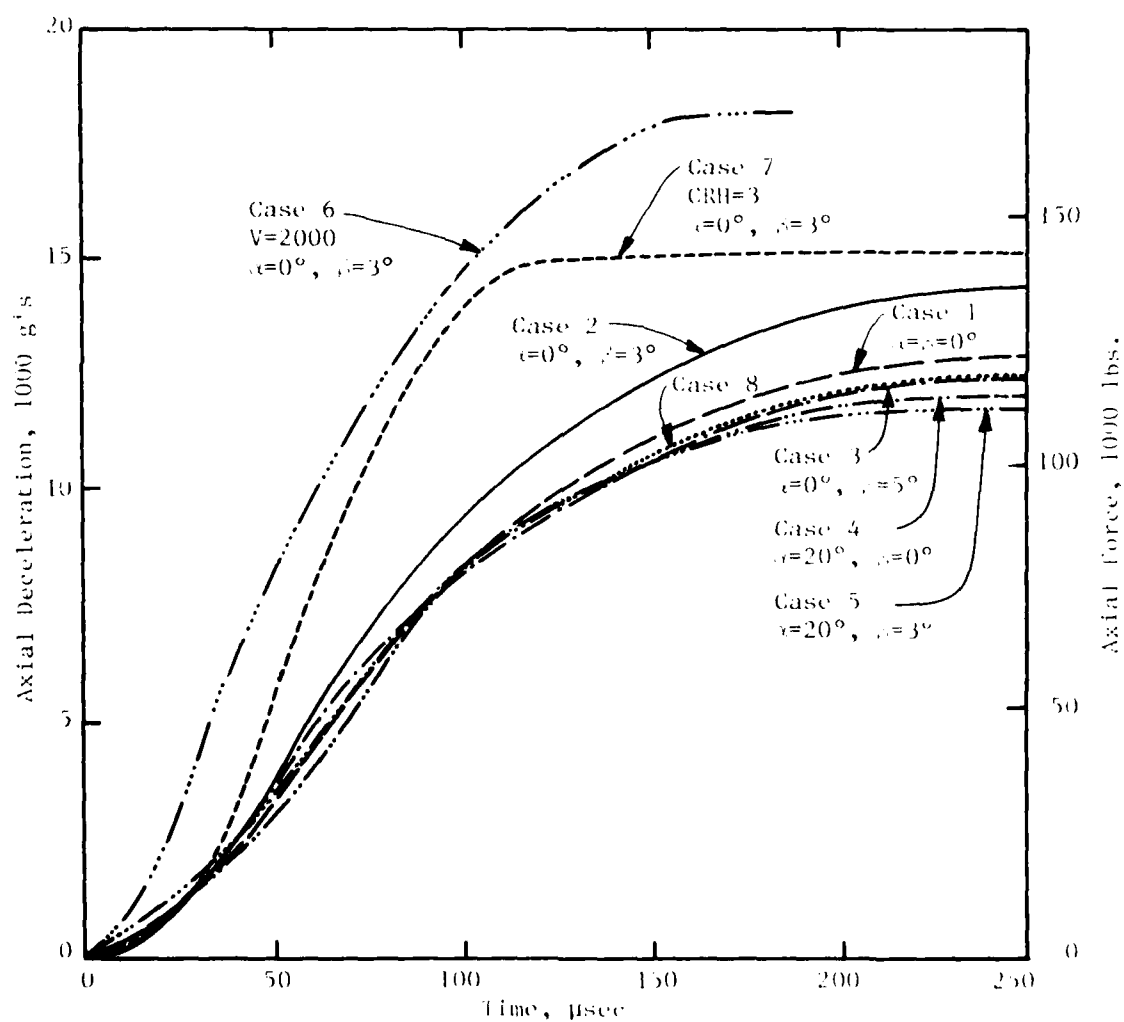


Figure 5.1. Comparison of Penetrator Axial Deceleration.

Case	CRH	L/D	V_i (fps)	α	β	Case	CRH	L/D	V_i (fps)	α	β
1	6.0	10.6	1521	0°	0°	5	6.0	10.6	1521	20°	3°
2	6.0	10.6	1521	0°	3°	6	6.0	10.6	2000	0°	3°
3	6.0	10.6	1521	0°	5°	7	3.0	10.6	1521	0°	3°
4	6.0	10.6	1521	20°	0°	8	6.0	5.3	1521	0°	3°

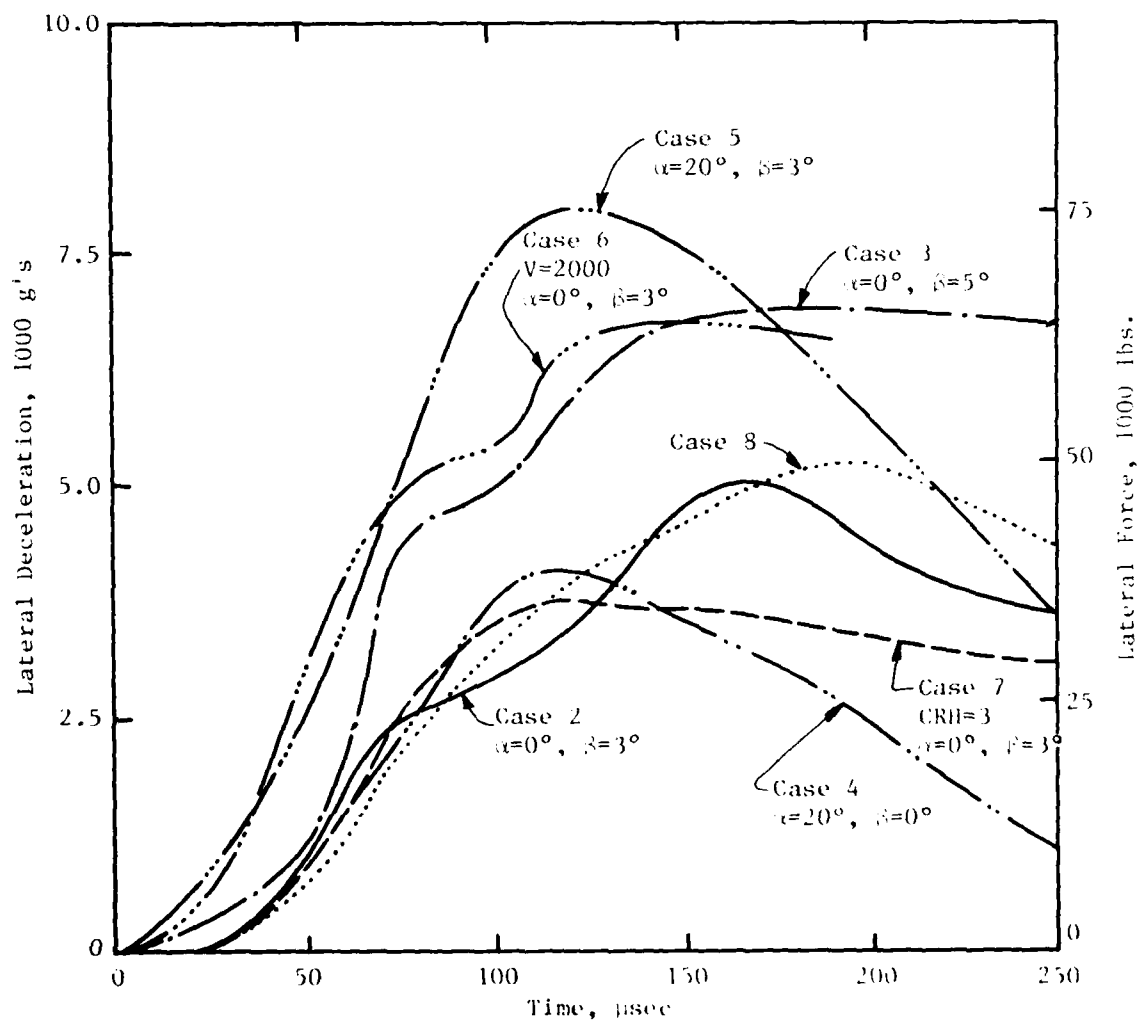


Figure 5.2. Comparison of Penetrator Lateral Deceleration.

Case	CRH	L/D	V_i (fps)	α	β	Case	CRH	L/D	V_i (fps)	α	β
1	6.0	10.6	1521	0°	0°	5	6.0	10.6	1521	20°	3°
2	6.0	10.6	1521	0°	3°	6	6.0	10.6	2000	0°	3°
3	6.0	10.6	1521	0°	5°	7	3.0	10.6	1521	0°	3°
4	6.0	10.6	1521	20°	0°	8	6.0	5.3	1521	0°	3°

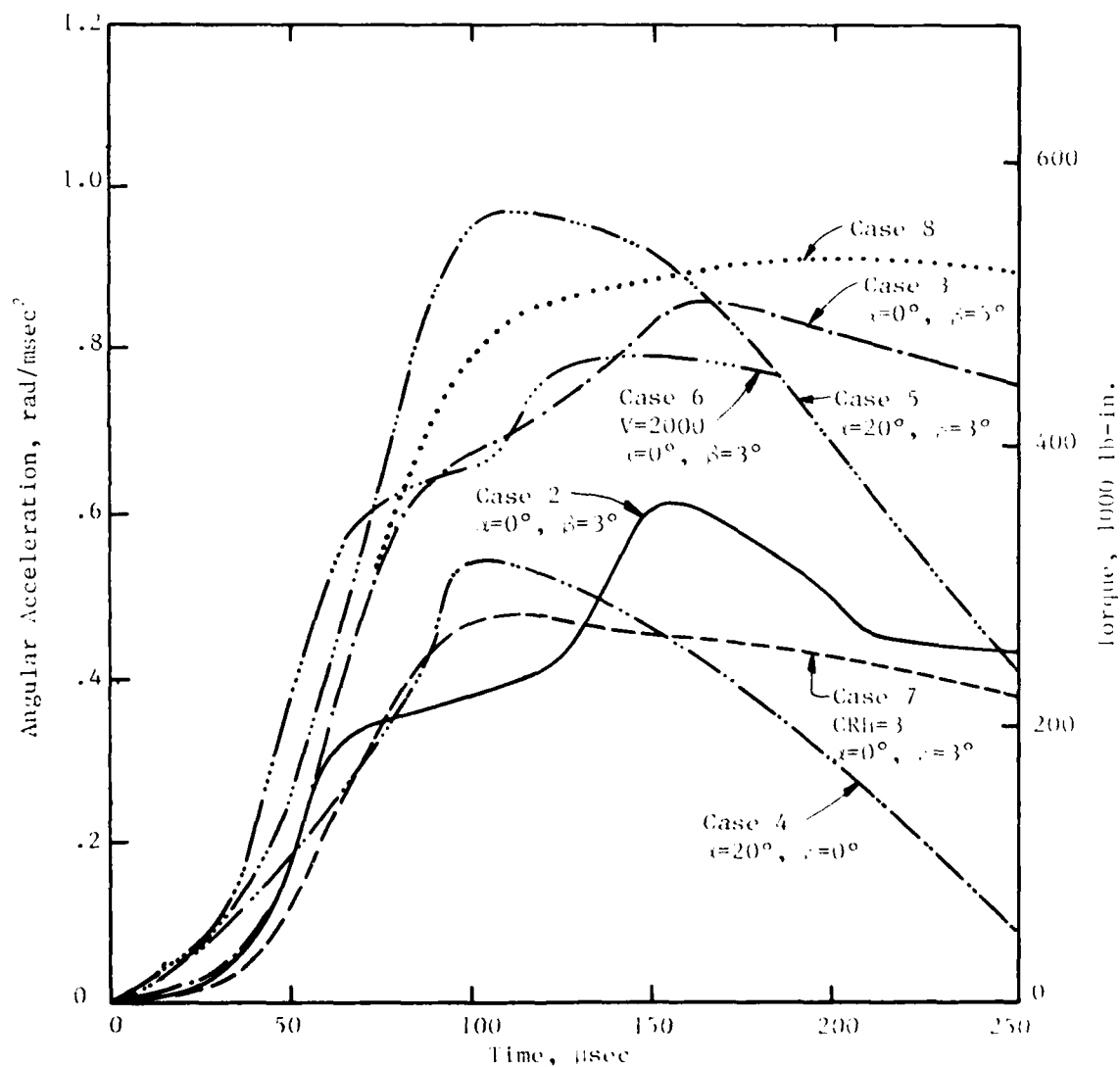


Figure 5.3. Comparison of Penetrator Angular Acceleration.

yawed impact (Case 2, $\beta = 3^\circ$; Case 3, $\beta = 5^\circ$) shows that even modest increases in yaw produces very sizeable increases in angular and lateral acceleration, roughly proportional to the increase in yaw. For both Case 2 and 3 the lateral and angular accelerations appear to reach a peak and then to remain stable, i.e., the initial lateral and angular accelerations persist through complete embedment, indicating a possible longer term stability problem. In Case 4, that of oblique impact only ($\alpha = 20^\circ$, $\beta = 0^\circ$) some initial lateral and angular acceleration develops, but after reaching a peak comparable to the normal impact 3° yaw case, the accelerations rapidly drop. Thus, oblique impact without yaw appears to much more stable than normal impact with yaw. The case when both yaw (3°) and obliquity ($\alpha = 20^\circ$) are present, Case 5, shows a weak coupling between yaw and obliquity with these results being almost a superposition of the results for $\alpha = 0^\circ$, $\beta = 3^\circ$ and for $\alpha = 20^\circ$, $\beta = 0^\circ$.

Case 6 is a special case in which the impact velocity is increased. Surprisingly, the lateral and angular accelerations for this slightly yawed case ($\alpha = 0^\circ$, $\beta = 3^\circ$) is quite comparable to the lower velocity case (1521 ft/sec) with a greater yaw ($\alpha = 0^\circ$, $\beta = 5^\circ$). Thus, from the standpoint of lateral and angular acceleration, 30% increases in impact velocity tend to produce the same effects at 67% increases in yaw. Clearly, both yaw and impact velocity emerge as key parameters, with obliquity playing a somewhat lesser role.

Case 7 indicates the effect of nose tip configuration. (As such, comparison should be made between this case and Case 2.) These results imply that the blunter nose tends to reduce the severity of the lateral and angular accelerations for small yaw, an effect probably due to the increased damage to the target material. However, the axial accelerations are higher,

as is evident from Figure 5.1. This implies that the blunter nose design will have a more stable penetration path, with a less harsh environment on the structure (since bending action is the primary effect on slender $L/D = 10.6$ penetrators). Unfortunately, the depth of penetration will be reduced.

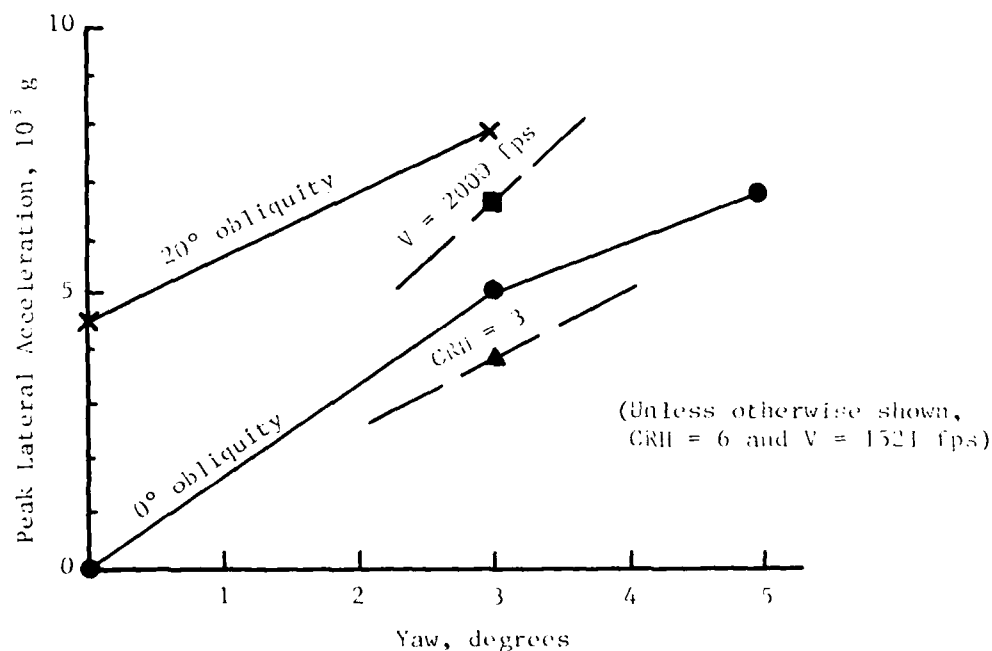
Finally, Case 8 is a case analyzed to investigate the effect of reducing the L/D ratio, here by 50%. This analysis is somewhat artificial since all other properties are preserved, including total mass. This configuration, which has an axial deceleration similar to the more slender EPWs, has a lateral acceleration similar to Case 2, but with a much higher angular acceleration, similar to Case 3. This vehicle then appears to have a less desirable post-impact stability performance than the $L/D = 10.6$ designs. This conclusion is viewed as very tentative due to the highly concentrated mass properties assigned to this missile.

Table 5.2 summarizes the conclusions obtained by the parametric analysis. It is important to recognize that care must be exercised in extrapolating information from this data. For example, an increase in obliquity may result in ricochet and a further reduction in CRH to values substantially less than three may result in the generation of very high axial accelerations which may be sufficient to cause structural failure.

This parametric analysis does not support the findings in [1] in which a parametric analysis (based on a very simple single degree of freedom structural model) infers that impact velocity increases may reduce the severity of the impact environment. The present analysis, which is based on first principles codes indicates the opposite, namely higher velocity impacts are more harsh than low velocity impacts, in all cases.

Table 5.2. Parametric Analyses of Asymmetric Penetration

1. For nose shapes considered, obliquities to 20° and yaw angles to 5° do not significantly affect *axial* acceleration as compared to normal impact.
2. Lateral (and angular) accelerations are very sensitive to yaw and/or obliquity:



3. CRH = 3 nose shape gives ~5% *greater* axial acceleration than CRH = 6 nose shape, but ~25% *smaller* lateral acceleration.
4. For CRH = 6 nose shape, 2000 fps impact velocity gives ~30% greater lateral *and* axial accelerations than 1521 fps.
5. L/D = 5.3 penetrator has about the *same* lateral acceleration, but ~50% *greater* angular acceleration than L/D = 10.6 penetrator with same W/A.

These eight analyses, which are by no means comprehensive, nevertheless demonstrate a number of important effects regarding post-impact EPW performance. Certainly, other parameters should be investigated, such as target properties, layered targets and missile aft body flare. The TRIFLE code is both an efficient tool for accomplishing these tasks and an essential part of the TRIFLE/NONSAP analysis of post-impact structural response. Thus, these codes are ideally suited to investigate penetration stability and efficiency and EPW post-impact survivability.

SECTION 6

CONCLUSIONS AND RECOMMENDATIONS FOR FUTURE INVESTIGATION

The development of the TRIFLE code permits the study of nonlinear asymmetric impact problems such as the EPW penetration problems investigated in this report. The use of truncated Fourier representations allows full three-dimensional problems to be analyzed much more economically than with three-dimensional codes. In fact, when compared with a 3-D Cartesian code TRIFLE gives more precise information at the impact site. The code gives detailed stress information which can easily be used by other codes such as the CRT/NONSAP finite element code to investigate EPW elastic-plastic structural response.

The TRIFLE and CRT/NONSAP computer programs, both of which are first principles codes, are used to perform a detailed analysis of the 0.284-scale RBT. Experimental and analytical results are shown to compare favorably given the difficulties inherent in both experiment and analysis. The analysis shows that for (3°) yawed impact the penetrator response is dominated by large inelastic bending deformations due to the large lateral forces generated in the nose. Large ringing type accelerations are predicted by the analysis, indicating the presence of intense stress wave motions in the penetrator structure.

The TRIFLE code also has been used to investigate the influence of several parameters on penetration dynamics. The analysis shows that slight yaw is very important in determining both flight stability and penetrator survivability. In fact, it is nearly as influential as initial impact velocity. Other parameters which were investigated were moderate (20°) initial flight obliquity, nose design (CRH ratio) and L/D ratio. It appears that moderate obliquity is less important than yaw and that

moderate obliquity without yaw generates lateral and angular accelerations which can be at least approximately superimposed on yawed and normal impact results. Nose shapes more blunt than the 0.284-scale design ($CRH = 6$) increase axial deceleration (and decrease penetration efficiency) but appear to stabilize post-impact penetration. Low L/D ratios appear to be less stable than the higher ratio designs given identical mass.

It is apparent from both the 0.284-scale test and the analysis that 3° yaw impact into Dakota sandstone at 1521 ft/sec extends the penetrator steel to its limit. This investigation shows that an increase in either impact velocity, yaw or obliquity will very likely produce large scale damage and/or failure of the missile.*

Since the intense bending stresses in the high L/D penetrator are primarily due to lateral forces applied to the forward end during early phases of the impact, obvious ways of increasing the resistance of EPW to impact are a) to reduce the CRH ratio, i.e., make the nose more blunt, and b) to reduce the L/D ratio. The first design modification will produce moderate improvements in penetrator survivability, but reduce penetration efficiency. The second will improve penetrator survivability but also reduce penetration efficiency when compared with high L/D ratio design with equal total mass.

The post-impact penetration stability of the low L/D design is also a matter of concern based on the present analysis. This stability problem may be eliminated by increasing aft body flare and/or relocating center-of-mass in a more forward position. Both design modifications can easily be investigated with the TRIFLE-NONSAP analysis capability.

* These results disagree with the results in [1], which indicate that increases in impact velocity for yawed impact can reduce the severity of impact.

Finally, while the present results indicate that moderate obliquity is not by itself a major problem, the results also show the buildup of significant lateral forces and moments which tend to cause the penetrator flight path to curve toward the target surface. Given a sufficient obliquity, it appears very likely that ricochet will occur, with attendant severe bending stresses and probability of penetrator dismemberment. In addition, the very intense stress wave induced by the initial impact show that another potential survivability problem may be encountered for EPWs encountering layered and/or discontinuous targets, such as reinforced concrete and boulder rubble targets. The analysis of EPW impact into targets with oblique surfaces, layered materials and discontinuities is therefore very important with respect to determining both post-impact penetration stability and efficiency. Perhaps the most significant problem is the determination of survivability margins for EPWs impacting these more difficult targets.

REFERENCES

1. Henderson, D., "Evaluation of High L/D Earth Penetrators," Final Report DNA 4984F, Defense Nuclear Agency, Washington, DC, November 1978.
2. Bernard, R. S. and Creighton, D. C., "Non-Normal Impact and Penetration: Analysis for Hard Targets and Small Angles of Attack," Technical Report S-78-17, U. S. Army Engineer Waterways Experiment Station, Vicksburg, MS, September 1978.
3. McCormick, J. M., "Comparison of Pre-Shot Response Predictions with AVCO Reverse Ballistic Tests of Half-Scale Penetrators," Topical Report DNA 4482T, Defense Nuclear Agency, Washington, DC, November 1977.
4. Ito, Y. M., Kreyenhagen, K. N. and Wagner, M. H., "Internal Response Analyses of Earth Penetrators," Topical Report DNA 4118T, Defense Nuclear Agency, Washington, DC, August 1976.
5. Ito, Y. M., Kreyenhagen, K. N., Eggum, G. E. and Goerke, W. S., "Analysis of Dynamic Stresses within a Terminal Delivery Vehicle During Penetration of a Hard Earth Target," Contract Report S-75-1, U. S. Army Engineer Waterways Experiment Station, Vicksburg, MS, February 1975.
6. Wagner, M. H., Kreyenhagen, K. N. and Goerke, W. S., "Numerical Analysis of Projectile Impact and Deep Penetration into Earth Media," Contract Report S-75-4, U. S. Army Engineer Waterways Experiment Station, Vicksburg, MS, August 1975.
7. Wagner, M. H., Kreyenhagen, K. N. and Goerke, W. S., "Numerical Analyses of DNA Earth Penetrator Experiment at DRES," Final Report DNA 3537F, Defense Nuclear Agency, Washington, DC, October 1974.
8. Creighton, D. C., "Correlation of Reverse Ballistic Test Data," Structures Laboratory, U. S. Army Engineer Waterways Experiment Station, Vicksburg, MS, December 1977.
9. Creighton, D. C., "Correlation of Additional Reverse Ballistic Test Data," Structures Laboratory, U. S. Army Engineer Waterways Experiment Station, Vicksburg, MS, August 1978.

10. Wilkins, M. L., "Calculation of Elastic-Plastic Flow," UCRL-7322, Rev. 1, Lawrence Radiation Laboratory, University of California, Livermore, January 1969.
11. Butler, D. K., Nielsen, R. K., Dropek, R. K. and Butters, S. W., "Constitutive Property Investigations in Support of Full-Scale Penetration Tests in Dakota Sandstone, San Ysidro, New Mexico," Technical Report S-77-3, U. S. Army Engineer Waterways Experiment Station, Vicksburg, MS, April 1977.
12. Wagner, M. H., "Material Model for Dakota Sandstone," California Research & Technology, Inc., Woodland Hills, CA, January 1976.
13. Bathe, K.-J., Wilson, E. L. and Iding, R. H., "NONSAP, A Structural Analysis Program for Static and Dynamic Response of Nonlinear Systems," UC-SESM 74-3, Structural Engineering Laboratory, University of California, Berkeley, CA, February 1974.

DISTRIBUTION LIST

DEPARTMENT OF DEFENSE

Assistant to the Secretary of Defense
Atomic Energy
ATTN: Executive Assistant

Defense Intelligence Agency
ATTN: DB-N4
ATTN: RDS-2A
ATTN: DT-2
ATTN: DB-4C, E. O'Farrell

Defense Nuclear Agency
ATTN: SPAS
2 cy ATTN: SPSS
4 cy ATTN: TITL

Defense Tech Info Center
12 cy ATTN: DD

Field Command
Defense Nuclear Agency
ATTN: FCPR, J. T. McDaniel

Field Command
Defense Nuclear Agency
Livermore Branch
ATTN: FCPRL

Interservice Nuclear Weapons School
ATTN: TTV

Joint Strat Tgt Planning Staff
ATTN: JLA
ATTN: NRI-STINFO, Lib

NATO School (SHAPE)
ATTN: US Documents Officer

Under Secretary of Defense for Rsch & Engrg
ATTN: Strategic & Space Sys (OS)

DEPARTMENT OF THE ARMY

Chief of Engineers
Department of the Army
2 cy ATTN: DAEN-MCE-D
2 cy ATTN: DAEN-RDL

Deputy Chief of Staff for Ops & Plans
Department of the Army
ATTN: DAMO-NC

Deputy Chief of Staff for Rsch Dev & Acq
Department of the Army
ATTN: DAMA-N-CSS, N. Barron

Engineer Studies Center
Department of the Army
ATTN: DAEN-FES

Gator Mine Program
Department of the Army
ATTN: E. Lindsay

US Army Armament Material Readiness Command
ATTN: MA, Lib

DEPARTMENT OF THE ARMY (Continued)

Harry Diamond Laboratories
Department of the Army
ATTN: DELHD-N-P, J. Gwaltney
ATTN: DELHD-N-P

US Army Ballistic Rsch Labs
ATTN: DRDAR-BLT, G. Grabarek
ATTN: DRDAR-BLT, G. Roeker
ATTN: DRDAR-BLT, A. Ricchiazzi
ATTN: DRDAR-BL
ATTN: DRDAR-BLT, J. Keefer
2 cy ATTN: DRDAR-TSB-S

US Army Chemical School
ATTN: ATZN-CM-CS

US Army Cold Region Res Engr Lab
ATTN: G. Swincow

US Army Concepts Analysis Agency
ATTN: CSSA-ADL

US Army Engineer Ctr
ATTN: ATZA

US Army Engineer Div, Huntsville
ATTN: HNDED-SR

US Army Engineer Div, Missouri River
ATTN: Tech Lib

US Army Engineer School
ATTN: ATZA-CDC
ATTN: ATZA-DTE-ADM

US Army Engr Waterways Exper Station
ATTN: WESSD, J. Jackson
ATTN: D. Butler
ATTN: WESSA, W. Flathau
ATTN: J. Strange
ATTN: WESSE, L. Ingram
ATTN: Lib
ATTN: B. Romani

US Army Mat Cmd Proj Mgr for Nuc Munitions
ATTN: DRCPM-NUC

US Army Material & Mechanics Rsch Ctr
ATTN: Tech Lib

US Army Materiel Dev & Readiness Cmd
ATTN: DRXAM-TL

US Army Materiel Sys Analysis Actv
ATTN: DRXSY-D, J. Sperrazza

US Army Missile Command
ATTN: F. Fleming
ATTN: RSIC
ATTN: DRCPM-PL, W. Jann

US Army Mobility Equip R&D Cmd
ATTN: DRDME-XS
ATTN: DRDME-WC

DEPARTMENT OF THE ARMY (Continued)

US Army Nuclear & Chemical Agency
ATTN: Lib

US Army War College
ATTN: Lib

DEPARTMENT OF THE NAVY

Marine Corp
Department of the Navy
ATTN: POM

Marine Corp Dev & Education Command
Department of the Navy
ATTN: D091, J. Hartneady

Naval Civil Engineering Lab
ATTN: Code L08A

Naval Explosive Ord Disposal Fac
ATTN: Code 504, J. Petrousky

Naval Postgraduate School
ATTN: Code 1424, Lib

Naval Rsch Lab
ATTN: Code 2627

Naval Sea Systems Command
ATTN: SEA-033
ATTN: SEA-9931G

Naval Surface Weapons Ctr
ATTN: Code F31
ATTN: Code U401, M. Kleinerman
ATTN: Code X211

Naval Surface Weapons Ctr
ATTN: Tech Lib & Info Svcs Br

Naval Weapons Ctr
ATTN: Code 233
ATTN: Code 266, C. Austin

Naval Weapons Evaluation Facility
ATTN: Code 10

Office of the Chief of Naval Operations
ATTN: OP 654C3, R. Piacesi
ATTN: OP 982
ATTN: OP 982E, M. Lenzini

Strategic Systems Project Office
Department of the Navy
ATTN: NSP-43

DEPARTMENT OF THE AIR FORCE

Air Force Armament Lab
ATTN: ADTC/XRS, M. Valentine
3 cy ATTN: DLYV, J. Collins

Air Force Institute of Technology
ATTN: Lib

Air Force Weapons Lab
Air Force Systems Command
ATTN: SUL

DEPARTMENT OF THE AIR FORCE (Continued)

Air University Lib
Department of the Air Force
ATTN: AUL-LSE

Assistant Chief of Staff
Intelligence
Department of the Air Force
ATTN: INT

Ballistic Missile Office
Air Force Systems Command
ATTN: SYDT
ATTN: HQ Space Div/RSS

Deputy Chief of Staff
Rsch, Dev. & Acq
Department of the Air Force
ATTN: R. Steere

Foreign Technology Div
Air Force Systems Command
ATTN: NIIS, Lib

Oklahoma State University
Fld Off for Wpns Effectiveness
Department of the Air Force
ATTN: E. Jakkett

Rome Air Development Center
Air Force Systems Command
ATTN: TSLD

Strategic Air Command
Department of the Air Force
ATTN: INT, E. Jacobsen

DEPARTMENT OF ENERGY

Department of Energy
Albuquerque Operations Office
ATTN: CTID

Department of Energy
ATTN: CMA/RD&T

Department of Energy
Nevada Operations Office
ATTN: Mail & Records for Tech Lib

OTHER GOVERNMENT AGENCIES

Central Intelligence Agency
ATTN: OSWR/NED

Federal Emergency Management Agency
National Sec Ofc Mitigation & Rsch Div
ATTN: Mitigation & Rsch Div

NASA
Ames Research Center
ATTN: R. Jackson

US Nuclear Regulatory Commission
ATTN: R. Whipp for Div Sec, L. Shao

DEPARTMENT OF ENERGY CONTRACTORS

Lawrence Livermore National Lab
ATTN: L-504, M. Wilkins
ATTN: Tech Info Dept Library
ATTN: J. Goudreau

Los Alamos National Lab
ATTN: M/S634, T. Dowler
ATTN: Reports Lib

Sandia National Lab
ATTN: W. Caudle
ATTN: W. Herrman
ATTN: W. Altsmeirer
ATTN: W. Patterson
ATTN: 3141
ATTN: J. Colp
ATTN: 5612, J. W. Keizur
ATTN: A. Chabai

Sandia National Laboratories
Livermore Laboratory
ATTN: Lib & Sec Classification Div

DEPARTMENT OF DEFENSE CONTRACTORS

Aerospace Corp
ATTN: Tech Info Services

Agbabian Associates
ATTN: M. Agbabian

Applied Theory, Inc
2 cy ATTN: J. Trulio

AVCO Rsch & Systems Group
ATTN: D. Henderson
ATTN: Lib A830

BDM Corp
ATTN: T. Neighbors
ATTN: Corporate Lib

Boeing Co
ATTN: Aerospace Lib

California Rsch & Tech, Inc
ATTN: K. Kreyenhagen
ATTN: Lib
4 cy ATTN: Y. Ito
4 cy ATTN: R. Nelson
4 cy ATTN: F. Ross-Perry

California Rsch & Tech, Inc
ATTN: D. Orphal

EG&G Wash Analytical Svcs Ctr, Inc
ATTN: Lib

Engineering Societies Lib
ATTN: A. Mott

General Dynamics Corp
ATTN: R. Dibrell

Honeywell, Inc
ATTN: T. Helvig

Institute for Defense Analyses
ATTN: Classified Lib

DEPARTMENT OF DEFENSE CONTRACTORS (Continued)

J. D. Haltiwanger Consult Eng Svcs
ATTN: W. Hall

Kaman Avidyne
ATTN: N. Hobbs
ATTN: E. Criscione
ATTN: Library

Kaman Sciences Corp
ATTN: Library

Kaman Tempo
ATTN: DASAC

Lockheed Missiles & Space Co., Inc
ATTN: Tech Info Ctr

Lockheed Missiles & Space Co., Inc
ATTN: TIC-Lib
ATTN: M. Culp

Martin Marietta Corp
ATTN: H. McQuaig
ATTN: A. Cowan
ATTN: M. Anthony

Merritt CASES, Inc
ATTN: Lib
ATTN: J. Merritt

University of New Mexico
ATTN: G. Triandafalidis

Pacific-Sierra Rsch Corp
ATTN: H. Brode

Pacifica Technology
ATTN: R. Bjork
ATTN: G. Kent

Physics International Co
ATTN: L. Behrmann
ATTN: Tech Lib

R & D Associates
ATTN: P. Rausch
ATTN: A. Field
ATTN: Tech Info Ctr
ATTN: J. Lewis
ATTN: W. Wright
ATTN: P. Haas

Rand Corp
ATTN: Lib

Science Applications, Inc
ATTN: Tech Lib

Science Applications, Inc
ATTN: W. Layson

SRI International
ATTN: G. Abrahamson
ATTN: J. Fulton

Terra Tek
ATTN: Lib

DEPARTMENT OF DEFENSE CONTRACTORS (Continued)

Systems, Science & Software, Inc

ATTN: Lib

ATTN: R. Sedgewick

TRW Defense & Space Sys Group

ATTN: N. Lipner

ATTN: Tech Info Ctr

TRW Defense & Space Sys Group

ATTN: E. Wong

ATTN: P. Dai

DEPARTMENT OF DEFENSE CONTRACTORS (Continued)

Weidlinger Assoc., Consulting Engrg

ATTN: M. Baron

ATTN: J. McCormick

Weidlinger Assoc., Consulting Engrg

ATTN: J. Isenberg